

A self-adaptive cohesive zone model for interfacial delamination

Citation for published version (APA):

Samimi, M. (2011). *A self-adaptive cohesive zone model for interfacial delamination*. [Phd Thesis 1 (Research TU/e / Graduation TU/e), Mechanical Engineering]. Technische Universiteit Eindhoven.
<https://doi.org/10.6100/IR712618>

DOI:

[10.6100/IR712618](https://doi.org/10.6100/IR712618)

Document status and date:

Published: 01/01/2011

Document Version:

Publisher's PDF, also known as Version of Record (includes final page, issue and volume numbers)

Please check the document version of this publication:

- A submitted manuscript is the version of the article upon submission and before peer-review. There can be important differences between the submitted version and the official published version of record. People interested in the research are advised to contact the author for the final version of the publication, or visit the DOI to the publisher's website.
- The final author version and the galley proof are versions of the publication after peer review.
- The final published version features the final layout of the paper including the volume, issue and page numbers.

[Link to publication](#)

General rights

Copyright and moral rights for the publications made accessible in the public portal are retained by the authors and/or other copyright owners and it is a condition of accessing publications that users recognise and abide by the legal requirements associated with these rights.

- Users may download and print one copy of any publication from the public portal for the purpose of private study or research.
- You may not further distribute the material or use it for any profit-making activity or commercial gain
- You may freely distribute the URL identifying the publication in the public portal.

If the publication is distributed under the terms of Article 25fa of the Dutch Copyright Act, indicated by the "Taverne" license above, please follow below link for the End User Agreement:

www.tue.nl/taverne

Take down policy

If you believe that this document breaches copyright please contact us at:

openaccess@tue.nl

providing details and we will investigate your claim.

A self-adaptive cohesive zone model for interfacial delamination

Mohammad Samimi

This research was carried out within the project WP IV-C-3 of the MicroNed program. It was partially supported by the valorization project number MA.10191 in the framework of the Knowledge Application Project of the Materials innovation institute (M2i).

CIP-DATA LIBRARY TECHNISCHE UNIVERSITEIT EINDHOVEN

Samimi Mohammad

A self-adaptive cohesive zone model for interfacial delamination.

Eindhoven University of Technology, 2011.

Proefschrift.

A catalogue record is available from the Eindhoven University of Technology Library. ISBN: 978-90-386-2493-8

This thesis is prepared with L^AT_EX₂ ϵ .

Cover design: Paul Verspaget

Printed by the Universiteitsdrukkerij TU Eindhoven, Eindhoven, The Netherlands.

A self-adaptive cohesive zone model for interfacial delamination

PROEFSCHRIFT

ter verkrijging van de graad van doctor aan de
Technische Universiteit Eindhoven, op gezag van de
rector magnificus, prof.dr.ir. C.J. van Duijn, voor een
commissie aangewezen door het College voor
Promoties in het openbaar te verdedigen
op dinsdag 31 mei 2011 om 16.00 uur

door

Mohammad Samimi

geboren te Esfahan, Iran

Dit proefschrift is goedgekeurd door de promotor:

prof.dr.ir. M.G.D. Geers

Copromotor:

dr.ir. J.A.W. van Dommelen

Contents

Summary	ix
1 Introduction	1
1.1 Cohesive zone models	1
1.2 Objective of the thesis	4
1.3 Self-adaptive finite elements	4
1.4 Outline of the thesis	5
2 An enriched cohesive zone model	7
2.1 Introduction	8
2.2 Problem statement; mode I delamination	11
2.2.1 Geometry, interface model, and material behavior	11
2.2.2 Analytical solution	13
2.2.3 Numerical solution	14
2.3 Cohesive zone enrichment	16
2.3.1 Interface elements	16
2.3.2 Bulk elements	20
2.4 Implementation aspects	23
2.4.1 Penalty factor	23
2.4.2 Adaptive enrichment strategy	23
2.5 Application to the example problem	24
2.6 Discussion and conclusion	25
2.7 Appendix A: Determination of the tangential stiffness matrix	27
3 A mixed-mode self-adaptive cohesive zone model	31
3.1 Introduction	32
3.2 Interface model	34
3.3 Cohesive zone enrichment	36
3.3.1 Interface elements	36
3.3.2 Bulk elements	39
3.4 Numerical aspects of the enrichment	41
3.5 Mixed-mode application	46
3.6 Discussion and conclusion	49

3.7	Appendix A: Element formulation	52
3.7.1	Cohesive zone elements	52
3.7.2	Bulk elements	52
3.8	Appendix B: Tangential stiffness matrix	53
3.8.1	Cohesive zone elements	53
3.8.2	Bulk elements	55
4	A three-dimensional self-adaptive cohesive zone model	57
4.1	Introduction	58
4.2	Self-adaptive 3D finite elements	61
4.2.1	Interface element kinematics	62
4.2.2	Bulk element kinematics	64
4.2.3	Numerical implementation	66
	Enrichment strategy	66
	Numerical integration	67
	Solution convergence and uniqueness	68
4.3	Numerical examples	68
4.3.1	Problem statement	68
4.3.2	Constitutive model for mixed-mode delamination	69
4.3.3	Cracks aligned with element edges	72
4.3.4	Cracks oblique with respect to element edges	74
4.4	An alternative enrichment strategy	75
4.4.1	Non-hierarchical self-adaptive finite elements	76
4.4.2	Simulation of a propagating oblique crack	78
4.5	Conclusion and remarks	79
5	A large deformation self-adaptive cohesive zone model	83
5.1	Introduction	84
5.2	Interface model	85
5.3	Large deformation self-adaptive finite elements	87
5.4	Miniaturized mixed-mode bending test	91
5.5	Discussion and conclusion	98
5.6	Appendix A: Interface tangent matrix	100
5.7	Appendix B: Transformation matrices	101
5.8	Appendix C: Stress stiffness matrices	103
6	General conclusion and outlook	105
6.1	Conclusion	105
6.2	Outlook	108
	Bibliography	111
	Samenvatting	123
	Acknowledgements	125

Curriculum Vitae

127

A self-adaptive cohesive zone model for interfacial delamination

Summary

Interfacial failure in the form of delamination, often results in malfunction or failure of laminated structures. Different numerical approaches have been proposed for the simulation of this process. Due to the appealing feature of predicting both the delamination onset and its growth, cohesive zone models have been widely used to simulate delamination as a result of a gradual degradation of the adhesion between two materials when they become separated.

Application of cohesive zone models for the modelling of delamination in brittle interfaces in a quasi-static finite element framework suffers from an intrinsic discretization sensitivity. A large number of interface elements are needed for the discretization of the process zone of a cohesive crack. Otherwise, a sudden release of energy in large cohesive zone elements results in a sequence of snap-through or snap-back points to appear in the global load-displacement response of the system which compromises the numerical efficiency.

While computationally expensive path-following techniques can be used to follow the oscillatory path, the efficiency and robustness of brittle cohesive zone models can be significantly increased by reducing the oscillations observed in the global load-displacement behaviour without a further mesh refinement. In line with this purpose, the separation approximation in the process zone is enriched with an adaptive hierarchical extension. The linear separation approximation throughout the cohesive zone element is enriched with a bi-linear function, where the enrichment peak position and the magnitude of the enrichment are regarded as additional degrees of freedom obtained by minimization of the total potential of the global system. The mobility of the peak of the enrichment function within individual cohesive zone elements locally adapts the discretization to the physics governing the problem.

Important numerical aspects of the proposed enrichment strategy such as its mobility and uniqueness have been thoroughly investigated while its limitations are addressed. The efficiency and robustness of the enrichment are shown through numerical examples which prove the general applicability of the methodology. In fact, application of the elaborated enrichment eliminates the need for a further mesh refinement while keeping the standard Newton-Raphson approach applicable in the case of a relatively coarse mesh which saves considerable computational costs.

Extension of the proposed enrichment scheme to delamination in a three-dimensional finite element framework has been carried out as well. Planar inter-

face elements have been enriched along all edges by bi-linear functions with mobile peaks. The effect of the proposed methodology on reducing discretization-induced oscillations is quantitatively evaluated. To deal with planar crack growth where the crack front is oblique with respect to element edges, a non-hierarchical enrichment strategy is also developed and its performance is compared with its hierarchical counterpart.

The self-adaptive finite element formulation is extended to a framework suitable for large deformations and is applied to interfaces in microelectronics under realistic mixed-mode loading conditions. In particular, the material/interface systems used in miniaturized mixed-mode bending tests, which are conducted for a wide range of mode angles, are modelled to make a direct comparison with experimental results. The interface constitutive law that is used takes the dependence of fracture toughness on mode-mixity into account. Thereby, the enhanced cohesive zone model can be used for the simulation of the behaviour of brittle interfaces in an accurate, effective, and efficient manner.

CHAPTER ONE

Introduction

Abstract

Laminated structures have gained popularity especially in mechanical, micro-electronic, and aerospace applications among other engineering disciplines due to their prominent thermo-electro-mechanical performance combined with unique features such as low weight/size and high toughness. Functionality and reliability of these structures rely not only on their constituents but also on the structural integrity. Accumulation of damage at the interfaces between laminae results in formation and growth of interlaminar cracks through a non-linear and irreversible process which is known as delamination. In fact, it is one of the most common failure modes in multi-layered systems which results in malfunction and loss of integrity and can eventually lead to a structural collapse. Efficient and robust numerical tools verified by dedicated experiments are required to predict delamination initiation and its growth pattern under complex thermo-hygro-mechanical loading conditions that may arise during the lifetime of a laminated structure. It facilitates a prior assessment of the system reliability and performance without a need to perform experiments in individual cases.

1.1 Cohesive zone models

Lumping degradation mechanisms in a small zone around the crack tip as shown in Figure 1.1, where cohesive forces are formed upon a displacement jump, the cohesive zone concept has emerged in continuum models with strong discontinuities [10, 40, 58]. Cohesive zone models have the appealing feature of predicting both delamination initiation and growth by combining stress-based and fracture mechanics-based approaches. These models are well suited for the simulation of interfacial

delamination in laminated structures where the potential crack paths are known a priori [6, 21, 25, 82, 112, 129, 131].

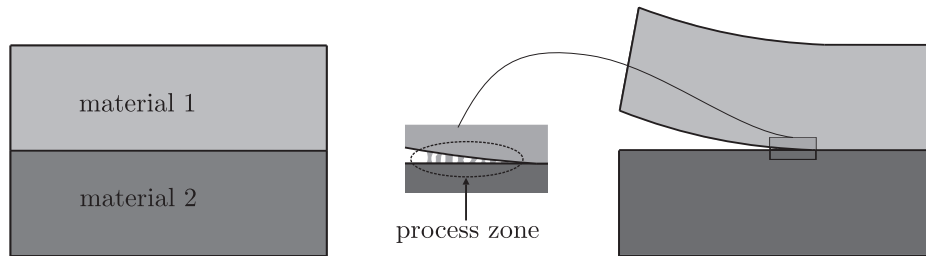


Figure 1.1: Schematic representation of interfacial cohesive crack growth.

In a finite element framework, cohesive zone elements are placed at the interface between the bulk elements of adjacent layers. The decohesion mechanism in the process zone of a cohesive crack, as shown in Figure 1.2, is characterized by a phenomenological traction-separation law reflecting the average micro-mechanical behavior during the degradation process (see Figure 1.2) [24, 35]. In general, interfacial stresses orthogonal or parallel to laminae cause delamination in mode I (normal opening) or modes II (sliding) and III (tearing), respectively.

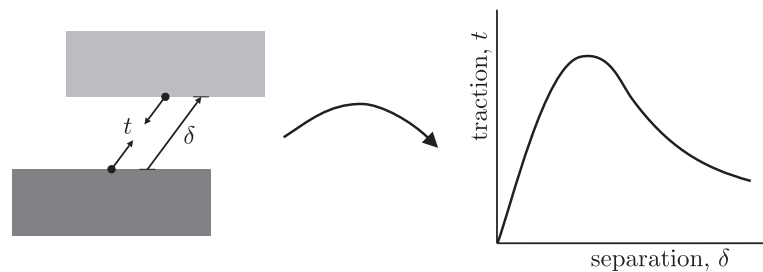


Figure 1.2: Cohesive zone; left) decohesion at an interfacial point, right) phenomenological constitutive law.

The cohesive zone approach can be related to Griffith's theory of fracture, if the area under the traction-separation curve is equal to the corresponding fracture toughness G_c [101]. Assuming a constant fracture toughness for a certain fracture mode, a higher maximum traction (or interfacial strength) would result in a smaller process zone and hence a more brittle interfacial behavior (see Figure 1.3).

Application of cohesive zone models in a quasi-static finite element framework suffers from an intrinsic mesh sensitivity. In other words, a sufficiently fine discretization is needed within the softening process zone of the cohesive crack to capture the strain field [122]. In case of a coarse mesh, softening of the local behavior in an interfacial element will result in a sudden release of the elastic strain energy stored in the surrounding bulk material which in turn leads to instantaneous failure of the element. In such a case, as can be seen in Figure 1.4(b), an artificial (non-physical)

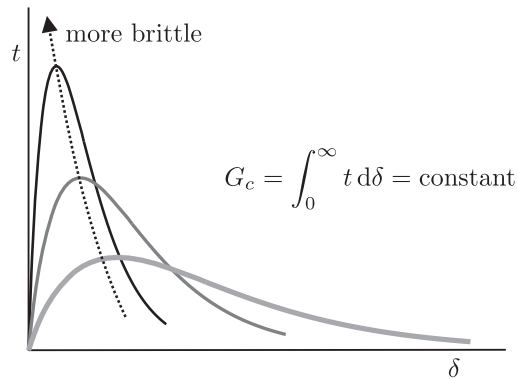


Figure 1.3: Cohesive zone model as a spatial regularization of the fracture mechanics model.

snap-back situation arises in the numerical solution which is also known as a solution jump [22]. It poses major numerical difficulties in solving the global system due to the fact that a standard Newton-Raphson iterative scheme fails to converge in the case of snap-backs. Current solution strategies with respect to this problem can be classified in two categories:

- *Strategies to eliminate or reduce the oscillations;* since the observed oscillations are discretization-induced, they are alleviated upon further mesh refinement (see Figure 1.4(b)). Therefore, the global response of the brittle system becomes smoother as the discretization is refined within the process zone [3,16,22,44,55,82,119,122,124].
- *Strategies to deal with the oscillations;* path-following techniques such as global or local arc-length control methods have been applied to trace the non-physical oscillatory path [4,27,34,45,46,53,57,102,110].

The first option is aimed at eliminating or reducing the oscillations; however, it is not practical in brittle interfaces where the size of the process zone is very small compared to structural dimensions due to unacceptably high computational costs imposed by the large size of the system. The second remedy deals with the existing oscillatory behavior by adding a constraint equation to the set of linearized equations to control the load step size. As a result, snap-backs can be traced with very small increments at the cost of heavy computations.

The solutions that have been proposed so far to avoid or to deal with numerical instabilities in cohesive zone modeling within a quasi-static finite element framework are so expensive that the applicability of these methods in large or complex structures with brittle interfaces is limited. Elimination or reduction of the oscillations in the global response of delaminating structures without a need for a further mesh refinement increases the efficiency and robustness of cohesive zone models considerably. In line with this purpose, attempts have been made to enhance the kinematic description within the process zone via a local enrichment of the elements by higher

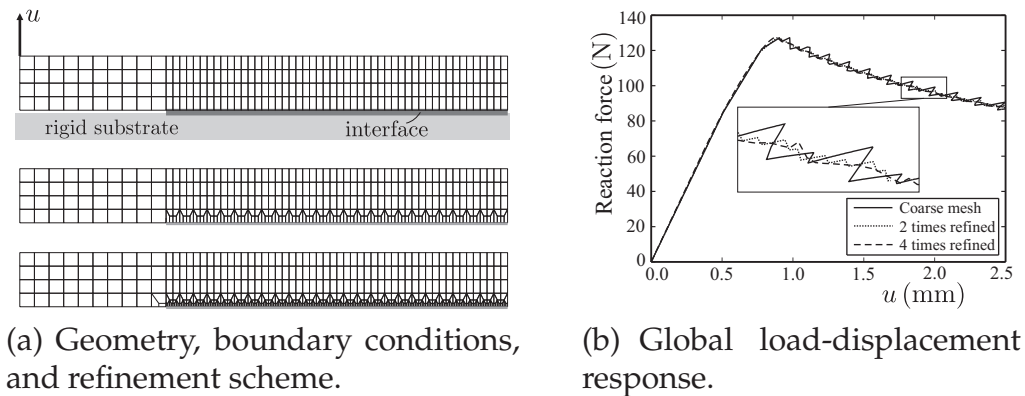


Figure 1.4: Cohesive zone model for simulation of delamination in a peel-off test.

order interpolation functions [28, 52, 119]. However, the fixed functions used do not adequately address the adaptivity (or mobility) of the process zone within the interface.

1.2 Objective of the thesis

This work is aimed at developing a self-adaptive cohesive zone model that facilitates the simulation of interfacial delamination in an effective and robust manner by eliminating the need for extensive computations usually required in this class of methods due to mesh refinements or complicated path-following techniques. More specifically, the objective is to *eliminate the mesh-induced snap-backs/oscillations while also being numerically efficient*.

1.3 Self-adaptive finite elements

In this work, an adaptive hierarchical extension is proposed to enrich the separation approximation in the fracture process zone. The proposed methodology solves the intrinsic shortcoming of the discretization that creates the non-physical oscillatory load-displacement response by refining the discretization where the physics of the underlying problem needs it. The linear separation approximation throughout the cohesive zone element is enriched with a bi-linear function, where the enrichment peak position and the magnitude of the enrichment are regarded as additional global degrees of freedom. The enrichment degrees of freedom are calculated by solving the global system of equations. The bulk elements adjacent to the enriched cohesive zone elements are also enriched to guarantee the continuity of the displacement field.

Adaptivity of the enrichment peak position such that it mimics the growing delamination front in either a two or three-dimensional setting is proposed in this work as an alternative to traditional remedies to overcome or trace spurious discretization-

induced oscillations encountered in cohesive zone modeling. A procedure is developed to ensure uniqueness of the solution when the enrichment peak positions in individual elements are considered as additional global degrees of freedom while imposing a minimum constraint on the adaptivity of the enrichment peak positions. As a consequence, an optimal adaptivity of the enrichment peak position is retrieved. A noticeable reduction of the discretization-induced oscillations in the global response obtained with a self-adaptive cohesive zone model to a level that it can be traced with a standard Newton-Raphson iterative scheme is obtained with the proposed methodology.

The self-adaptive finite element framework is not restricted to a particular constitutive model for the cohesive zone. Moreover, its applicability to three-dimensional delamination problems and its extension to a large deformation framework make it suitable for general engineering applications as illustrated in this thesis.

1.4 Outline of the thesis

In this thesis, a self-adaptive cohesive zone model is developed for interfacial delamination in several steps:

- In Chapter 2, the solution jump problem associated with application of the conventional cohesive zone model to interfacial delamination in brittle interfaces is addressed and a process driven hierarchical extension is proposed to enrich the separation approximation in the process zone of a cohesive crack. A simple one-dimensional example for which an analytical solution exists is used to demonstrate the performance of the new methodology.
- In Chapter 3, a full two-dimensional self-adaptive finite element is developed which can be used for the simulation of irreversible mixed-mode delamination. Adaptivity of the enrichment is considerably enhanced due to the developments proposed in this chapter.
- In Chapter 4, the self-adaptive cohesive zone model is extended to model planar mixed-mode crack growth in a general three-dimensional continuum. The effect of the proposed methodology on reducing discretization-induced oscillations is quantitatively evaluated. A non-hierarchical enrichment strategy is also developed and its performance is compared with its hierarchical counterpart.
- In Chapter 5, the self-adaptive cohesive zone model is formulated within a large deformation framework. The numerical results are compared with experimental results obtained from miniaturized mixed-mode bending tests performed on bi-material specimens.

Finally, general conclusions and outlooks derived from the research on the self-adaptive cohesive zone model are given in Chapter 6.

CHAPTER TWO

An enriched cohesive zone model¹

Abstract

Application of standard cohesive zone models in a finite element framework to simulate delamination in brittle interfaces may trigger non-smooth load-displacement responses that lead to the failure of iterative solution procedures. This non-smoothness is an artifact of the discretization; and hence, can be avoided by sufficiently refining the mesh leading to unacceptably high computational costs and a low efficiency and robustness. In this chapter, a process-driven hierarchical extension is proposed to enrich the separation approximation in the process zone of a cohesive crack. Some numerical examples show that instead of mesh refinement, a more efficient enriched formulation can be used to prevent a non-smooth solution.

¹*Reproduced from:* M. Samimi, J.A.W. van Dommelen, and M.G.D Geers. An enriched cohesive zone model for delamination in brittle interfaces. *Int. J. Numer. Meth. Engng.* 80:609-630, 2009.

2.1 Introduction

Increasing demands for high wear, corrosion, thermal resistance and toughness, combined with reduction in weight and/or size in mechanical, micro-electronic, and aerospace applications have led to the development of multi-layered material systems. The presence of different materials from metals to polymers, and complicated thermo-hygro-mechanical loading conditions in such systems make their reliability or mechanical response more difficult to be analyzed in a predictive manner with existing tools. Since the quality, robustness, and reliability of multi-layered structures such as microsystems depend, to a large extent, on the adhesion and durability of interfaces, interlaminar damage or delamination is one of the predominant forms of their failure, especially when there is no reinforcement in the thickness direction.

The simulation of delamination is usually divided into delamination initiation and delamination propagation. Several methodologies have been developed for numerical simulation and prediction of interfacial delamination. Interface stress is commonly used as a failure criterion in an interface fracture mechanics based finite element analysis of delamination [43]. In stress-based approaches, stress at or near the interface is compared to the critical stress levels to indicate the interfacial regions most prone to delamination. Such methods assume perfect adhesion between materials (no defect state), and therefore overestimate the loading capacity. For microsystems, brittle fracture often occurs in which the size of the failure process zone is small, and hence, linear elastic fracture mechanics (LEFM) concepts can apply [11,67].

Finite element based techniques such as the J-integral [101], virtual crack closure (VCC) [97,105], and virtual crack extension (VCE) [56] have been introduced within the LEFM framework for the prediction of crack growth. The simplified Griffith energy balance states that the mechanical energy supplied to the system, will be stored as an elastic internal energy or dissipated through generating new crack surfaces [51]. Therefore, delamination propagates when the energy available for crack propagation exceeds the fracture toughness, or the critical energy release rate, which is a mechanical parameter of the interface. However, simulation of crack propagation is more complex in the case of a mixed mode delamination where a transverse shear in the contact zone of a crack tip can raise the energy required for failure [74,120,121]. Another drawback of this class of methods is that explicit knowledge of the location and size of an initial interlaminar crack is necessary.

Moreover, a high mesh density in the crack front region is usually required in order to capture the singularity in the asymptotic crack tip fields with the conventional finite element method. In enriched finite element methods, incorporating the asymptotic crack tip fields in the trial functions allows for an accurate computation of fracture parameters [15,48]. However, the mesh generation and regeneration as the crack grows constitutes a major drawback of LEFM approaches. In order to avoid remeshing, finite elements with embedded discontinuities and the element-free Galerkin method (EFGM) have been successfully applied to crack problems [66,118].

The extended finite element method (X-FEM), which was first developed in a two-

dimensional LEFM context using the concept of partition of unity [13,84], can cope well with problems associated with discontinuity of the displacement field across the crack faces. As an advantage to this approach, the need for a further mesh refinement is eliminated to a great extent. To avoid a non-physical singular stress field at the crack tip, the crack growth is accompanied by a cohesive law on crack faces using the partition of unity property of finite elements [83,134]. However, in an X-FEM based approach, the crack tip position is commonly prescribed inside an element, allowing to determine the elements to be enriched by a discontinuous function or by near-tip asymptotic functions [84]. As an alternative, the discontinuity is often (if not mostly) extended across a complete element such that the crack tip touches the next element boundary [134]. Regarding the oscillatory nature of the singular stress in the vicinity of the crack tip, appropriate crack tip asymptotic displacement functions have been added to the finite element approximation for bi-material interface cracks [116].

Although a comparison of crack driving forces in several interfaces provides a qualitative impression of the most vulnerable interface in a multi-layered system, it is still too hard to describe the cases where some cracks may be arrested or evolve simultaneously even in two-dimensional problems when using LEFM-based methods. Furthermore, none of these methods are able to simulate both initiation and propagation of delamination together. To simulate both initiation and propagation of delamination as a result of gradual degradation of the adhesion between laminae, cohesive zone models (CZMs) are proposed that do not suffer from the limitations of the previously mentioned methods when multiple cracks exist.

CZMs were originally introduced by Barenblatt [10] and Dugdale [40] as an alternative to elasticity-based fracture mechanics, which leads to infinite stresses at the crack tip, in perfectly elastic-brittle materials. The earlier approaches were extended in the sense that a cohesive crack could develop anywhere in a specimen or a structure, and not only ahead of a pre-existing crack tip [58].

CZMs are used to describe a broad range of fracture and damage processes in a wide variety of material systems from ductile void growth [126] to fracture in brittle materials [20]. Using CZMs, the behavior of the structure is lumped in two parts; the damage free continuum with an arbitrary material law, and cohesive interfaces between continuum elements that specify the damage of the material. For the modeling of delamination, decohesion elements are placed at interfaces between laminae. Using these elements, the traction with respect to separation across boundaries is defined with a traction-separation law (TSL). An overview of TSLs that have been developed can be found in [24]. The influence of the shape of the traction-separation law on the response and numerical performance of CZMs are also investigated in some recent publications [2,24].

Application of CZMs in a quasi-static framework is accompanied by severe numerical difficulties in the case of relatively brittle interfaces where the solution of the discretized problem rapidly suffers from an intrinsic mesh size dependency. If the mesh is not sufficiently fine, the global load-displacement response of the system shows a non-smoothness that totally compromises the numerical efficiency [3]. In

fact, as delamination propagates, there should be sufficient interface elements in the softening process zone to capture the strain field [122]; otherwise, softening of the local behavior in an interfacial element will result in a sudden release of the elastic strain energy stored in the surrounding bulk material which in turn leads to instantaneous failure of the element. In such a case, an artificial (non-physical) limit point in the form of a snap-through or a snap-back situation arises in the numerical solution which is also known as a solution jump [22].

Remedies such as artificially reducing the interfacial strength to increase the size of the process zone, performing a dynamic analysis or using viscous regularization techniques, and using a non-local formulation for the interface model are either non-realistic or computationally expensive and inefficient. A mesh refinement can overcome this problem without yielding unrealistic results. However, for realistic interface parameters with a small process zone size, the element size has to be extremely small, which results in unacceptably high computational costs. An adaptive mesh refinement around the process zone is a possible way to reduce the computational cost. However, the method itself has extra costs and complexities.

Practically, using the standard iterative Newton-Raphson method under load or displacement control often fails to converge when confronted to the mentioned limit points. Reducing the increment size does not solve the problem, whereas the validity of the solution with large increment sizes can be questioned since several interface nodes may fail simultaneously in a single increment [22]. Therefore, path following techniques such as the cylindrical arc-length control method have been proposed to overcome the non-smoothness even in the case of relatively sharp snap-backs [57]. Since all degrees of freedom contribute with an equal weight in a global path following approach, convergence problems still exist in case of a severely localized deformation, such as interfacial delamination. Therefore, local control techniques are employed to overcome this type of problem [45].

The complicated combination of local path following techniques and line searches can be used at the cost of heavy computations [4], since very small increments are needed to trace a non-physical path. Elimination or at least reduction of the oscillations observed in the global load-displacement behavior of systems involving brittle interfaces without mesh refinement will enhance the efficiency and robustness of cohesive zone models. Local enrichment of the elements in the vicinity of the softening process zone with hierarchical polynomial shape functions is considered a means to reduce these oscillations [28].

In this chapter, a process driven hierarchical extension is proposed to enrich the separation approximation in the process zone of a cohesive crack. The enrichment solves the intrinsic shortcoming of the discretization that creates the non-physical oscillatory load-displacement behavior. In the new formulation, the linear separation approximation throughout the cohesive zone element is enriched by adding a piece-wise linear enrichment function such that the enrichment peak can be located at an arbitrary position within a cohesive zone element. In this approach, the location of the enrichment peak and the magnitude of the enrichment form additional

degrees of freedom. Moreover, continuity of the displacement field requires that bulk elements adjacent to the enriched cohesive zone elements be enriched as well. The principle of virtual work is used to establish the weak form of the equilibrium equations [143]. Numerical examples using a bi-linear TSL show that the proposed enrichment scheme can be used to improve the global load-displacement response of the system discretized by a relatively coarse mesh without a need for further mesh refinement.

2.2 Problem statement; mode I delamination

In order to illustrate the response resulting from a cohesive zone model, a simplified peel-off test is considered for which an analytical solution can be easily retrieved. In this test, a bulk material is pulled from a rigid substrate.

2.2.1 Geometry, interface model, and material behavior

In cohesive zone models, a traction-separation law describes the nonlinear relations between the separation vector δ and the traction vector t . Since the precise form of the TSL is not the subject of interest here, a bilinear TSL is considered, which acts in the normal direction denoted by the vector \mathbf{n} . The normal traction t_n linearly increases with increasing normal separation δ_n until it reaches a maximum $t_{n,max}$. The separation $\delta_{n,c}$ corresponds to the maximum traction. More separation will result in a decrease of the interfacial stiffness (see Figure 2.1).

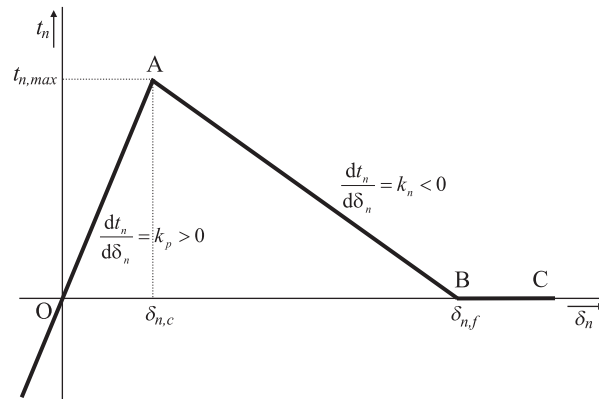


Figure 2.1: Bilinear traction-separation law.

The bi-linear TSL that is depicted in Figure 2.1 is defined by:

$$t_n(\delta_n) = \begin{cases} k_p \delta_n & \text{if } \delta_n \leq \delta_{n,c} \\ t_{n,max} + k_n(\delta_n - \delta_{n,c}) & \text{if } \delta_{n,c} < \delta_n \leq \delta_{n,f} \\ 0 & \text{if } \delta_n > \delta_{n,f} \end{cases} \quad (2.1)$$

in which $\delta_{n,f}$ is the failure separation. The slopes of the traction-separation curve in hardening and softening regimes are denoted by k_p and k_n , respectively; see Figure 2.1. The maximum normal traction is defined as:

$$t_{n,max} = k_p \delta_{n,c}. \quad (2.2)$$

Although unloading does not occur in the numerical examples considered further on, the behavior of the interface is irreversible upon unloading by following the secant stiffness [3].

The cohesive zone approach can be related to Griffith's theory of fracture, if the area under the traction-separation curve is equal to the corresponding fracture toughness G_c [101]. Assuming a fixed value of G_c for a certain fracture mode, a higher maximum traction would result in a smaller process zone and hence a more brittle interfacial behavior. In fact, maintaining a constant fracture toughness, an interface model is often interpreted as a regularization of the fracture mechanics singularity by planar lumping of the process zone [22]. In order to investigate the effect of the brittleness on the behavior of the cohesive zone models, two sets of constitutive parameters are used to characterize the interfacial behavior with respect to the level of brittleness, which is related to the size of the process zone (see Table 2.1).

Table 2.1: Cohesive zone parameters.

parameter set	characteristic separation $\delta_{n,c}$ (mm)	tensile strength $t_{n,max}$ (MPa)	fracture toughness G_c (N/mm)
1	0.002	50	0.25
2	0.001	100	0.25

The linear elastic bulk material is characterized by a stiffness of $C_{nn} = 27$ GPa in normal direction and zero shear stiffness, $C_{sn} = 0$ (to retrieve an easy analytical solution), and all displacements and/or separations occur in the normal direction. Figure 2.2 shows the geometry and boundary conditions. A linear normal displacement is prescribed in an incremental manner along the upper edge of the bulk layer as follows:

$$u(s) = \alpha \bar{u}(s) = \alpha \left(\bar{u}_L - \frac{\bar{u}_L - \bar{u}_R}{L} s \right), \quad 0 \leq \alpha \leq 1, \quad (2.3)$$

where the parameter α controls the magnitude of the prescribed displacement in the longitudinal direction denoted by s and where the prescribed displacement of the left and right top edge of the bulk layer are given by $\bar{u}_L = 0.0135$ mm and $\bar{u}_R = 0.0045$ mm, respectively.

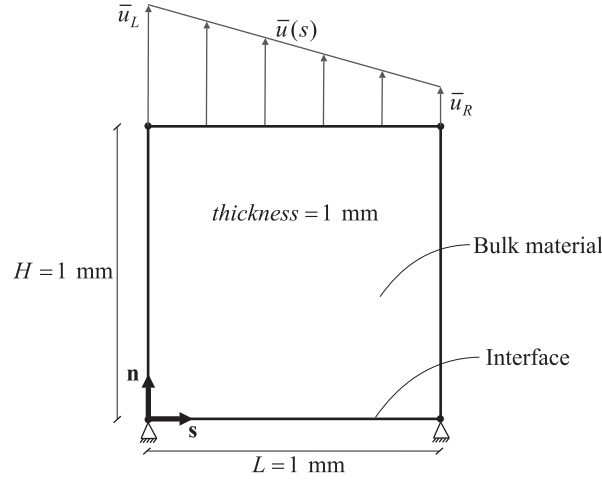


Figure 2.2: Mode I delamination; geometry and boundary conditions.

2.2.2 Analytical solution

An analytical solution of the peel-off problem is determined first. Due to the lack of shear stiffness in the bulk material, the constitutive relationship governing the displacement inside the bulk material can be written as

$$t_{bulk,n}(s) = E \epsilon_n(s), \quad (2.4)$$

where $\epsilon_n(s)$ is the normal strain within the bulk material. Equilibrium and compatibility equations for the whole domain imply:

$$t_{bulk,n}(s) - t_{cz,n}(s) = 0, \quad (2.5)$$

$$H \epsilon_n(s) + \delta_n(s) = u(s), \quad (2.6)$$

Assuming the condition ($E + H k_n > 0$) to avoid a physical solution jump, two unknowns, ϵ_n and δ_n , are calculated using the above equations:

$$\begin{bmatrix} \epsilon_n(s) \\ \delta_n(s) \end{bmatrix} = \begin{cases} \frac{1}{E + H k_p} \begin{bmatrix} k_p u(s) \\ E u(s) \end{bmatrix} & \text{if } \delta_n(u(s)) \leq \delta_{n,c} \\ \frac{1}{E + H k_n} \begin{bmatrix} t_{n,max} + k_n(u(s) - \delta_{n,c}) \\ E u(s) - H(t_{n,max} - k_n \delta_{n,c}) \end{bmatrix} & \text{if } \delta_{n,c} < \delta_n(u(s)) \leq \delta_{n,f} \\ \begin{bmatrix} 0 \\ u(s) \end{bmatrix} & \text{if } \delta_n(u(s)) > \delta_{n,f} \end{cases} \quad (2.7)$$

Next, the locations s_c and s_f along the interface in which the normal separation of the cohesive zone equals $\delta_{n,c}$ and $\delta_{n,f}$, respectively, are determined:

$$s_c = \frac{L}{u_L - u_R} \left(u_L - \frac{E + H k_p}{E} \delta_{n,c} \right), \quad (2.8a)$$

$$s_f = \frac{L}{u_L - u_R} \left(u_L - \frac{k_n - k_p}{k_n} \delta_{n,c} \right). \quad (2.8b)$$

Using Equations (2.7) and (2.8) and assuming that $u_L \geq u_R$, the behavior of the system with respect to the prescribed displacement can be identified in different stages, based on normal separations at left and right edges of the cohesive zone element, $\delta_{n,L} = \delta_n(0)$ and $\delta_{n,R} = \delta_n(L)$, respectively:

- $\delta_{n,L}, \delta_{n,R} \leq \delta_{n,c}$: The whole interface is intact; that is, no reduction in interface stiffness (or any damage) has occurred, which implies that the response is linear (see Figure 2.3(a)).
- $\delta_{n,c} < \delta_{n,L} \leq \delta_{n,f}$ and $\delta_{n,R} < \delta_{n,c}$: The left edge of the interface has started softening but has not failed yet while the right edge is intact, which implies that the separation profile is bi-linear (see Figure 2.3(b)).
- $\delta_{n,L} > \delta_{n,f}$ and $\delta_{n,R} < \delta_{n,c}$: The left edge of the interface has failed while the right edge is intact. The separation profile becomes tri-linear (see Figure 2.3(c)).
- $\delta_{n,L} \geq \delta_{n,f}$ and $\delta_{n,c} \leq \delta_{n,R} < \delta_{n,f}$: The left edge of the interface has failed while the right edge is softening but did not fail yet. The separation profile throughout the interface is bi-linear (see Figure 2.3(d)).
- $\delta_{n,L}, \delta_{n,R} \geq \delta_{n,f}$: The whole interface has failed which implies that the separation profile is linear (see Figure 2.3(e)).

2.2.3 Numerical solution

For the problem sketched in Figure 2.2, the bulk material domain is discretized uniformly along the s -axis by one layer of quadrilateral 4-node elements while cohesive zone elements are placed between bulk elements and the rigid substrate. First, a coarse mesh of 10 non-enriched (standard) bulk and interface elements in the longitudinal direction is used for both parameter sets described in Table 2.1. The variation of the total applied force on the upper edge of the bulk material with respect to the prescribed displacement at the same edge is illustrated in Figure 2.4, revealing oscillations in the response of the parameter set 2. A finer mesh of 100 standard bulk and interface elements is also used for the same set of parameters. As can be seen in Figure 2.4, the numerical solution obtained with the coarse mesh oscillates around the smooth refined solution, as expected.

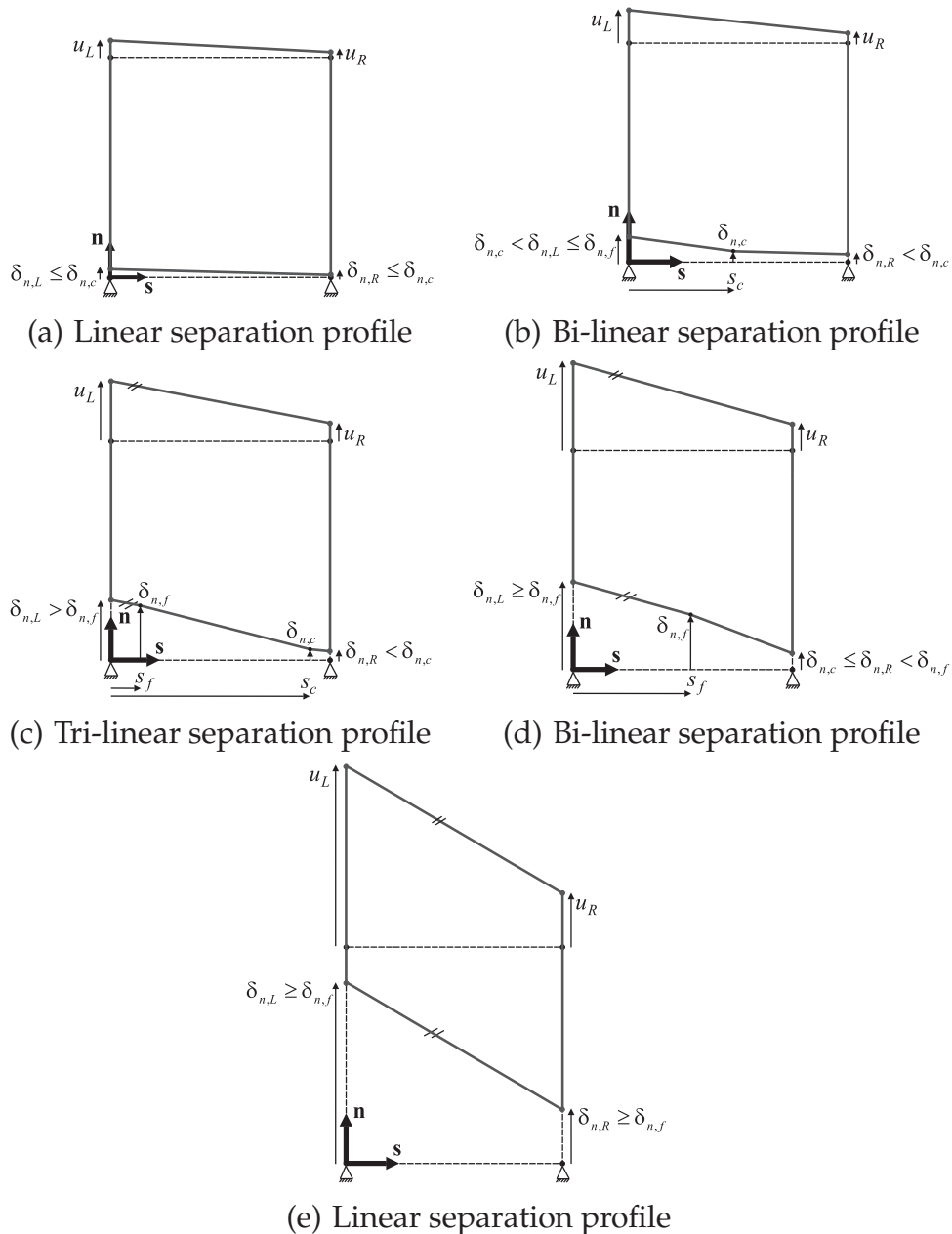


Figure 2.3: Peel-off test; analytical opening profile in different stages of interface opening.

The oscillations observed in the global load-displacement behavior of the system discretized by a coarse mesh (see Figure 2.4) directly result from the inaccurate separation approximation in the cohesive zone. In other words, the number of nodes in the process zone is too small to describe the process zone accurately for the relatively brittle interface. Figure 2.4 also shows that reducing the initial stiffness of the interface while maintaining a constant fracture toughness (i.e. increasing the characteristic separation, $\delta_{n,c}$) does eliminate the oscillations observed but unrealistically underestimates the peak in the global load-displacement behavior.

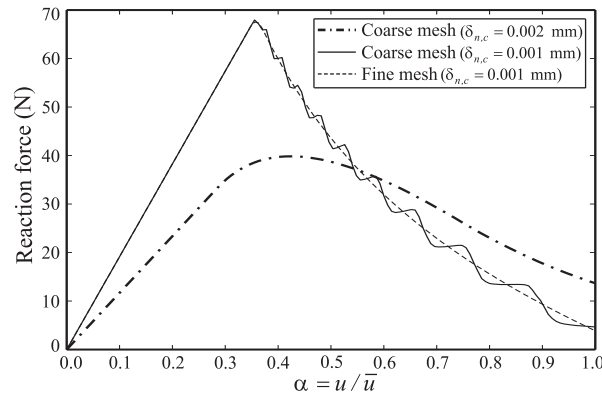


Figure 2.4: Force-displacement responses of the peel-off problem without enrichment.

2.3 Cohesive zone enrichment

The finite element formulation of both interface and bulk material will be enriched in order to more accurately describe the opening profile of a crack. This improvement should result in a reduction of the non-smoothness observed in the general load-displacement behavior of the system which is an artifact of the discretization of the opening profile. In fact, as delamination propagates in brittle interfaces, the strain field in the process zone should be captured with enough accuracy to avoid a sudden release of the elastic strain energy stored in the surrounding bulk material, which in turn results in a snap-back response in the numerical solution. This can be avoided by refining the mesh in the process zone or by using an enriched model that can predict the position of the discontinuity in the strain field.

2.3.1 Interface elements

The separation approximation of the cohesive zone element will be enriched to improve the separation approximation in the process zone of a cohesive crack (see Figure 2.5).

The most obvious enrichment is presented in Figure 2.6, where a linear separation approximation is enriched by adding a piecewise linear enrichment function multiplied by enrichment scaling factors to determine the magnitude of the enrichment at the top and bottom edges of the interface element. The bi-linear enrichment function, ϕ , is defined as:

$$\phi = \frac{1}{a} \xi - \frac{1}{a(1-a)} \mathcal{R}(\xi - a), \quad (2.9)$$

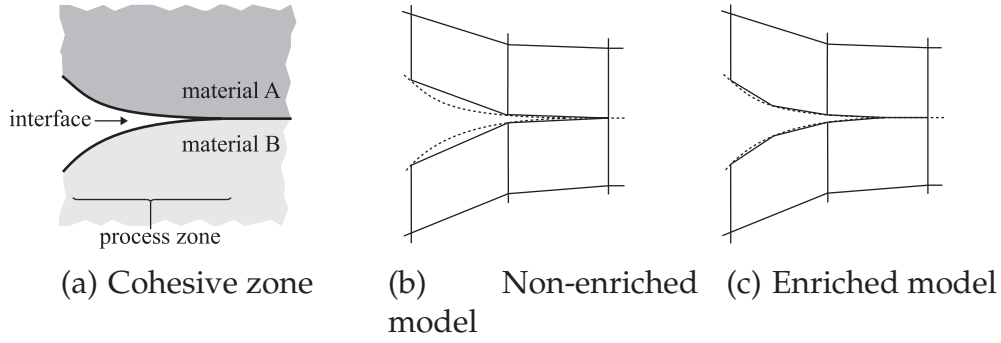


Figure 2.5: Schematic representation of a cohesive zone and its discretization.

with the ramp function, \mathcal{R} , defined as:

$$\mathcal{R}(\xi - a) = \begin{cases} 0 & \text{if } \xi \leq a \\ \xi - a & \text{if } \xi > a \end{cases}, \quad (2.10)$$

where $\xi \in [0, 1]$ represents the non-dimensional coordinate:

$$\xi = \frac{s}{L}, \quad (2.11)$$

where L is the length of the cohesive zone element in the initial configuration. The enrichment peak position inside the cohesive zone element is denoted by a which is considered to depend on an additional degree of freedom. The enrichment function becomes singular when the enrichment peak approaches the interface element boundaries $\xi = 0$ or $\xi = 1$. On the other hand, in such situations the proposed enrichment is not required anymore since a linear opening profile remains. Therefore, an auxiliary parameter z is defined as a degree of freedom such that the peak of the bi-linear enrichment function is forced to remain inside the cohesive zone element:

$$a = \frac{1}{2} + \frac{1}{\pi} \arctan(z). \quad (2.12)$$

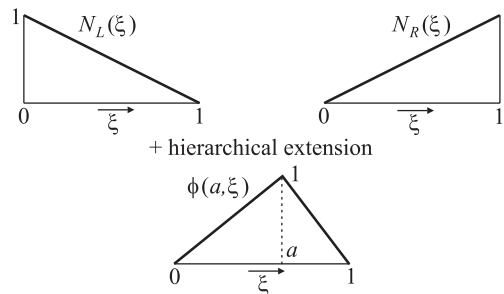


Figure 2.6: Hierarchical enrichment of standard linear finite element interpolation functions with a bi-linear enrichment function.

The two-dimensional conventional interface element depicted in Figure 2.7(a), is characterized by a traction-separation relationship in normal direction (see Section 2.2.1). Here, no shear separation is considered. The cohesive zone element has zero thickness in the undeformed state where the normal separation δ_n is zero throughout the element. Element coordinates $\{s, n\}$ are defined with the shear or tangential direction, s , oriented along the edge from node 1 to node 2 in the initial configuration, and the normal direction n perpendicular to the shear direction. As can be seen in Figure 2.7(b), the piecewise linear function is employed to enrich the normal separation approximation which corresponds to mode I delamination.

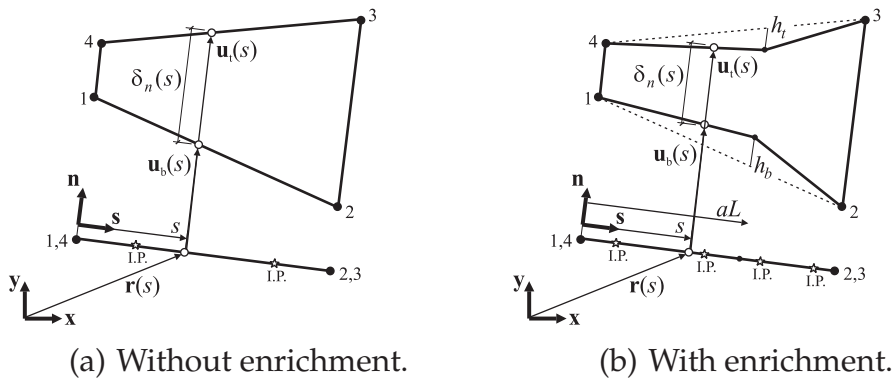


Figure 2.7: Deformation of a cohesive zone element.

In the enriched cohesive zone element, displacements at the top and bottom edges along the normal direction, $u_{n,t}$ and $u_{n,b}$ respectively, are approximated by:

$$u_{n,t} = N_L u_{n,4} + N_R u_{n,3} + \phi h_t, \quad (2.13a)$$

$$u_{n,b} = N_L u_{n,1} + N_R u_{n,2} + \phi h_b, \quad (2.13b)$$

where h_t and h_b are unknown enrichment scaling factors for the top and bottom edges of the interface element, respectively. The subscripts L and R refer to the left and right edges of the cohesive zone element, respectively. The linear interpolation functions depicted in Figure 2.6 are defined as:

$$N_L = 1 - \xi, \quad (2.14a)$$

$$N_R = \xi. \quad (2.14b)$$

The field variable of interest is the normal separation of cohesive surfaces which can be expressed as:

$$\delta_n = u_{n,t} - u_{n,b} = \underline{B}_{u,cz} \underline{u} + \underline{B}_{h,cz} \underline{h}, \quad (2.15a)$$

with

$$\underline{B}_{u,cz} = \begin{bmatrix} -N_L & -N_R & N_R & N_L \end{bmatrix}, \quad (2.15b)$$

$$\underline{u}^T = [u_{n,1} \quad u_{n,2} \quad u_{n,3} \quad u_{n,4}], \quad (2.15c)$$

$$\underline{B}_{h,cz} = [-\phi \quad \phi], \quad (2.15d)$$

$$\underline{h}^T = [h_b \quad h_t]. \quad (2.15e)$$

The equilibrium equation for a cohesive zone element can be written as:

$$t_n(s) = \begin{cases} \bar{t}_{n,t}(s) & \text{at the top edge} \\ \bar{t}_{n,b}(s) & \text{at the bottom edge} \end{cases}, \quad (2.16)$$

where $\bar{t}_{n,t}(s)$ and $\bar{t}_{n,b}(s)$ represent the external normal traction at the top and bottom edges of the cohesive zone element, respectively, which establish the equilibrium after the cohesive zone element is separated from the rest of the model. The principle of virtual work is used to establish the weak form of the equilibrium equations and is valid for nonlinear as well as linear stress-strain relations. Application of this principle in the present cohesive zone model states that for an arbitrary small normal separation perturbation $d\delta_n$, the work done by the internal forces equals the work done by the external forces. It can be expressed as:

$$\int_{\Gamma} d\delta_n t_n d\Gamma = \int_{\Gamma} (du_{n,t} \bar{t}_{n,t} + du_{n,b} \bar{t}_{n,b}) d\Gamma, \quad (2.17)$$

where $du_{n,t}$ and $du_{n,b}$ represent the normal displacement perturbations at the top and bottom edges, respectively. The normal separation perturbation $d\delta_n$ can be expressed as:

$$\begin{aligned} d\delta_n &= \frac{\partial \delta_n}{\partial \underline{u}} d\underline{u} + \frac{\partial \delta_n}{\partial \underline{h}} d\underline{h} + \frac{\partial \delta_n}{\partial \phi} \frac{\partial \phi}{\partial a} \frac{\partial a}{\partial z} dz \\ &= \underline{B}_{u,cz} d\underline{u} + \underline{B}_{h,cz} d\underline{h} + B_{z,cz} dz, \end{aligned} \quad (2.18)$$

where:

$$B_{z,cz} = \frac{\partial(\underline{B}_{h,cz} \underline{h})}{\partial a} \frac{da}{dz} = \frac{da}{dz} B_{a,cz}, \quad (2.19a)$$

$$B_{a,cz} = \left[-\frac{\partial \phi}{\partial a} \quad \frac{\partial \phi}{\partial a} \right] \underline{h}. \quad (2.19b)$$

Substitution of the relations for the normal separation perturbation in the principle of virtual work (Equation (2.17)) results in the following expression:

$$d\underline{u}^T \underline{f}_{i,cz} + d\underline{h}^T \underline{g}_{i,cz} + dz b_{i,cz} = d\underline{u}^T \underline{f}_{e,cz} + d\underline{h}^T \underline{g}_{e,cz} + dz b_{e,cz}. \quad (2.20)$$

In the above expression, $\underline{f}_{i,cz}$, $\underline{g}_{i,cz}$, and $b_{i,cz}$ collect the internal forces adjoint to nodal displacements, \underline{u} , enrichment scaling factors, \underline{h} , and the auxiliary parameter, z (which defines the position of the enrichment peak, a , by Equation (2.12)), respectively. External forces are collected in $\underline{f}_{e,cz}$, $\underline{g}_{e,cz}$, and $b_{e,cz}$. The internal forces are defined as:

$$\underline{f}_{i,cz} = \int_{\Gamma} \underline{B}_{u,cz}^T t_n \, d\Gamma, \quad (2.21a)$$

$$\underline{g}_{i,cz} = \int_{\Gamma} \underline{B}_{h,cz}^T t_n \, d\Gamma, \quad (2.21b)$$

$$b_{i,cz} = \int_{\Gamma} B_{z,cz} t_n \, d\Gamma. \quad (2.21c)$$

The equilibrium Equation (2.20) should hold for arbitrary nodal displacement perturbations, du , arbitrary perturbations of enrichment scaling factors, dh , and arbitrary perturbations of the position of the enrichment peak, da (or equivalently, dz). A derivation of the tangential stiffness matrix is given in Section 2.7. In order to calculate the stiffness matrix and internal force components, a Gauss integration scheme is adopted, where in the case of an enriched cohesive zone element, integration is carried out in both parts of the element separated by the enrichment peak (see Figure 2.7(b) where the location of integration points are indicated by I.P.).

The TSL is defined in local (element) coordinates $\{s, n\}$ whereas nodal coordinates and displacement degrees of freedom are defined in global (cartesian) coordinates $\{x, y\}$. Before the global assembly of the system, all vectorial field variables derived in element coordinates are converted to the global coordinates in a standard manner.

2.3.2 Bulk elements

Two-dimensional 4-node quadrilateral elements are used to model the bulk material (see Figure 2.8(a)). Similar to the cohesive zone elements, field variables in the bulk elements are described in a cartesian coordinate system with the basis $\{s, n\}$ which is aligned with the cohesive zone element coordinates. Only displacements in n -direction, u_n , between the undeformed state and the deformed state of a material point, are considered, and hence, the strain field in a two-dimensional configuration considering the small strain/displacement framework will be identified as:

$$\underline{\epsilon}(\mathbf{r}) = \begin{bmatrix} \epsilon_n(s, n) \\ \gamma_{sn}(s, n) \end{bmatrix} = \begin{bmatrix} \partial u_n / \partial n \\ \partial u_n / \partial s \end{bmatrix}. \quad (2.22)$$

Ignoring body forces in the continuum, the standard static equilibrium equation with respect to $\{s, n\}$ is given by:

$$\frac{\partial \sigma_n}{\partial n} + \frac{\partial \tau_{sn}}{\partial s} = 0, \quad (2.23)$$

where the constitutive behavior of the bulk material is defined as

$$\underline{\sigma} = \begin{bmatrix} \sigma_n(s, n) \\ \tau_{sn}(s, n) \end{bmatrix} = \underline{f}(\underline{\epsilon}). \quad (2.24)$$

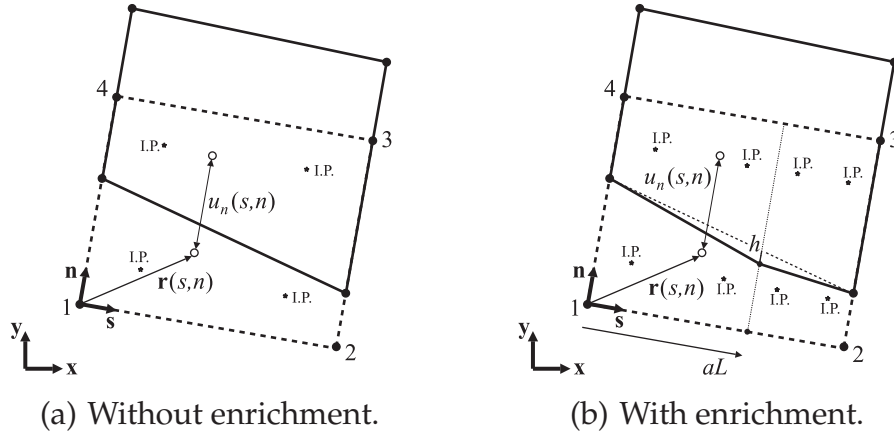


Figure 2.8: Deformation of a 2-D bulk element.

As mentioned earlier, continuity of the displacement field requires that bulk elements adjacent to the enriched cohesive zone elements be enriched as well (see Figure 2.8(b)). Therefore, a weighted piecewise linear enrichment function, ϕ , added to the weighted sum of interpolation functions N_i , approximates the displacement along the normal direction in the enriched model discussed here:

$$u_n = \underline{N} \underline{u} + \psi h, \quad (2.25a)$$

$$\underline{N} = [N_1 \quad N_2 \quad N_3 \quad N_4], \quad (2.25b)$$

$$\underline{u}^T = [u_{n,1} \quad u_{n,2} \quad u_{n,3} \quad u_{n,4}], \quad (2.25c)$$

where the interpolation and enrichment functions are defined by using normalized coordinates, $\xi, \eta \in [0, 1]$ with the origin in node 1:

$$N_1 = (1 - \xi)(1 - \eta), \quad (2.26a)$$

$$N_2 = \xi(1 - \eta), \quad (2.26b)$$

$$N_3 = \xi\eta, \quad (2.26c)$$

$$N_4 = (1 - \xi)\eta, \quad (2.26d)$$

$$\psi = (1 - \eta)\phi. \quad (2.26e)$$

The enrichment function, ϕ , is defined in Equation (2.9). Using Equations (2.22) and (2.25a), the strain field in the bulk material can be approximated as follows:

$$\underline{\epsilon}(\mathbf{r}) = \begin{bmatrix} \epsilon_n(s, n) \\ \gamma_{sn}(s, n) \end{bmatrix} = \underline{B}_{u,bulk} \underline{u} + \underline{B}_{h,bulk} h, \quad (2.27a)$$

where:

$$\underline{B}_{u,bulk} = \begin{bmatrix} \partial N_1/\partial n & \partial N_2/\partial n & \partial N_3/\partial n & \partial N_4/\partial n \\ \partial N_1/\partial s & \partial N_2/\partial s & \partial N_3/\partial s & \partial N_4/\partial s \end{bmatrix}, \quad (2.27b)$$

$$\underline{B}_{h,bulk} = \begin{bmatrix} \partial\psi/\partial n \\ \partial\psi/\partial s \end{bmatrix}. \quad (2.27c)$$

The displacement approximation and the subsequent strain approximation are compatible with the neighboring cohesive zone element and other conventional bulk elements. Equilibrium conditions are enforced in an integral way by application of the principle of virtual work, which can be expressed as

$$\int_{\Omega} d\tilde{\epsilon}^T \tilde{\sigma} d\Omega = \int_{\Gamma} d\tilde{u}^T \tilde{t} d\Gamma, \quad (2.28)$$

where $d\tilde{\epsilon}$ represents a small strain perturbation and Γ represents the circumferential boundary coordinate. The external forces are denoted by \tilde{t} which includes all forces that establish equilibrium if the element is isolated from the surrounding material. The small strain perturbation can be written as:

$$\begin{aligned} d\tilde{\epsilon} &= \frac{\partial\tilde{\epsilon}}{\partial u} du + \frac{\partial\tilde{\epsilon}}{\partial h} dh + \frac{\partial\tilde{\epsilon}}{\partial\psi} \frac{\partial\psi}{\partial a} \frac{\partial a}{\partial z} dz \\ &= \underline{B}_{u,bulk} du + \underline{B}_{h,bulk} dh + \underline{B}_{z,bulk} dz, \end{aligned} \quad (2.29)$$

where:

$$\underline{B}_{z,bulk} = \frac{\partial(\underline{B}_{h,bulk} h)}{\partial a} \frac{da}{dz} = \frac{da}{dz} \underline{B}_{a,bulk}, \quad (2.30a)$$

$$\underline{B}_{a,bulk} = \begin{bmatrix} \partial^2\psi/\partial n \partial a \\ \partial^2\psi/\partial s \partial a \end{bmatrix} h. \quad (2.30b)$$

Substitution of the relations for the strain perturbation in the principle of virtual work (Equation (2.28)) results in the following expression:

$$d\tilde{u}^T \underline{f}_{i,bulk} + dh g_{i,bulk} + dz b_{i,bulk} = d\tilde{u}^T \underline{f}_{e,bulk} + dh g_{e,bulk} + dz b_{e,bulk}. \quad (2.31)$$

In the above expression, $\underline{f}_{i,bulk}$, $g_{i,bulk}$, and $b_{i,bulk}$ collect the internal forces adjoint to nodal displacements, u , the enrichment scaling factor, h , and the auxiliary parameter, z , respectively. External forces are collected by $\underline{f}_{e,bulk}$, $g_{e,bulk}$, and $b_{e,bulk}$. The internal forces are defined as:

$$\underline{f}_{i,bulk} = \int_{\Omega} \underline{B}_{u,bulk}^T \tilde{\sigma} d\Omega, \quad (2.32a)$$

$$g_{i,bulk} = \int_{\Omega} \underline{B}_{h,bulk}^T \underline{\varrho} \, d\Omega, \quad (2.32b)$$

$$b_{i,bulk} = \int_{\Omega} \underline{B}_{z,bulk}^T \underline{\varrho} \, d\Omega. \quad (2.32c)$$

The equilibrium Equation (2.31) should hold for arbitrary nodal displacement perturbations, dy , arbitrary perturbations of the enrichment scaling factor, dh , and arbitrary perturbations of the position of the enrichment peak, da (or equivalently, dz). A derivation of the tangential stiffness matrix is given in Section 2.7. In order to calculate the stiffness matrix and internal force components, a Gauss numerical integration scheme is adopted, where in the case of an enriched bulk element, integration is carried out in both parts of the element separated by the enrichment peak (see Figure 2.8(b)).

2.4 Implementation aspects

2.4.1 Penalty factor

The considered cohesive zone element separation profile remains linear when the whole interface within an element is still intact or the whole element is failed or when the element is entirely within the process zone. In such cases, no discontinuity is present in the separation profile within the cohesive zone element; and hence, an enrichment is not required. The linear solution is retrieved when the scaling factors are zero and in that case the solution is not affected by the value of a , which remains undetermined. Therefore, no unique solution exists. In order to obtain a unique solution, a penalty term based on the discontinuity position, a , is added to the total potential of the system, Π :

$$\bar{\Pi} = \Pi + p(a - \bar{a})^2, \quad (2.33)$$

where p is a small penalty factor and \bar{a} is an arbitrary fixed position within the cohesive zone element; i.e., the middle of the element. The additional term, $p(a - \bar{a})^2$, is to be taken sufficiently small in order not to influence the solution in the physical sense if the crack tip passes through the cohesive zone element.

2.4.2 Adaptive enrichment strategy

Enrichment of all interface elements and their neighboring bulk elements results in a large increase of the total number of degrees of freedom. However, interface elements that are still intact or those that have already failed do not need to be enriched. Therefore, only the elements located within the process zone are enriched and the rest remain non-enriched. For this purpose, at the start of each increment, the following enrichment scheme based on the results obtained from the previous one, is used:

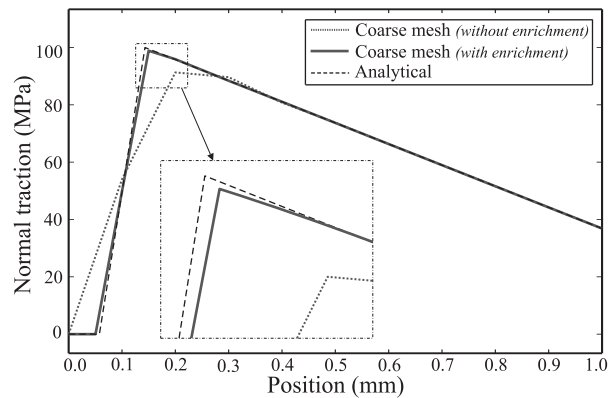
- $\delta_n(s) \leq \varrho \delta_{n,c} ; \forall s \in [0, L]$: The entire interface element is in the linear hardening regime which implies that an enrichment is not required. The coefficient $\varrho \in [0, 1]$ is defined with respect to the size of increments to ensure that enrichment in an element is switched on when necessary.
- $\delta_n(s) \geq \delta_{n,f} ; \forall s \in [0, L]$: The entire interface element is failed and an enrichment is not required anymore; hence, prior enrichment degrees of freedom are removed.
- $\varrho \delta_{n,c} < \delta_n(s) < \delta_{n,f} ; \forall s \in [0, L]$: Due to the near existence of a piece-wise linear separation profile, an enrichment is activated in the interface element.

The scheme remains unchanged throughout all iterations performed in an increment. At the end of the increment, the enrichment scheme is updated; i.e. as delamination grows, the enrichment in some elements is activated, whereas it is de-activated in failed elements. As a result, the total number of degrees of freedom and the column of degrees of freedom may slightly vary from increment to increment in order to enhance the efficiency of the proposed technique, but their total amount remains limited. An adaptive enrichment strategy is particularly beneficial when analyzing domains including several interfaces where multiple cracks may develop simultaneously.

2.5 Application to the example problem

In the simplified mode I delamination example explained in Section 2.2, the new enrichment scheme is used to improve the response obtained from the cohesive zone model. Figure 2.9 shows the interfacial separation profile and the traction along the interface characterized by parameter set 2 of Table 2.1 for an applied load given by $\alpha = u/\bar{u} = 0.39$. A coarse mesh of 10 bulk and interface elements in the longitudinal direction is used for the numerical simulation, for which both standard and enriched elements have been used. The enriched case clearly shows a more accurate traction profile compared to the standard case (see Figure 2.9(a)). Likewise, the enriched separation profile (Figure 2.9(b)) is obviously close to the analytical solution (Figure 2.9(d)) in contrast to the standard case (Figure 2.9(c)).

Local enrichment of the kinematics of the cohesive zone element improves the oscillatory behavior noticed in Figure 2.4 (parameter set 2, 10 bulk/interface elements). Figure 2.10 shows that the enrichment considerably reduces the oscillations that occur around the exact solution of the problem. The minor remaining oscillations in the numerical response of the enriched model are due to the presence of a tri-linear separation regime inside interface elements, especially at the last stages of loading (see Section 2.2.2). Here, the response obtained from the analytical solution is used as a reference. The adaptive enrichment strategy significantly improves the results whereas the total number of degrees of freedom is only slightly and locally increased.



(a) Traction profiles.



(b) Separation profile; coarse mesh without enrichment.



(c) Separation profile; coarse mesh with enrichment.



(d) Analytical separation profile.

Figure 2.9: Interfacial traction and separation profiles of the peel-off problem when $\alpha = 0.39$.

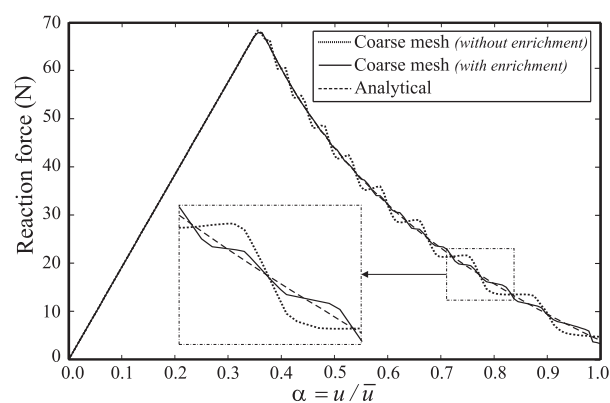


Figure 2.10: Force-displacement responses of the peel-off problem with and without enrichment.

2.6 Discussion and conclusion

Cohesive zone models have the appealing feature of predicting both delamination initiation and growth. These models are also linked to traditional fracture mechan-

ics by relating the traction at the interface to the separation through a non-linear softening relationship, for which the area under the traction-separation curve equals the fracture toughness. However, application of these models to brittle interfaces is accompanied by some numerical difficulties. The oscillatory load-displacement behavior that is often observed for such interfaces is an artifact of the relatively coarse mesh size (with respect to interface parameters) and can break down the computations unless complicated path-following techniques are employed. On the other hand, using a sufficiently refined mesh so that the separation field of a cohesive crack is approximated with acceptable accuracy, results in a noticeable increase in the size of the computations. The discretization-induced oscillations are not affected by the integration scheme even when an analytical integration of cohesive zone elements is carried out. Application of an enrichment to the conventional model considerably enhances the robustness of cohesive zone models, thereby avoiding an expensive mesh refinement.

To this purpose, an adaptive hierarchical extension has been presented to enrich the separation approximation in the process zone of a cohesive crack. In the proposed formulation, the linear separation approximation throughout the cohesive zone element is enriched by a piece-wise linear function. The finite element formulation of the enriched bulk and interface elements is elaborated and an adaptive enrichment strategy is used for a maximum efficiency. The numerical example shows that the proposed enrichment scheme improves the global load displacement response of the system discretized by a relatively coarse mesh without a need for further mesh refinement.

In the formulation, the peak point of the enrichment function can be located at any arbitrary position within an interface element. The position and scaling factor used in the enrichment function are treated as additional degrees of freedom. The moving peak of the bi-linear enrichment function relates to the moving process zone and provides a more accurate numerical approximation of the physical problem where delamination grows in an interface. This feature makes the new enrichment scheme distinct from conventional hierarchical enrichments where only scaling factors associated with higher order enrichment functions are calculated while the crack tip position is prescribed beforehand. Whereas an X-FEM approach relies on a position of the crack tip to be prescribed inside an element or from element edge to edge, the moving discontinuity in the proposed methodology naturally retrieves this position from the global solution of the equilibrium equations.

Using the current bi-linear enrichment function, a tri-linear separation profile within a single interface element can only be captured approximately, which may leave minor oscillations remaining in the load-displacement response of bi-linear enriched systems. However, the proposed methodology is well-suited to be extended to other enrichments as well, allowing for more complex separation profiles within a single cohesive zone element. The limit case of the proposed enrichment scheme with a tri-linear interpolation for an infinitely stiff interface corresponds to a strong discontinuity.

2.7 Appendix A: Determination of the tangential stiffness matrix

The tangential stiffness matrix of the cohesive zone element used in the non-linear solution procedure contains the derivatives of the internal forces with respect to the element degrees of freedom:

$$\underline{K}_{cz} = \begin{bmatrix} \underline{K}_{uu,cz} & \underline{K}_{uh,cz} & \underline{K}_{uz,cz} \\ \underline{K}_{hu,cz} & \underline{K}_{hh,cz} & \underline{K}_{hz,cz} \\ \underline{K}_{zu,cz} & \underline{K}_{zh,cz} & \underline{K}_{zz,cz} \end{bmatrix}, \quad (2.34a)$$

where:

$$\begin{aligned} \underline{K}_{uu,cz} &= \frac{\partial f_{i,cz}}{\partial \underline{u}} = \int_{\Gamma} \frac{\partial}{\partial \underline{u}} (\underline{B}_{u,cz}^T t_n) \, d\Gamma = \int_{\Gamma} \underline{B}_{u,cz}^T \frac{\partial t_n}{\partial \delta_n} \frac{\partial \delta_n}{\partial \underline{u}} \, d\Gamma \\ &= \int_{\Gamma} \underline{B}_{u,cz}^T \frac{\partial t_n}{\partial \delta_n} \underline{B}_{u,cz} \, d\Gamma, \end{aligned} \quad (2.34b)$$

$$\begin{aligned} \underline{K}_{hu,cz} &= \frac{\partial g_{i,cz}}{\partial \underline{u}} = \int_{\Gamma} \frac{\partial}{\partial \underline{u}} (\underline{B}_{h,cz}^T t_n) \, d\Gamma = \int_{\Gamma} \underline{B}_{h,cz}^T \frac{\partial t_n}{\partial \delta_n} \frac{\partial \delta_n}{\partial \underline{u}} \, d\Gamma \\ &= \int_{\Gamma} \underline{B}_{h,cz}^T \frac{\partial t_n}{\partial \delta_n} \underline{B}_{u,cz} \, d\Gamma, \end{aligned} \quad (2.34c)$$

$$\underline{K}_{uh,cz} = \underline{K}_{hu,cz}^T, \quad (2.34d)$$

$$\begin{aligned} \underline{K}_{zu,cz} &= \frac{\partial b_{i,cz}}{\partial \underline{u}} = \int_{\Gamma} \frac{\partial}{\partial \underline{u}} (B_{z,cz} t_n) \, d\Gamma = \int_{\Gamma} B_{z,cz} \frac{\partial t_n}{\partial \delta_n} \frac{\partial \delta_n}{\partial \underline{u}} \, d\Gamma \\ &= \int_{\Gamma} B_{z,cz} \frac{\partial t_n}{\partial \delta_n} \underline{B}_{u,cz} \, d\Gamma, \end{aligned} \quad (2.34e)$$

$$\underline{K}_{uz,cz} = \underline{K}_{zu,cz}^T, \quad (2.34f)$$

$$\begin{aligned} \underline{K}_{hh,cz} &= \frac{\partial g_{i,cz}}{\partial \underline{h}} = \int_{\Gamma} \frac{\partial}{\partial \underline{h}} (\underline{B}_{h,cz}^T t_n) \, d\Gamma = \int_{\Gamma} \underline{B}_{h,cz}^T \frac{\partial t_n}{\partial \delta_n} \frac{\partial \delta_n}{\partial \underline{h}} \, d\Gamma \\ &= \int_{\Gamma} \underline{B}_{h,cz}^T \frac{\partial t_n}{\partial \delta_n} \underline{B}_{h,cz} \, d\Gamma, \end{aligned} \quad (2.34g)$$

$$\begin{aligned} \underline{K}_{zh,cz} &= \frac{\partial b_{i,cz}}{\partial \underline{h}} = \int_{\Gamma} \frac{\partial}{\partial \underline{h}} (B_{z,cz} t_n) \, d\Gamma = \int_{\Gamma} \left(B_{z,cz} \frac{\partial t_n}{\partial \delta_n} \frac{\partial \delta_n}{\partial \underline{h}} + \frac{\partial B_{z,cz}}{\partial \underline{h}} t_n \right) \, d\Gamma \\ &= \int_{\Gamma} \left(B_{z,cz} \frac{\partial t_n}{\partial \delta_n} \underline{B}_{h,cz} + \frac{da}{dz} \frac{\partial \underline{B}_{h,cz}}{\partial a} t_n \right) \, d\Gamma, \end{aligned} \quad (2.34h)$$

$$\underline{K}_{hz,cz} = \underline{K}_{zh,cz}^T, \quad (2.34i)$$

$$\begin{aligned}
K_{zz,cz} &= \frac{\partial b_{i,cz}}{\partial z} = \int_{\Gamma} \frac{\partial}{\partial z} (B_{z,cz} t_n) d\Gamma = \int_{\Gamma} \left(B_{z,cz} \frac{\partial t_n}{\partial \delta_n} \frac{\partial \delta_n}{\partial z} + \frac{\partial B_{z,cz}}{\partial z} t_n \right) d\Gamma \\
&= \int_{\Gamma} \left(B_{z,cz} \frac{\partial t_n}{\partial \delta_n} B_{z,cz} + \frac{d^2 a}{dz^2} B_{a,cz} t_n + \left(\frac{da}{dz} \right)^2 \frac{\partial B_{a,cz}}{\partial a} t_n \right) d\Gamma.
\end{aligned} \tag{2.34j}$$

The following derivatives in the above formulation can be obtained as:

$$\frac{\partial t_n}{\partial \delta_n} = \begin{cases} k_p & \text{if } \delta_n \leq \delta_{n,c} \\ k_n & \text{if } \delta_{n,c} < \delta_n \leq \delta_{n,f} \\ 0 & \text{if } \delta_n > \delta_{n,f} \end{cases}, \tag{2.35a}$$

$$\frac{\partial B_{h,cz}}{\partial a} = \begin{bmatrix} -\frac{\partial \phi}{\partial a} & \frac{\partial \phi}{\partial a} \end{bmatrix}, \tag{2.35b}$$

$$\frac{\partial B_{a,cz}}{\partial a} = \begin{bmatrix} -\frac{\partial^2 \phi}{\partial a^2} & \frac{\partial^2 \phi}{\partial a^2} \end{bmatrix} \underline{h}. \tag{2.35c}$$

Assuming a linear elastic material, the constitutive relation of the bulk material (Equation (2.24)) in the case of plane strain conditions can be stated as follows:

$$\boldsymbol{\sigma}(\mathbf{r}) = \underline{\underline{H}} \boldsymbol{\varepsilon}(\mathbf{r}), \tag{2.36}$$

where $\underline{\underline{H}}$ is the material moduli matrix. In general, the constitutive relation for the bulk material can be non-linear and the above assumptions are made for the sake of simplicity. The tangential stiffness matrix of the bulk element contains the derivatives of the internal forces with respect to the element degrees of freedom:

$$\underline{\underline{K}}_{bulk} = \begin{bmatrix} \underline{K}_{uu,bulk} & \underline{K}_{uh,bulk} & \underline{K}_{uz,bulk} \\ \underline{K}_{hu,bulk} & \underline{K}_{hh,bulk} & \underline{K}_{hz,bulk} \\ \underline{K}_{zu,bulk} & \underline{K}_{zh,bulk} & \underline{K}_{zz,bulk} \end{bmatrix}. \tag{2.37a}$$

where:

$$\underline{K}_{uu,bulk} = \frac{\partial f_{i,bulk}}{\partial u} = \int_{\Omega} \underline{B}_{u,bulk}^T \underline{\underline{H}} \underline{B}_{u,bulk} d\Omega, \tag{2.37b}$$

$$\underline{K}_{uh,bulk} = \frac{\partial f_{i,bulk}}{\partial h} = \int_{\Omega} \underline{B}_{u,bulk}^T \underline{\underline{H}} \underline{B}_{h,bulk} d\Omega, \tag{2.37c}$$

$$\underline{K}_{hu,bulk} = \underline{K}_{uh,bulk}^T, \tag{2.37d}$$

$$\underline{K}_{uz,bulk} = \frac{\partial f_{i,bulk}}{\partial z} = \int_{\Omega} \underline{B}_{u,bulk}^T \underline{\underline{H}} \underline{B}_{z,bulk} d\Omega, \tag{2.37e}$$

$$\underline{K}_{zu,bulk} = \underline{K}_{uz,bulk}^T, \tag{2.37f}$$

$$\underline{K}_{hh,bulk} = \frac{\partial g_{i,bulk}}{\partial h} = \int_{\Omega} \underline{B}_{h,bulk}^T \underline{\underline{H}} \underline{B}_{h,bulk} d\Omega, \tag{2.37g}$$

$$\begin{aligned}
K_{hz,bulk} &= \frac{\partial g_{i,bulk}}{\partial z} = \frac{\partial g_{i,bulk}}{\partial a} \frac{da}{dz} \\
&= \frac{da}{dz} \int_{\Omega} \left(\frac{\partial \underline{B}_{h,bulk}^T}{\partial a} \underline{H} \underline{\epsilon} + \underline{B}_{h,bulk}^T \underline{H} \underline{B}_{a,bulk} \right) d\Omega, \tag{2.37h}
\end{aligned}$$

$$K_{zh,bulk} = K_{hz,bulk}, \tag{2.37i}$$

$$\begin{aligned}
K_{zz,bulk} &= \frac{\partial b_{i,bulk}}{\partial z} = \frac{d^2 a}{dz^2} \int_{\Omega} \underline{B}_{a,bulk}^T \underline{H} \underline{\epsilon} d\Omega \\
&\quad + \left(\frac{da}{dz} \right)^2 \int_{\Omega} \frac{\partial \underline{B}_{a,bulk}^T}{\partial a} \underline{H} \underline{\epsilon} d\Omega \\
&\quad + \int_{\Omega} \underline{B}_{z,bulk}^T \underline{H} \underline{B}_{z,bulk} d\Omega. \tag{2.37j}
\end{aligned}$$

In the above formulation:

$$\frac{\partial \underline{B}_{h,bulk}^T}{\partial a} = \begin{bmatrix} \frac{\partial^2 \psi}{\partial n \partial a} & \frac{\partial^2 \psi}{\partial s \partial a} \end{bmatrix}, \tag{2.38a}$$

$$\frac{\partial \underline{B}_{a,bulk}^T}{\partial a} = \begin{bmatrix} \frac{\partial^3 \psi}{\partial n \partial a^2} & \frac{\partial^3 \psi}{\partial s \partial a^2} \end{bmatrix} h. \tag{2.38b}$$

CHAPTER THREE

A mixed-mode self-adaptive cohesive zone model¹

Abstract

Oscillations observed in the load-displacement response of brittle interfaces modeled by cohesive zone elements in a quasi-static finite element framework are artifacts of the discretization. The typical limit points in this oscillatory path can be traced by application of path-following techniques, or avoided altogether by adequately refining the mesh until the standard iterative Newton-Raphson method becomes applicable. Both strategies however lead to an unacceptably high computational cost and a low efficiency, justifying the development of a process driven hierarchical extension of the discretization used in the process zone of a cohesive crack. A self-adaptive enrichment scheme within individual cohesive zone elements driven by the physics governing the problem, is an efficient solution that does not require further mesh refinements. A two-dimensional mixed-mode example in a general framework with an irreversible cohesive zone law shows that an enriched formulation restores the smoothness of the solution in structures that are discretized in a relatively coarse manner.

¹Reproduced from: M. Samimi, J.A.W. van Dommelen, and M.G.D Geers. A self-adaptive finite element approach for simulation of mixed-mode delamination using cohesive zone models. *Engng. Fract. Mech.* Accepted.

3.1 Introduction

Accumulation of damage at interfaces in laminated structures results in the formation and growth of interlaminar cracks through a non-linear and irreversible process which is known as delamination and constitutes one of the most common failure modes in such structures. Interfacial stresses orthogonal or parallel to laminae cause delamination in mode I (normal opening) or modes II (sliding) and III (tearing), respectively. Continuum models with strong discontinuities seem to yield the best description for deformation of a structure undergoing this failure mechanism.

Linear elastic fracture mechanics (LEFM)-based techniques have often been adopted for the modeling of discrete crack propagation problems when the size of the failure process zone is small compared to structural dimensions which is the case in large structures or brittle interfaces [11, 56, 61, 101, 105, 114]. In this class of methods, the mesh has to be sufficiently fine near the crack tip to capture the stress singularity in that region [47, 132]. Using the partition of unity property of finite elements [8], the extended finite element method (X-FEM) has been introduced to eliminate the need for a mesh refinement by enriching the elements adjacent to the crack with a discontinuous function or near-tip asymptotic functions [13, 84]. The concept has also been extended to cohesive crack propagation analyses [83, 100]. However, additional criteria are still required for crack initiation and propagation [3, 140].

Eliminating the stress singularity at the crack tip, cohesive zone models (CZMs) were introduced by Barenblatt [10] for perfectly brittle materials and by Dugdale [40] for a perfectly plastic material. These models were extensively used after being applied in a finite element framework to predict crack initiation and growth [58]. Later, an interfacial potential was defined to apply the methodology to interface problems [85]. Thereafter, these models have been improved and used in a wide variety of applications [6, 20, 25, 73, 91, 113, 125, 130, 133, 135, 139] while their different numerical aspects have also been investigated [4, 24, 36, 42, 113].

Simulation of interfacial delamination in a finite element framework is carried out by placing interface (decohesion) elements along interfaces between laminae where the interfacial damage in the structure is reflected. The damage free continuum can then be described with an arbitrary material law. Being characterized by a traction-separation law (TSL) which describes the variation of traction with respect to separation along the cohesive zone, interface models have the appealing feature of combining stress-based and fracture mechanics-based approaches to predict delamination onset and propagation [30].

Using CZMs for the modeling of delamination in brittle interfaces in a quasi-static finite element framework suffers from an intrinsic discretization sensitivity. A large number of interface elements are needed for the discretization of the process zone, i.e. the region entering the softening regime [55, 122]. Without this very fine discretization, sudden release of energy in large CZ elements results in a sequence of snap-through or snap-back points to appear in the global load-displacement response of the system [22]). Further mesh refinement may still be necessary to ensure a stable

crack growth in case of physically stable crack growth problems [44].

Application of the standard iterative Newton-Raphson method under load or displacement control fails to converge in the case of snap-through or snap-back. Path-following techniques have been proposed to follow the discretization-induced oscillations, requiring expensive computations accompanying the small increments needed to trace this non-physical path [4, 27, 34, 45, 46, 53, 57, 102, 110]. Since these oscillations are artifacts of the discretization, a persistent mesh refinement finally results in a smooth path which can be solved by the standard Newton-Raphson scheme [82]. However, for realistic interface parameters with a small process zone size, the element size has to be extremely small, which results in unacceptably high computational costs. In some cases, a coarse mesh is used by artificially reducing the interface strength without changing the fracture toughness [124], which can underestimate the loading capacity of the structure [16].

The efficiency and robustness of brittle CZMs can be significantly increased by reducing the oscillations observed in the global load-displacement behavior without further mesh refinement. In line with this purpose, a local enrichment of the elements in the vicinity of the softening process zone with hierarchical polynomial shape functions has been proposed in [28]. The partition of unity property of finite element interpolation functions has been employed to enrich the basis functions of CZ and bulk elements with the analytical solutions of a beam bending problem [52].

Recently, the authors proposed an approach to enrich the separation approximation in the process zone of a cohesive crack by an adaptive hierarchical extension [109]. The linear separation approximation throughout the CZ element was enriched with a bi-linear function, where the enrichment peak position and the magnitude of the enrichment were regarded as additional degrees of freedom. The effect of the enrichment on the global load-displacement response of a simple mode I delamination problem discretized by a relatively coarse mesh was found to be a reduction of the discretization-induced oscillations. However, the adaptivity of the enrichment peak was not optimal; moreover, defining the enrichment peak position in terms of an auxiliary parameter lowered the convergence rate due to introduction of an extra nonlinearity.

In this chapter, the formulation of the process driven enrichment scheme proposed in [109] is extended to account for mixed-mode delamination while taking the irreversibility of the delamination process into account. The formulation of enriched CZ elements and their adjacent bulk elements – that are also enriched for continuity of the displacement field – are derived in a full two-dimensional finite element framework. All numerical aspects of the enrichment are discussed first on the basis of a simple mode I delamination problem which results in a considerable improvement of the enrichment adaptivity. Benefiting from the new developments, the enrichment function acts in a self-adaptive manner within the interface; that is, its peak position is controlled by the moving process zone. To achieve the latter, the penalty formulation used in [109] has been modified to improve the adaptivity of the enrichment in the elements within the process zone. This ensures a maximum benefit to be gained

from the enrichment adaptivity regarding the elimination of discretization-induced oscillations. An additional penalty condition near the boundaries of enriched CZ elements is introduced to keep the bi-linear enrichment function confined within element boundaries. This eliminates the need for a transformation to an auxiliary parameter as done in [109] and prevents convergence problems due to the non-linearity added to the system. The new set of developments significantly improves the efficiency and robustness of an enriched CZM while allowing it to be used in general applications. The advantage of the self-adaptive enrichment is illustrated through a full two-dimensional peel-off example using a mixed-mode irreversible bi-linear traction-separation law.

3.2 Interface model

The most important parameters of an interface constitutive law are the area under the traction-separation curve (known as the fracture toughness) and the maximum strength. However, different shapes have been adopted to describe the variation of traction with respect to separation (or TSL) for which an overview can be found in [24, 127]. In this work, a bi-linear TSL is used.

At an interfacial point between two materials in a two-dimensional continuum, separation and traction vectors are defined as $\boldsymbol{\delta}$ and \mathbf{t} , respectively:

$$\boldsymbol{\delta} = \delta_n \mathbf{n} + \delta_s \mathbf{s}, \quad (3.1a)$$

$$\mathbf{t} = t_n \mathbf{n} + t_s \mathbf{s}, \quad (3.1b)$$

where the direction perpendicular to the interface is denoted by the unit normal vector \mathbf{n} and the vectorial components in that direction are indicated by the subscript n . The vectorial components in the tangential or shear direction, denoted by the unit vector \mathbf{s} , are indicated by the subscript s .

In most two-dimensional engineering applications, fracture energy is dissipated in both normal opening (mode I) and sliding (mode II) during a mixed-mode delamination process. The formulation of a mixed-mode cohesive law can be simplified by introducing an effective separation, λ , as [91, 130]:

$$\lambda = \sqrt{\langle \delta_n \rangle^2 + \beta^2 \delta_s^2}, \quad (3.2)$$

where the weights of tangential and normal opening displacements are determined by the parameter $\beta = t_{s0}/t_{n0}$ in which t_{s0} and t_{n0} denote maximum shear and normal tractions, respectively. Equation (3.2) implies that the interpenetration of laminae does not contribute to the effective separation due to the McCauley brackets, $\langle \delta_n \rangle = (\delta_n + |\delta_n|)/2$. The interface traction-separation law is derived in a damage mechanics

framework as:

$$t = k_0 (1 - d) \lambda, \quad (3.3)$$

where t is the effective traction and k_0 is the slope of the hardening part of the $t - \lambda$ curve as can be seen in Figure 3.1(a). The irreversibility of the interface constitutive model is taken into account by means of the damage parameter, d , for which the evolution law is formulated as [3]:

$$d = \begin{cases} 0 & \text{if } \lambda_{max} < \lambda_0 \\ \frac{\lambda_f}{\lambda_f - \lambda_0} \frac{\lambda_{max} - \lambda_0}{\lambda_{max}} & \text{if } \lambda_0 \leq \lambda_{max} \leq \lambda_f \\ 1 & \text{if } \lambda_{max} > \lambda_f. \end{cases} \quad (3.4)$$

As can be seen in Figure 3.1(a), the effective traction t increases with increasing effective separation λ with an undamaged slope of k_0 until it reaches the interface strength t_0 at a characteristic separation λ_0 . More separation results in a decrease of the interface stiffness which is controlled by the monotonic increase of the damage parameter from 0 for the undamaged case to 1 for the fully damaged case at the failure separation of λ_f as depicted in Figure 3.1(b). The history parameter λ_{max} is set to be the maximum effective separation that has been attained so far.

The expressions for the normal traction, t_n , and the shear traction, t_s , are written as follows:

$$t_n = k_0 (1 - d) \langle \delta_n \rangle - k_0 \langle -\delta_n \rangle, \quad (3.5a)$$

$$t_s = k_0 (1 - d) \beta^2 \delta_s, \quad (3.5b)$$

where a linear elastic response with the initial stiffness is considered in the normal compression regime. The corresponding effective traction is then given by:

$$t = \sqrt{t_n^2 + \beta^{-2} t_s^2}. \quad (3.6)$$

The fracture toughness (also called the critical energy release rate, G_c) is frequently used as a material parameter in a CZM. It equals the area under the effective traction-separation curve. This area denotes the total energy dissipated at the end of the damage process due to delamination and is here given by:

$$G_c = \int_0^{\lambda_f} t \, d\lambda = \frac{1}{2} t_0 \lambda_f, \quad (3.7)$$

and is independent of mode mixity.

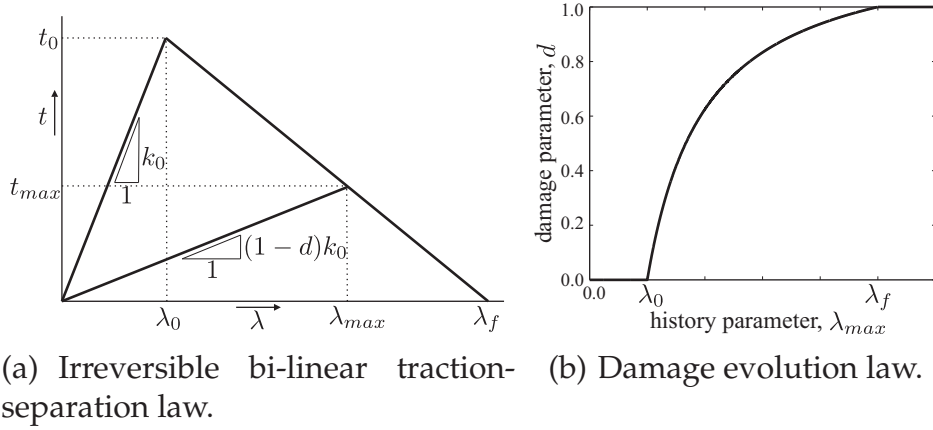


Figure 3.1: Interface constitutive model.

3.3 Cohesive zone enrichment

As delamination grows in brittle interfaces discretized with a coarse mesh, a characteristic non-smooth behavior is observed in the global load-displacement response of the system. To remedy this problem, the finite element formulation of the interface is enriched. The finite element formulation of the neighboring bulk is also enriched to ensure compatibility of the displacement field in the process zone of a cohesive crack which propagates in mixed-mode loading conditions.

3.3.1 Interface elements

Linear 4-node CZ elements as depicted in Figure 3.2(a), are used to discretize the interface between bulk elements. Assuming a geometrically linear framework, a local reference system, $\{\mathbf{n}, \mathbf{s}\}$, is defined with the shear or tangential direction, \mathbf{s} , oriented along the element from the left to the right edge, and the normal direction \mathbf{n} perpendicular to the shear direction. In the undeformed state, the effective separation λ is zero throughout the CZ element; therefore, the element is a line in its initial configuration (line AB in Figure 3.2). The constitutive behavior of the interface has been defined in Section 3.2.

The separation within an enriched CZ element as depicted in Figure 3.2(b), is approximated by linear interpolation functions at the left and right corner nodes of the CZ element, N_L and N_R respectively, and a piecewise linear function ϕ (see Figure 3.3):

$$N_L = 1 - \xi, \quad (3.8a)$$

$$N_R = \xi, \quad (3.8b)$$

$$\phi = \frac{1}{a}\xi - \frac{1}{a(1-a)}\langle \xi - a \rangle. \quad (3.8c)$$

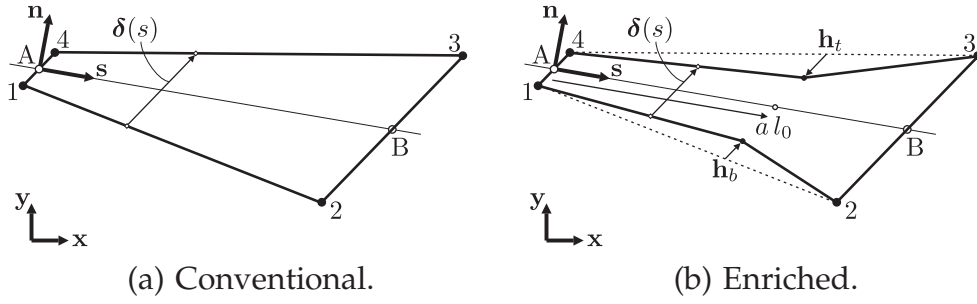


Figure 3.2: A CZ element in an undeformed and deformed state under mixed-mode delamination (line AB shows the undeformed state of the element).

The dimensionless position of the enrichment peak inside the CZ element is denoted by a which is an additional degree of freedom. The above interpolation functions for a CZ element with an initial length of l_0 are expressed in non-dimensional coordinate $\xi \in [0, 1]$ as:

$$\xi = \frac{s}{l_0} \quad \text{with} \quad s \in [0, l_0], \quad (3.9)$$

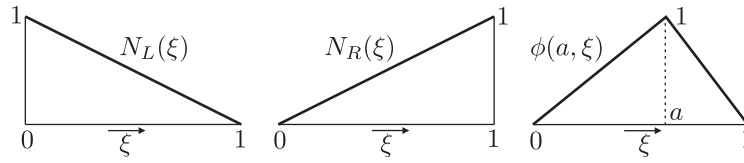


Figure 3.3: Finite element interpolation functions for the 4-node enriched CZ element.

Considering the set of interpolation functions shown in Figure 3.3, the displacements at the top and bottom edges of the enriched CZ element, $\underline{u}_t = [u_{t,n} \ u_{t,s}]^T$ and $\underline{u}_b = [u_{b,n} \ u_{b,s}]^T$ are approximated by:

$$\underline{u}_t = N_L \underline{u}_4 + N_R \underline{u}_3 + \phi \underline{h}_t, \quad (3.10a)$$

$$\underline{u}_b = N_L \underline{u}_1 + N_R \underline{u}_2 + \phi \underline{h}_b, \quad (3.10b)$$

respectively, where \underline{h}_t and \underline{h}_b contain the extra unknown enrichment scaling factors in the normal and shear direction for the top and bottom edges of the interface element, respectively. The field variable of interest is the separation throughout the enriched interface element:

$$\underline{\delta} = \underline{u}_t - \underline{u}_b = \underline{B}_{u,cz} \underline{u}_e + \underline{B}_{h,cz} \underline{h}, \quad (3.11)$$

for which further details are given in Section 3.7.

The tangential stiffness matrix for the enriched CZ element is derived based on the

virtual work principle which reads:

$$\int_{\Gamma} d\delta^T \underline{t} d\Gamma = \int_{\Gamma_b} d\underline{u}_b^T \underline{\bar{t}}_b d\Gamma_b + \int_{\Gamma_t} d\underline{u}_t^T \underline{\bar{t}}_t d\Gamma_t, \quad (3.12)$$

where Γ denotes the internal CZ domain and $d\underline{u}_b$ and $d\underline{u}_t$ represent the displacement perturbations at the external bottom and top edges, Γ_b and Γ_t , respectively. $\underline{\bar{t}}_b$ and $\underline{\bar{t}}_t$ represent the external tractions at the bottom and top edges of the CZ element, respectively. The separation perturbation $d\delta$ is derived as follows:

$$d\delta = \frac{\partial \delta}{\partial \underline{u}_e} d\underline{u}_e + \frac{\partial \delta}{\partial \underline{h}} d\underline{h} + \frac{\partial \delta}{\partial \phi} \frac{\partial \phi}{\partial a} da = \underline{B}_{u,cz} d\underline{u}_e + \underline{B}_{h,cz} d\underline{h} + \underline{B}_{a,cz} da, \quad (3.13)$$

where:

$$\underline{B}_{a,cz}(\xi, a, \underline{h}) = \frac{\partial \delta}{\partial \phi} \frac{\partial \phi}{\partial a} = \frac{\partial \underline{B}_{h,cz}}{\partial \phi} \frac{\partial \phi}{\partial a} \underline{h}. \quad (3.14)$$

Combining Equations (3.12) and (3.13) results in the following equilibrium equation:

$$d\underline{u}_e^T \underline{f}_{i,cz} + d\underline{h}^T \underline{g}_{i,cz} + da b_{i,cz} = d\underline{u}_e^T \underline{f}_{e,cz} + d\underline{h}^T \underline{g}_{e,cz} + da b_{e,cz}. \quad (3.15)$$

In the above expression, $\underline{f}_{i,cz}$, $\underline{g}_{i,cz}$, and $b_{i,cz}$ collect the internal forces adjoint to nodal displacements \underline{u}_e , enrichment scaling factors \underline{h} , and the enrichment peak position a , respectively. External forces are collected in $\underline{f}_{e,cz}$, $\underline{g}_{e,cz}$, and $b_{e,cz}$. The internal forces are defined as:

$$\underline{f}_{i,cz} = \int_{\Gamma} \underline{B}_{u,cz}^T \underline{t} d\Gamma, \quad (3.16a)$$

$$\underline{g}_{i,cz} = \int_{\Gamma} \underline{B}_{h,cz}^T \underline{t} d\Gamma, \quad (3.16b)$$

$$b_{i,cz} = \int_{\Gamma} \underline{B}_{a,cz}^T \underline{t} d\Gamma. \quad (3.16c)$$

The derivation of the tangential stiffness matrix is given in Section 3.8. The adaptivity of the enrichment peak position requires special attention for the integration procedure. Integration of the element can be done by either using fixed integration points (in which case a sufficiently high number is needed) or by a lower number of adaptive integration points. In order to calculate the stiffness matrix and internal force components, a Gaussian integration scheme using fixed integration points is adopted which is more efficient for the storage of history parameters in the case of an enriched CZ element. A relatively large number of integration points (i.e. 10) are used because of the highly non-linear nature of the traction-separation law combined with the enriched kinematics. The numerical integration of CZ elements on the basis of a Gaussian integration scheme may result in spurious oscillations of the traction field. A low order Newton-Cotes integration scheme gives the smoothest

results when high traction gradients exist throughout the interface element [113]. However, a Newton-Cotes integration scheme yields no improvement with respect to the element performance when a high order integration, which is necessary here, is applied [113]. Moreover, the oscillations observed in the global structural load-displacement response are discretization-induced ones which are not affected by the integration scheme. Therefore, a convenient choice of using the same integration scheme (Gaussian) is made for both enriched interface and bulk elements (see Section 3.3.2 for the latter). Since the CZ element is formulated in element coordinates $\{n, s\}$, a coordinate transformation is carried out to convert all vectorial field variables to a global coordinate system $\{x, y\}$.

3.3.2 Bulk elements

The two-dimensional bulk medium is discretized by geometrically linear 4-node quadrilateral elements as shown in Figure 3.4(a). For the bulk elements connected to CZ elements, field variables are described in a local coordinate system with basis $\{n, s\}$ which is aligned with the CZ element coordinates (see Figure 3.4).

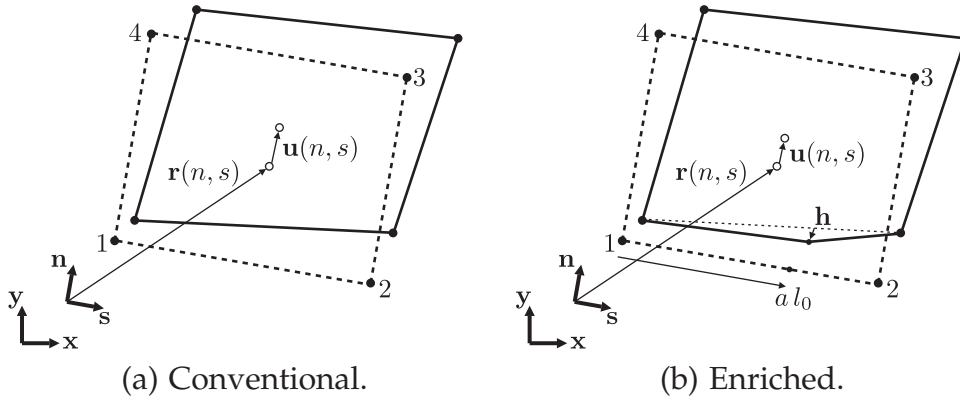


Figure 3.4: A 2-D bulk element in an undeformed and deformed state.

The bulk elements adjacent to the enriched CZ elements are enriched as depicted in Figure 3.4(b) to ensure the continuity of the displacement field in the crack front region. The displacement field of the enriched elements is enhanced by a weighted piecewise linear enrichment function, ψ :

$$u = \underline{N} u_e + \psi h, \quad (3.17)$$

with

$$\psi = (1 - \eta) \phi. \quad (3.18)$$

All interpolation functions including standard element shape functions $\underline{N}(\xi, \eta)$ and

the bi-linear enrichment function $\phi(a, \xi)$ are expressed in terms of the isoparametric coordinates $\xi, \eta \in [0, 1]$, with ξ along the direction of the interface element connected to the bulk element in its initial configuration. Before the global assembly of the system, a coordinate transformation is carried out to convert all vectorial field variables to a global coordinate system $\{\mathbf{x}, \mathbf{y}\}$.

The strain field in the bulk material is then given by:

$$\underline{\epsilon} = \underline{B}_{u,bulk} \underline{u}_e + \underline{B}_{h,bulk} \underline{h}, \quad (3.19)$$

for which further details are given in Section 3.7.

The constitutive behavior of the bulk material in a small strain/displacement framework is defined as:

$$\underline{\sigma} = \mathcal{G}(\underline{\epsilon}). \quad (3.20)$$

Ignoring body forces acting on the medium, the virtual work principle is written as:

$$\int_{\Omega} \underline{d}\underline{\epsilon}^T \underline{\sigma} \, d\Omega = \int_{\Gamma} \underline{d}\underline{u}^T \bar{\underline{t}} \, d\Gamma, \quad (3.21)$$

where $\underline{d}\underline{\epsilon}$ represents a small strain perturbation. Γ and Ω represent the circumferential boundary and the domain of the bulk element, respectively. The external forces are denoted by $\bar{\underline{t}}$. The strain perturbation can then be expressed as:

$$\underline{d}\underline{\epsilon} = \frac{\partial \underline{\epsilon}}{\partial \underline{u}_e} \underline{d}\underline{u}_e + \frac{\partial \underline{\epsilon}}{\partial \underline{h}} \underline{d}\underline{h} + \frac{\partial \underline{\epsilon}}{\partial a} \frac{\partial \psi}{\partial a} \underline{d}a = \underline{B}_{u,bulk} \underline{d}\underline{u}_e + \underline{B}_{h,bulk} \underline{d}\underline{h} + \underline{B}_{a,bulk} \underline{d}a, \quad (3.22)$$

where:

$$\underline{B}_{a,bulk}(\xi, \eta, a, \underline{h}) = \frac{\partial \underline{B}_{h,bulk}}{\partial a} \underline{h}. \quad (3.23)$$

Combining Equations (3.21) and (3.22) results in the following equilibrium equation:

$$\underline{d}\underline{u}_e^T \underline{f}_{i,bulk} + \underline{d}\underline{h}^T \underline{g}_{i,bulk} + \underline{d}a \, b_{i,bulk} = \underline{d}\underline{u}_e^T \underline{f}_{e,bulk} + \underline{d}\underline{h}^T \underline{g}_{e,bulk} + \underline{d}a \, b_{e,bulk}, \quad (3.24)$$

In the above expression, $\underline{f}_{i,bulk}$, $\underline{g}_{i,bulk}$, and $b_{i,bulk}$ collect the internal forces adjoint to the nodal displacements \underline{u}_e , enrichment scaling factors \underline{h} , and the enrichment peak position a , respectively. External forces are collected by $\underline{f}_{e,bulk}$, $\underline{g}_{e,bulk}$, and $b_{e,bulk}$. The internal forces are defined as:

$$\underline{f}_{i,bulk} = \int_{\Omega} \underline{B}_{u,bulk}^T \underline{\sigma} \, d\Omega, \quad (3.25a)$$

$$\underline{g}_{i,bulk} = \int_{\Omega} \underline{B}_{h,bulk}^T \underline{\sigma} \, d\Omega, \quad (3.25b)$$

$$b_{i,bulk} = \int_{\Omega} \underline{B}_{a,bulk}^T \varrho \, d\Omega. \quad (3.25c)$$

The derivation of the tangential stiffness matrix is given in Section 3.8. In order to calculate the stiffness matrix and internal force components, a Gauss numerical integration scheme is adopted. Since there is no history parameter in linear elastic bulk elements to keep track of, it is not required to use a high number of fixed integration points in an enriched element. Instead, the integration is carried out in both parts of the element separated by the enrichment peak with as few integration points as required (i.e. 2×2 integration points in each part) [109].

3.4 Numerical aspects of the enrichment

A simplified peel-off test, for which an analytical solution exists [109], is revisited to illustrate important numerical aspects of the enrichment which leads to a deeper insight in its efficiency. The adaptivity of the proposed enrichment and the penalty formulation used to ensure a unique solution are discussed in detail.

A linear elastic bulk material is pulled from a rigid substrate as shown in Figure 3.5. A bi-linear TSL as introduced in Section 3.2 and characterized by $G_c = 0.25 \text{ N/mm}$, $t_0 = 100 \text{ MPa}$, $\lambda_0 = 1.0 \text{ }\mu\text{m}$, and without shear tractions ($\beta = 0$) is used in the interface. The bulk material is characterized by a stiffness of $C_{nn} = 45 \text{ GPa}$ in normal direction and zero stiffness for the other components of the elasticity matrix; therefore, all displacements and/or separations occur in the normal direction. A normal displacement is incrementally prescribed, distributed linearly along the upper edge of the bulk layer where the final prescribed displacement of the left and right top edge of the bulk layer are given by $u_{n,L} = 12 \text{ }\mu\text{m}$ and $u_{n,R} = 4 \text{ }\mu\text{m}$, respectively.

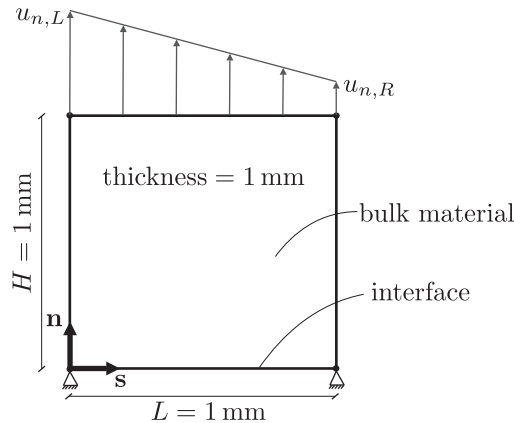


Figure 3.5: Simplified mode I delamination problem; geometry and boundary conditions.

The traction-separation law considered here is assumed to be reversible so that the

total work done in the interface before complete failure remains recoverable. Therefore, a total potential energy concept applies to this simplified example which facilitates a comprehensive study of the variation of the total potential with respect to the enrichment peak position. However, the arguments based on the reversible law do apply when unloading does not occur within the process zone even if the assumed constitutive law is irreversible. For this reason, the principles that are derived in this section apply to the general numerical example of the next section and to other cases when unloading does not occur anywhere within the process zone without affecting the validity of the analysis.

In line with this purpose and in contrast to [109], only one enriched or one non-enriched bulk/CZ element is used to discretize the domain. Although the enrichment peak position and scaling factors are driven by the deformation process, i.e. their values are determined during an incremental/iterative approach, the behavior of the system is first analyzed for a suitably high and well-spaced number of enrichment peak positions to investigate the variation of the total potential, Π , with respect to the new degree of freedom where the upper edge linear displacement is prescribed incrementally ($u_{n,L} \in [0, 12 \mu\text{m}]$). In this variational context, the solution minimizes the total potential of the system, which here consists of the strain energy stored in the bulk layer and the internal work done in the interface. Figure 3.6 shows the optimum enrichment peak position a , throughout the delamination process obtained by direct minimization of the total potential.

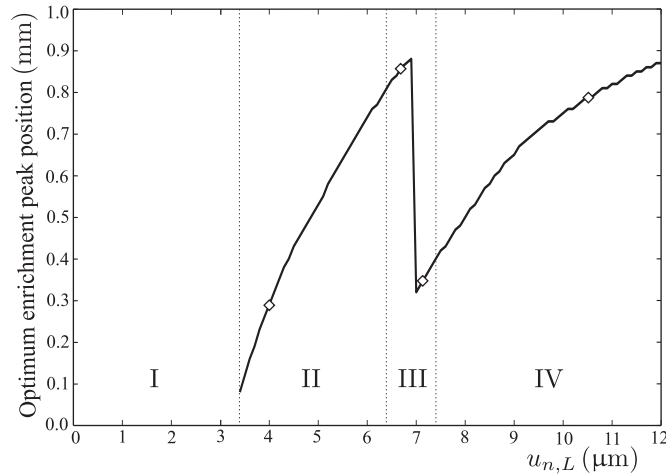


Figure 3.6: Optimum position of the enrichment peak throughout the deformation process (symbols \diamond indicate the positions for which the total potential variations, opening profile, and traction profile are shown in Figure 3.7).

Different separation regimes are identified, during which delamination progresses through the interface (see Figure 3.6). Initially, the whole interface remains intact ($\lambda < \lambda_c$), which results in a linear separation and traction profile along the entire interface and no variation of the total potential with respect to the enrichment peak po-

sition (see Figure 3.7(a)). Later, in regime II, the interface starts to soften from the left edge while the right part is still intact. For the bi-linear separation profile depicted in Figure 3.7(b), the total potential is minimized when the enrichment peak position is at the kink point in the analytical separation profile. The analytical traction profile along the interface is captured exactly with the bi-linear enrichment, whereas the non-enriched solution is not a good approximation. The analytical solution for further delamination growth (regime III) shows a tri-linear separation profile in which the left kink separates the completely failed part (zero cohesive traction) from the softening part and the right kink separates the softening part from the intact part of the interface. In this regime, it is obvious that the analytical profile cannot be captured exactly with a bi-linear enrichment. As can be seen in Figures 3.7(c) and 3.7(d), the total potential (as a function of the enrichment peak position) in this separation regime is non-convex, with two local minima. The minimum related to the right kink point is moving toward the right edge, whereas the second minimum (related to the left kink point) enters from the left edge. Even though still more efficient than the non-enriched solution, the enriched solution now only approximates the tri-linear analytical traction profile. For the last delamination stage (IV) before complete interface failure, the analytical solution shows again a bi-linear separation profile, where the right part of the interface is still softening (see Figure 3.7(e)). The total potential (expressed with respect to the enrichment peak position) has again one minimum that coincides with the analytical separation profile kink point. The analytical traction profile along the interface is again captured exactly with the bi-linear numerical solution, while the non-enriched solution falls short.

Some important numerical aspects of the implementation of the enrichment, especially related to the case where both or none of the TSL characteristic kink points are present in a single CZ element or a transition between different separation regimes occurs, are to be discussed. Special attention is also paid to keeping the enrichment peak position inside the element boundaries.

In case of a linear separation profile in the analytical solution (Figure 3.7(a)), no optimal enrichment peak position exists (regime I in Figure 3.6), i.e. the enrichment is not needed. In such a case, parameter a does not have any real meaning and a singular matrix is obtained in practice. In order to ensure a unique solution in this case, a penalty term, \mathcal{P}_1 , based on the enrichment peak position, a , is added to the total potential (see Figure 3.8) defined as:

$$\mathcal{P}_1 = c_1 (a - \bar{a})^2, \quad (3.26)$$

where c_1 is a sufficiently small penalty factor that does not significantly influence the solution if the enrichment is active in the CZ element. The value of \bar{a} is incrementally adapted in order to keep the influence of the penalty small throughout the deformation process:

$$\bar{a}_n = a_{n-1}^{(c)}, \quad (3.27)$$

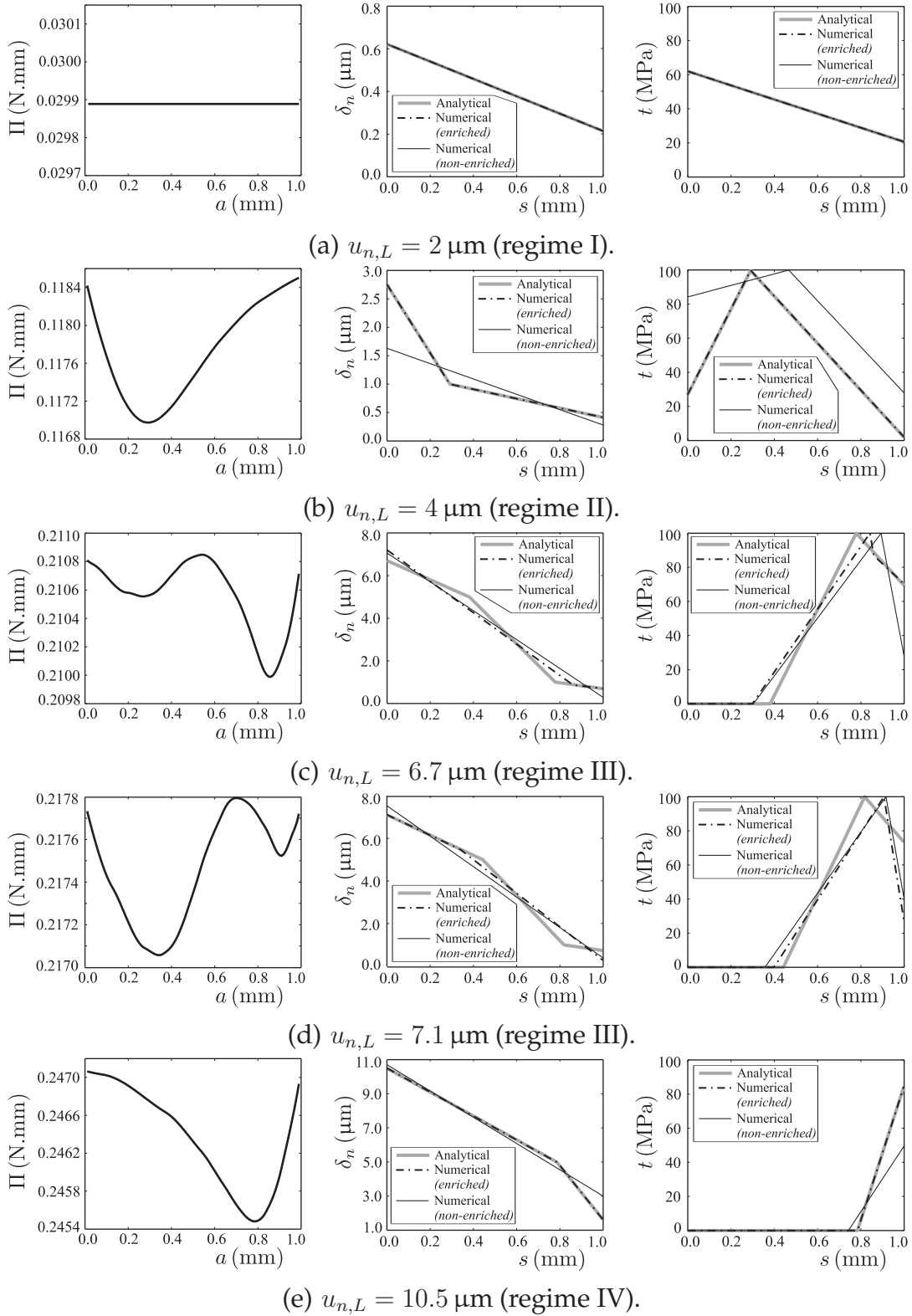


Figure 3.7: Total potential expressed with respect to the enrichment peak position (left), opening profile in the analytical and the numerical solution (middle), and traction profile in the analytical and the numerical solutions (right) in different stages of delamination growth.

where $a_{n-1}^{(c)}$ is the last converged value for the enrichment peak position within an incremental procedure. In addition, the initial estimate for a_n in a Newton-Raphson solution procedure for increment n is set equal to \bar{a}_n . The initial position of \bar{a} is chosen close to the left or right edge of the enriched interface element depending on from which side delamination enters the element. Note that it is not always known a priori but can usually be obtained from the opening profile in the early stages of loading. To increase the efficiency, an adaptive enrichment strategy is used where only elements near the process zone are enriched (see [109]).

A tri-linear separation profile within a single interface element can not be captured with the bi-linear profile of the numerical approximation. Consequently, as can be seen in Figures 3.7(c) and 3.7(d), the potential of the system with respect to the enrichment peak position is non-convex, with two local minima. In order to capture the second kink point entering the element, \bar{a} and the initial estimate for a are discretely shifted to the vicinity of the other edge ($\bar{a} = 0.1$) when the first enrichment peak position is approaching the right edge of the interface element. Increasing the penalty coefficient and fixing \bar{a} to an arbitrary position, i.e. in the middle of the element, is another possible solution for the case where both characteristic kink points of the TSL are contained within a single interface element. The proposed solution on the basis of Equation (3.26), takes benefit of the local convergence radius of the Newton-Raphson method and the local convex character of each minimum in Π .

The enrichment function becomes singular when the enrichment peak approaches the interface element boundaries ($a = 0$ or $a = 1$). In [109], a transformation to an auxiliary parameter z as the degree of freedom (instead of the enrichment peak position a) has been proposed to handle this problem. In doing so, a was defined as an arctan function of the auxiliary parameter, which automatically enforces the constraint $a \in (0, 1)$. However, in that approach, the non-linear dependence of the actual solution on the auxiliary degree of freedom varies considerably throughout the domain, which slows down the convergence rate. Application of the auxiliary parameter limits the enrichment adaptivity to the vicinity of the center of the element where its relation with the enrichment peak position is almost linear. To remedy this, another penalty \mathcal{P}_2 is used, which becomes large near the boundaries of enriched CZ elements, as shown in Figure 3.8, ensuring that the peak of the bi-linear enrichment function stays within the element boundaries:

$$\mathcal{P}_2 = \begin{cases} c_2 (a - \bar{a}_L)^2 & \text{for } a \leq \bar{a}_L \\ c_2 (a - \bar{a}_R)^2 & \text{for } a \geq \bar{a}_R, \end{cases} \quad (3.28)$$

where \bar{a}_L and \bar{a}_R are fixed positions close to the left and right edges of the enriched interface element, i.e. $\bar{a}_L = 0.1$ and $\bar{a}_R = 0.9$, respectively, and c_2 is a sufficiently large penalty factor to keep the enrichment peak position away from the element boundaries. In fact, there is no need to let the enrichment peak position approach the element boundaries because the effect of the enrichment becomes negligible then and nodal interpolations suffice for the numerical approximation. In addition to this penalty, for values of the degree of freedom a outside of the domain $[\bar{a}_L, \bar{a}_R]$, the

effective enrichment peak position used in Equation (3.8c) is kept at the edge of this domain so that the total potential of the system depends only on the penalty terms \mathcal{P}_1 and \mathcal{P}_2 . The resulting total potential of the system is then defined by:

$$\bar{\Pi} = \Pi + \mathcal{P}_1 + \mathcal{P}_2. \quad (3.29)$$

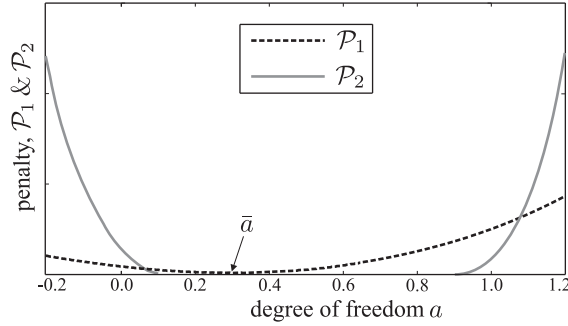


Figure 3.8: Schematic representation of the penalty terms applied to the degree of freedom a .

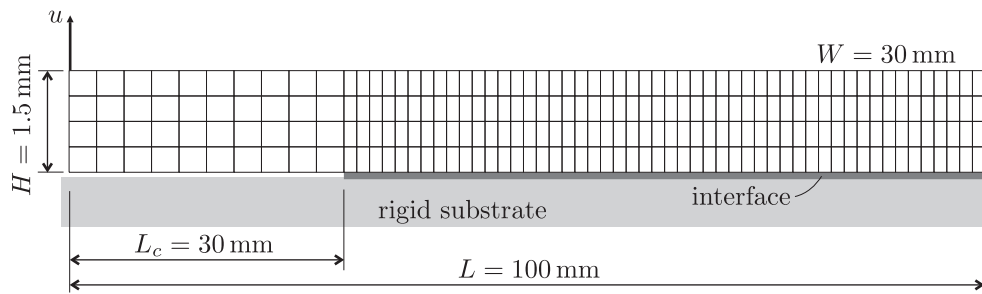
The numerical procedure outlined in this section enables a full adaptivity of the proposed enrichment in the regimes where the enrichment is meaningful (see the numerical solution in Figure 3.7), whereas it stabilizes the solution in other regimes.

In order to enhance the efficiency of the proposed enrichment, an adaptive enrichment strategy can be employed to enrich only the elements located in the process zone. At the end of each increment, the effective separation throughout CZ elements is monitored and a suitable choice is made on the elements to be enriched. The strategy is fully described in [109] for the normal opening only.

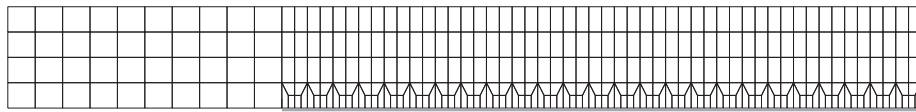
3.5 Mixed-mode application

In order to evaluate the performance of the improved enriched CZM in a mixed-mode delamination problem, a full 2-D peel-off test under plane strain conditions is considered. In this example, a linear elastic bulk strip with length L , height H , and width W is pulled from a rigid substrate, see Figure 3.9(a). In the interface between the strip and the substrate, an initial crack with length L_c is inserted. A normal displacement up to $u = 3$ mm is prescribed at the pre-cracked end of the strip.

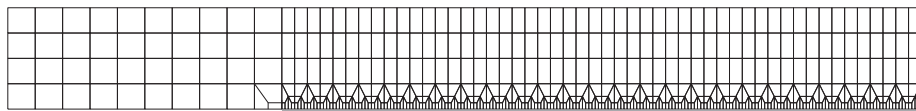
The bulk layer is discretized by a regular mesh of 4×10 elements along the cracked length and a finer regular mesh of 4×50 elements along the rest of the strip. The interface is initially discretized by 50 CZ elements characterized by the bi-linear TSL introduced in Section 3.2. Also more refined interface discretizations are used. The 4-node linear elements suffer from an intrinsic inefficiency in describing the bending



(a) Geometry, boundary conditions, discretization; 50 CZ elements along the interface.



(b) Discretization; 100 CZ elements along the interface.



(c) Discretization; 200 CZ elements along the interface.

Figure 3.9: Mixed-mode delamination problem; geometry, boundary conditions, and mesh refinement schemes.

behavior. However, the main focus here is on the discretization at the level of the interface and examining the performance of the proposed enrichment. In order to eliminate the effect of the bending approximation in the comparison of interface discretizations, only the bulk element layer adjacent to the interface is refined by factors of 2 and 4 (see Figures 3.9(b) and 3.9(c), respectively).

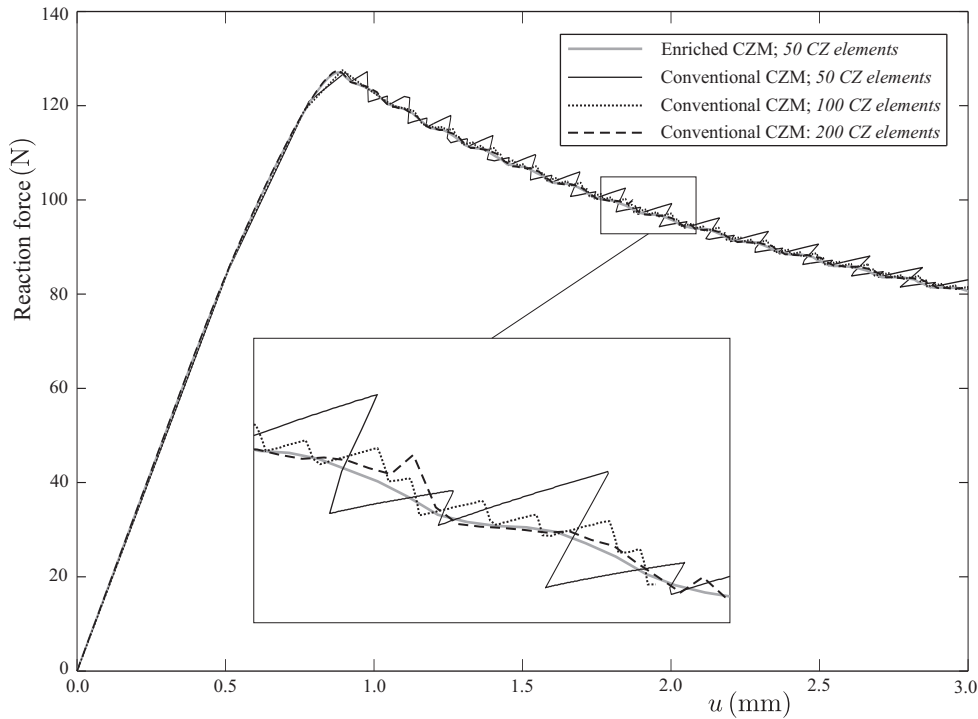
Bulk material data and CZM parameters are given in Table 3.1. The small characteristic separation, λ_0 , relative to the structural dimensions implies a relatively brittle interface. For these bulk material properties and CZM parameters, the mesh with 50 interface elements is relatively coarse and therefore the global load-displacement response of the system shows severe oscillations when conventional CZ elements are used, as can be seen in Figure 3.10. In the figure, each oscillation represents the failure of one CZ element.

Since a standard displacement-controlled procedure with an iterative Newton-Raphson solution method fails to converge in the case of snap-backs, a path-following technique has to be adopted. In the case of delamination analysis in brittle interfaces, the problem is governed by a strong deformation localization for which local arc-length control methods are well suited. Here, a weighted sub-plane control (see [45, 46]) on the rate of opening in the interface with the cylindrical arc-length method, as introduced in [27], is used to follow the oscillatory path.

Table 3.1: Bulk material data and CZM parameters.

Young's modulus, E (GPa)	100
Poisson's ratio, ν	0.3
Fracture toughness, G_c (N/mm)	0.25
Interface strength, t_0 (MPa)	20
Characteristic separation, λ_0 (mm)	0.005
Maximum traction ratio, β	1.0

Table 3.2 shows that a large number of increments/iterations are needed to track the non-physical oscillations resulting from a coarse discretization of the brittle interface. Also, the robustness of conventional CZMs is limited. Consequently, achieving convergence can not be guaranteed in the case of very sharp snap-backs even at the cost of extremely small increment steps.

**Figure 3.10:** Force-displacement responses of the mixed-mode peel-off problem.

As can be seen in Figure 3.10, using more CZ elements smoothens the global response of the unenriched model. However, as can be seen in Table 3.2, a standard Newton-Raphson method still fails to converge at $u = 1.72$ mm in the case of two times refinement and application of the path-following approach becomes necessary for a full simulation. A more refined mesh using 200 CZ elements at the interface smoothens the global response so that a standard Newton-Raphson method can be used for the simulation of the mixed-mode delamination problem at the cost of a

noticeable increase in the number of degrees of freedom (see Table 3.2).

Table 3.2: Numerical performance of different algorithms.

CZ model	Number of CZ elements	Total number of increments	Total number of iterations	nDOF	u_{max} (mm)
Conventional	50 †	3740	7705	712	3.00
	100 ‡	1425	3059	1062	3.00
	100 †	(119) §	(476) §	1062	1.72
	200 †	203	758	1768	3.00
Enriched	50 †	153	610	757	3.00

† Solved by the standard Newton-Raphson method.

‡ Solved by a local arc-length control method.

§ The final displacement was not reached since the simulation failed prematurely.

Application of the proposed enrichment together with the improvements, especially on the penalty formulation, smoothens the path to a level that can be followed by a standard Newton-Raphson method, even for the most coarse mesh, which significantly increases the efficiency of the CZM. As can be seen in Figure 3.10, some minor oscillations are left in the enriched coarse mesh while the maximum number of degrees of freedom encountered to complete the maximum prescribed displacement is only slightly higher than that of a non-enriched coarse mesh solved by a local path-following technique.

Since a lack of adaptivity implies a local refinement by a factor of only two, a major increase in the enrichment adaptivity due to the current developments constitutes a substantial improvement with respect to the first model published in [109]. In fact, the enriched model behaves in a more smooth and efficient manner compared to refinement remedies while preserving the lowest computational effort by eliminating the need for expensive mesh refinements, and allowing for a standard solution method.

3.6 Discussion and conclusion

Cohesive zone models are commonly used to simulate initiation and propagation of delamination, whereby enough cohesive zone (CZ) elements should be used in the process zone to ensure a correct description of the opening profile which results in a more stable solution. Hence, a fine mesh is necessary for brittle interfaces, where the process zone size is small compared to other structural dimensions. A fine mesh typically increases the computational cost whereas a coarse discretization results in snap-backs in the global load-displacement response of the system (leading to instabilities with a standard iterative Newton-Raphson method). The oscillations

can be followed by using path-following techniques with a high computational cost to trace all non-physical oscillations. Elimination or reduction of these oscillations in the global load-displacement response, with a solution that preserves a coarse discretization scheme, obviously enhances the efficiency and robustness of cohesive zone models.

In this chapter, an adaptive hierarchical extension is used to enrich the separation approximation in the process zone of an interface undergoing a mixed-mode delamination. The interface constitutive law is formulated within a damage mechanics framework which takes the irreversibility of the delamination process into account. The elaborated bi-linear traction-separation law accounts for tractions in both normal and shear directions. A bi-linear function with a mobile enrichment peak is used to enhance the linear separation approximation within a CZ element. The adaptivity of the peak of the enrichment function within individual CZ elements locally improves the discretization according to the physics governing the problem.

The formulation of enriched CZ and bulk elements is derived in a full two-dimensional finite element framework. While being simple to implement, linear 4-node bulk elements do not show a high performance in delamination problems which involve bending. In such cases, kinematically enhanced or higher order elements are more accurate; however, these elements are not used in this work to avoid extra complications and to keep the focus on the role of the enrichment in yielding a more accurate separation approximation in the process zone of a cohesive crack while the proposed enrichment or higher order enrichments of this type can be applied to higher order elements as well which can be useful in a certain class of problems.

Important numerical aspects of the enrichment are discussed on the basis of a simplified mode I delamination problem. The adaptivity of the enrichment and its relation with the total potential of the system have been investigated which results in a considerable improvement of the enrichment adaptivity and leads to a further minimization of the discretization-induced oscillations. A new penalty formulation is used to ensure a unique solution and to keep the enrichment within the element boundaries. The latter eliminates the need for a transformation to an auxiliary parameter as done in [109] and improves the stability of the methodology by preventing extra convergence problems due to the non-linearity that was being added to the non-linear system. It is also shown that a tri-linear separation profile obtained from the analytical solution is not captured exactly and that multiple minima occur in the non-convex total potential of the system. However, a procedure is proposed to handle the non-convex nature and tracing of the minima.

The mode-mixity is taken into account in a peel-off example which is solved in a full two-dimensional finite element framework. It is shown that the proposed enrichment in combination with a coarse mesh significantly enhances the efficiency of the cohesive zone model by smoothening the global load-displacement response of the system while it can be used in general two-dimensional applications. In fact, application of the elaborated enrichment eliminates the need for a further mesh refinement

while keeping the standard Newton-Raphson approach applicable in the case of a relatively coarse mesh which saves considerable computational costs. Extension of the proposed enrichment scheme to delamination in a three-dimensional finite element framework is conceptually possible but not straightforward. It involves the adaptivity of a crack front as a line in a planar interface. This subject is addressed in the following chapter.

3.7 Appendix A: Element formulation

In this appendix, the formulation of Section 3.3 is given in more detail.

3.7.1 Cohesive zone elements

Equation (3.11) for the separation along an interface element can be written as:

$$\underline{\delta} = \begin{bmatrix} \delta_n \\ \delta_s \end{bmatrix} = \underline{B}_{u,cz} \underline{u}_e + \underline{B}_{h,cz} \underline{h}, \quad (3.30)$$

with

$$\underline{B}_{u,cz}(\xi) = \begin{bmatrix} -N_L & 0 & -N_R & 0 & N_R & 0 & N_L & 0 \\ 0 & -N_L & 0 & -N_R & 0 & N_R & 0 & N_L \end{bmatrix}, \quad (3.31a)$$

$$\underline{u}_e = [u_{1,n} \quad u_{1,s} \quad u_{2,n} \quad u_{2,s} \quad u_{3,n} \quad u_{3,s} \quad u_{4,n} \quad u_{4,s}]^T, \quad (3.31b)$$

$$\underline{B}_{h,cz}(\xi, a) = \phi \begin{bmatrix} -1 & 0 & 1 & 0 \\ 0 & -1 & 0 & 1 \end{bmatrix}, \quad (3.31c)$$

$$\underline{h} = [h_{b,n} \quad h_{b,s} \quad h_{t,n} \quad h_{t,s}]^T. \quad (3.31d)$$

3.7.2 Bulk elements

Considering Equations (3.17) and (3.19) for the displacement field and strain in the bulk element, the following can be written:

$$\underline{N} = \begin{bmatrix} N_1 & 0 & N_2 & 0 & N_3 & 0 & N_4 & 0 \\ 0 & N_1 & 0 & N_2 & 0 & N_3 & 0 & N_4 \end{bmatrix}, \quad (3.32a)$$

$$\underline{u}_e = [u_{1,n} \quad u_{1,s} \quad u_{2,n} \quad u_{2,s} \quad u_{3,n} \quad u_{3,s} \quad u_{4,n} \quad u_{4,s}]^T, \quad (3.32b)$$

$$\underline{h} = [h_n \quad h_s]^T, \quad (3.32c)$$

$$\underline{B}_{u,bulk}(\xi, \eta) = \begin{bmatrix} \frac{\partial}{\partial n} & 0 \\ 0 & \frac{\partial}{\partial s} \\ \frac{\partial}{\partial s} & \frac{\partial}{\partial n} \end{bmatrix} \underline{N}, \quad (3.32d)$$

$$\underline{B}_{h,bulk}(\xi, \eta, a) = \begin{bmatrix} \frac{\partial \psi}{\partial n} & 0 \\ 0 & \frac{\partial \psi}{\partial s} \\ \frac{\partial \psi}{\partial s} & \frac{\partial \psi}{\partial n} \end{bmatrix}. \quad (3.32e)$$

The interpolation and enrichment functions are defined by using isoparametric coordinates $\xi, \eta \in [0, 1]$, with ξ along the direction of the interface:

$$N_1 = (1 - \xi)(1 - \eta), \quad (3.33a)$$

$$N_2 = \xi(1 - \eta), \quad (3.33b)$$

$$N_3 = \xi\eta, \quad (3.33c)$$

$$N_4 = (1 - \xi)\eta, \quad (3.33d)$$

$$\psi = (1 - \eta)\phi. \quad (3.33e)$$

It should be noted that these interpolation functions deviate from a standard isoparametric formulation.

3.8 Appendix B: Tangential stiffness matrix

3.8.1 Cohesive zone elements

The tangential stiffness matrix of the CZ element used in the non-linear solution procedure contains the derivatives of the internal forces with respect to the element degrees of freedom:

$$\underline{K}_{cz} = \begin{bmatrix} \underline{K}_{uu,cz} & \underline{K}_{uh,cz} & \underline{K}_{ua,cz} \\ \underline{K}_{hu,cz} & \underline{K}_{hh,cz} & \underline{K}_{ha,cz} \\ \underline{K}_{au,cz} & \underline{K}_{ah,cz} & \underline{K}_{aa,cz} \end{bmatrix}, \quad (3.34a)$$

where:

$$\begin{aligned} \underline{K}_{uu,cz} &= \frac{\partial f_{i,cz}}{\partial \underline{u}} = \int_{\Gamma} \frac{\partial}{\partial \underline{u}} (\underline{B}_{u,cz}^T \underline{t}) \, d\Gamma = \int_{\Gamma} \underline{B}_{u,cz}^T \frac{\partial \underline{t}}{\partial \underline{u}} \, d\Gamma \\ &= \int_{\Gamma} \underline{B}_{u,cz}^T \underline{H}_{cz} \underline{B}_{u,cz} \, d\Gamma, \end{aligned} \quad (3.34b)$$

$$\begin{aligned} \underline{K}_{hu,cz} &= \frac{\partial g_{i,cz}}{\partial \underline{u}} = \int_{\Gamma} \frac{\partial}{\partial \underline{u}} (\underline{B}_{h,cz}^T \underline{t}) \, d\Gamma = \int_{\Gamma} \underline{B}_{h,cz}^T \frac{\partial \underline{t}}{\partial \underline{u}} \, d\Gamma \\ &= \int_{\Gamma} \underline{B}_{h,cz}^T \underline{H}_{cz} \underline{B}_{u,cz} \, d\Gamma, \end{aligned} \quad (3.34c)$$

$$\underline{K}_{uh,cz} = \underline{K}_{hu,cz}^T, \quad (3.34d)$$

$$\begin{aligned} \underline{K}_{au,cz} &= \frac{\partial b_{i,cz}}{\partial u} = \int_{\Gamma} \frac{\partial}{\partial u} (\underline{B}_{a,cz}^T \underline{t}) \, d\Gamma = \int_{\Gamma} \underline{B}_{a,cz}^T \frac{\partial \underline{t}}{\partial u} \, d\Gamma \\ &= \int_{\Gamma} \underline{B}_{a,cz}^T \underline{H}_{cz} \underline{B}_{u,cz} \, d\Gamma, \end{aligned} \quad (3.34e)$$

$$\underline{K}_{ua,cz} = \underline{K}_{au,cz}^T, \quad (3.34f)$$

$$\begin{aligned} \underline{K}_{hh,cz} &= \frac{\partial g_{i,cz}}{\partial h} = \int_{\Gamma} \frac{\partial}{\partial h} (\underline{B}_{h,cz}^T \underline{t}) \, d\Gamma = \int_{\Gamma} \underline{B}_{h,cz}^T \frac{\partial \underline{t}}{\partial h} \, d\Gamma \\ &= \int_{\Gamma} \underline{B}_{h,cz}^T \underline{H}_{cz} \underline{B}_{h,cz} \, d\Gamma, \end{aligned} \quad (3.34g)$$

$$\begin{aligned} \underline{K}_{ah,cz} &= \frac{\partial b_{i,cz}}{\partial h} = \int_{\Gamma} \frac{\partial}{\partial h} (\underline{B}_{a,cz}^T \underline{t}) \, d\Gamma = \int_{\Gamma} \left(\underline{B}_{a,cz}^T \frac{\partial \underline{t}}{\partial h} + \underline{t}^T \frac{\partial \underline{B}_{a,cz}}{\partial h} \right) \, d\Gamma \\ &= \int_{\Gamma} \left(\underline{B}_{a,cz}^T \underline{H}_{cz} \underline{B}_{h,cz} + \underline{t}^T \frac{\partial \underline{B}_{h,cz}}{\partial a} \right) \, d\Gamma, \end{aligned} \quad (3.34h)$$

$$\underline{K}_{ha,cz} = \underline{K}_{ah,cz}^T, \quad (3.34i)$$

$$\begin{aligned} K_{aa,cz} &= \frac{\partial b_{i,cz}}{\partial a} = \int_{\Gamma} \frac{\partial}{\partial a} (\underline{B}_{a,cz}^T \underline{t}) \, d\Gamma = \int_{\Gamma} \left(\underline{B}_{a,cz}^T \frac{\partial \underline{t}}{\partial a} + \underline{t}^T \frac{\partial \underline{B}_{a,cz}}{\partial a} \right) \, d\Gamma \\ &= \int_{\Gamma} \left(\underline{B}_{a,cz}^T \underline{H}_{cz} \underline{B}_{a,cz} + \underline{t}^T \frac{\partial \underline{B}_{a,cz}}{\partial a} \right) \, d\Gamma. \end{aligned} \quad (3.34j)$$

The following derivatives were used in the above formulation:

$$\underline{B}_{a,cz} = \frac{\partial \phi}{\partial a} \begin{bmatrix} -1 & 0 & 1 & 0 \\ 0 & -1 & 0 & 1 \end{bmatrix} \underline{h}, \quad (3.35a)$$

$$\frac{\partial \underline{B}_{h,cz}}{\partial a} = \frac{\partial \phi}{\partial a} \begin{bmatrix} -1 & 0 & 1 & 0 \\ 0 & -1 & 0 & 1 \end{bmatrix}, \quad (3.35b)$$

$$\frac{\partial \underline{B}_{a,cz}}{\partial a} = \frac{\partial^2 \phi}{\partial a^2} \begin{bmatrix} -1 & 0 & 1 & 0 \\ 0 & -1 & 0 & 1 \end{bmatrix} \underline{h}. \quad (3.35c)$$

The CZ stiffness matrix, \underline{H}_{cz} , is derived as follows:

$$\underline{H}_{cz} = \frac{\partial \underline{t}}{\partial \delta} + \frac{\partial \underline{t}}{\partial d} \frac{\partial d}{\partial \lambda} \frac{\partial \lambda}{\partial \delta}, \quad (3.36)$$

where

$$\frac{\partial \underline{t}}{\partial \delta} = \begin{bmatrix} \frac{\partial t_n}{\partial \delta_n} & \frac{\partial t_n}{\partial \delta_s} \\ \frac{\partial t_s}{\partial \delta_n} & \frac{\partial t_s}{\partial \delta_s} \end{bmatrix} = k_0 \begin{bmatrix} 1 - d \mathcal{H}(\delta_n) & 0 \\ 0 & (1 - d) \beta^2 \end{bmatrix}, \quad (3.37a)$$

$$\frac{\partial t}{\partial d} = -k_0 \begin{bmatrix} \langle \delta_n \rangle \\ \beta^2 \delta_s \end{bmatrix}, \quad (3.37b)$$

$$\frac{\partial d}{\partial \lambda} = \begin{cases} 0 & \text{if } \lambda_{max} < \lambda_0 \\ \mathcal{F} \frac{1}{\lambda_{max}^2} \frac{\lambda_f \lambda_0}{\lambda_f - \lambda_0} & \text{if } \lambda_0 \leq \lambda_{max} \leq \lambda_f \\ 0 & \text{if } \lambda_{max} > \lambda_f, \end{cases} \quad (3.37c)$$

$$\frac{\partial \lambda}{\partial \delta} = \frac{1}{\lambda} \begin{bmatrix} \langle \delta_n \rangle & \beta^2 \delta_s \end{bmatrix}. \quad (3.37d)$$

In the above formulation, \mathcal{H} is the Heaviside function. The load function is denoted by \mathcal{F} which equals 1 in loading and 0 otherwise. The rest of the parameters have been addressed in Section 3.2.

3.8.2 Bulk elements

In general, there is no restriction on the constitutive behavior of the bulk material, but here for the sake of simplicity, a linear elastic material is assumed for which the constitutive relation (Equation (3.20)) can be stated as follows:

$$\underline{\sigma} = \underline{H}_{bulk} \underline{\varepsilon}, \quad (3.38)$$

where \underline{H}_{bulk} is the material elasticity matrix in the case of plane strain conditions:

$$\underline{H}_{bulk} = \frac{E}{(1+\nu)(1-2\nu)} \begin{bmatrix} 1-\nu & \nu & 0 \\ \nu & 1-\nu & 0 \\ 0 & 0 & (1-2\nu)/2 \end{bmatrix}. \quad (3.39)$$

with E the Young's modulus and ν the Poisson's ratio.

The tangential stiffness matrix of the bulk element contains the derivatives of the internal forces with respect to the element degrees of freedom:

$$\underline{K}_{bulk} = \begin{bmatrix} \underline{K}_{uu,bulk} & \underline{K}_{uh,bulk} & \underline{K}_{ua,bulk} \\ \underline{K}_{hu,bulk} & \underline{K}_{hh,bulk} & \underline{K}_{ha,bulk} \\ \underline{K}_{au,bulk} & \underline{K}_{ah,bulk} & \underline{K}_{aa,bulk} \end{bmatrix}, \quad (3.40a)$$

where:

$$\underline{K}_{uu,bulk} = \frac{\partial \underline{f}_{i,bulk}}{\partial \underline{u}} = \int_{\Omega} \underline{B}_{u,bulk}^T \underline{H}_{bulk} \underline{B}_{u,bulk} \, d\Omega, \quad (3.40b)$$

$$\underline{K}_{uh,bulk} = \frac{\partial \underline{f}_{i,bulk}}{\partial \underline{h}} = \int_{\Omega} \underline{B}_{u,bulk}^T \underline{H}_{bulk} \underline{B}_{h,bulk} \, d\Omega, \quad (3.40c)$$

$$\underline{K}_{hu,bulk} = \underline{K}_{uh,bulk}^T, \quad (3.40d)$$

$$\underline{K}_{ua,bulk} = \frac{\partial f_{i,bulk}}{\partial a} = \int_{\Omega} \underline{B}_{u,bulk}^T \underline{H}_{bulk} \underline{B}_{a,bulk} \, d\Omega, \quad (3.40e)$$

$$\underline{K}_{au,bulk} = \underline{K}_{ua,bulk}^T, \quad (3.40f)$$

$$\underline{K}_{hh,bulk} = \frac{\partial g_{i,bulk}}{\partial h} = \int_{\Omega} \underline{B}_{h,bulk}^T \underline{H}_{bulk} \underline{B}_{h,bulk} \, d\Omega, \quad (3.40g)$$

$$\underline{K}_{ha,bulk} = \frac{\partial g_{i,bulk}}{\partial a} = \int_{\Omega} \left(\frac{\partial \underline{B}_{h,bulk}^T}{\partial a} \underline{\sigma} + \underline{B}_{h,bulk}^T \underline{H}_{bulk} \underline{B}_{a,bulk} \right) \, d\Omega, \quad (3.40h)$$

$$\underline{K}_{ah,bulk} = \underline{K}_{ha,bulk}^T, \quad (3.40i)$$

$$K_{aa,bulk} = \frac{\partial b_{i,bulk}}{\partial a} = \int_{\Omega} \frac{\partial \underline{B}_{a,bulk}^T}{\partial a} \underline{\sigma} \, d\Omega + \int_{\Omega} \underline{B}_{a,bulk}^T \underline{H}_{bulk} \underline{B}_{a,bulk} \, d\Omega. \quad (3.40j)$$

In the above formulation:

$$\underline{B}_{a,bulk} = \begin{bmatrix} \frac{\partial^2 \psi}{\partial n \partial a} & 0 \\ 0 & \frac{\partial^2 \psi}{\partial s \partial a} \\ \frac{\partial^2 \psi}{\partial s \partial a} & \frac{\partial^2 \psi}{\partial n \partial a} \end{bmatrix} \underline{h}, \quad (3.41a)$$

$$\frac{\partial \underline{B}_{h,bulk}^T}{\partial a} = \begin{bmatrix} \frac{\partial^2 \psi}{\partial n \partial a} & 0 & \frac{\partial^2 \psi}{\partial s \partial a} \\ 0 & \frac{\partial^2 \psi}{\partial s \partial a} & \frac{\partial^2 \psi}{\partial n \partial a} \end{bmatrix}, \quad (3.41b)$$

$$\frac{\partial \underline{B}_{a,bulk}^T}{\partial a} = \underline{h}^T \begin{bmatrix} \frac{\partial^3 \psi}{\partial n \partial a^2} & 0 & \frac{\partial^3 \psi}{\partial s \partial a^2} \\ 0 & \frac{\partial^3 \psi}{\partial s \partial a^2} & \frac{\partial^3 \psi}{\partial n \partial a^2} \end{bmatrix}. \quad (3.41c)$$

A three-dimensional self-adaptive cohesive zone model¹

Abstract

Discrete crack models with cohesive binding forces in the fracture process zone have been widely used to address failure in quasi-brittle materials and interfaces. However, the numerical concerns and limitations stemming from the application of interface cohesive zone models in a quasi-static finite element framework considerably increase as the relative size of the process zone decreases. An excessively fine mesh is required in the process zone to accurately resolve the distribution of tractions in a relatively small moving zone. With a moderate mesh size, inefficient path-following techniques have to be employed to trace the local discretization-induced snap-backs. In order to increase the applicability of cohesive zone models by reducing their numerical deficiencies, a self-adaptive finite element framework is proposed, based on a hierarchical enrichment of the standard elements. With this approach, the planar mixed-mode crack growth in a general three-dimensional continuum, discretized by a coarse mesh, can be modeled while the set of equations of the non-linear system is solved by a standard Newton-Raphson iterative procedure. This hierarchical scheme was found to be most effective in reducing the oscillatory behavior of the global response.

¹*Reproduced from: M. Samimi, J.A.W. van Dommelen, and M.G.D Geers. A three-dimensional self-adaptive cohesive zone model for interfacial delamination. To be submitted.*

4.1 Introduction

Integration of dissimilar materials in structural components has gained considerable attraction in the last several decades, giving unique mechanical properties in different engineering applications. However, the presence of different interfaces in laminated structures triggers interfacial failure, mainly in the form of delamination, which results in malfunction or failure at the global level. Therefore, efficient and robust numerical models, supported by dedicated experiments to characterize the interface properties, are required for a prior assessment of the system reliability and performance.

Based on the early work of Griffith and Irwin on perfectly brittle materials [51,61], linear elastic fracture mechanics (LEFM) based models have been developed for the numerical simulation of crack propagation [23,72,93,101]. This class of methods has been extensively used in different applications from piezoelectric materials [92] to functionally graded coatings [9]. While different criteria such as the maximum circumferential stress, maximum strain energy release rate, and the minimum strain energy density [19,31], have been proposed and successfully applied to approximate crack propagation, LEFM approaches typically suffer from the lack of a criterion to predict crack initiation [140]. Moreover, capturing the propagation of multiple cracks is not straightforward in this framework [103].

Avoiding a persistent mesh refinement at the tip of a propagating crack is crucial for the practical applicability of any numerical methodology tackling this phenomenon. Therefore, motivated by the exploitation of the partition of unity concept [38,39,77], extended finite elements (X-FEM) have been developed [13]. The analytical solution for the singular field in an elastic solid has been used in the interpolation of finite elements around the crack tip, while a Heaviside function is used to account for the strong discontinuity inside the cracked elements [84]. An enhanced deformation approximation at the crack faces and the crack tip allows to use a relatively coarse discretization. The formulation was later extended to three-dimensional crack growth and multiple branched cracks [32,117]. X-FEM has also been used for the simulation of cohesive crack growth [26,76,83,134,136].

In another attempt to reduce the mesh size sensitivity in analyzing localization in strain softening materials, and inspired by earlier work on embedded weak discontinuities [14,90], the embedded localization line concept has been developed where a discontinuity line characterized by a traction-displacement law is introduced inside the element [41]. The concept of elements with embedded discontinuities was further extended and generalized to different types of finite elements to form another class of discrete crack approaches [68,75,87,88]. Embedded discontinuity approaches have been classified within a unified framework [64,66], and their variational formulation as well as numerical implementation aspects have been compared to X-FEM [65,89]. In contrast with X-FEM, the additional degrees of freedom in an element with an embedded discontinuity are condensed at the element level.

Another approach has been proposed where phantom elements/nodes are super-

posed on the existing mesh, allowing the discontinuity to grow at arbitrary locations inside the elements [54]. Using standard finite element basis functions for both existing and phantom nodes, the methodology has been applied for the simulation of cohesive cracks in two and three-dimensional continua [78,79]. While being equivalent to X-FEM in the sense that additional degrees of freedom are introduced at the enriched nodes, this approach is simpler to implement in commercial finite element codes and more practical to use in explicit dynamic analyses [115]. As an improvement to the original approach, where a discontinuity crosses the entire element, a new crack tip element formulation allows the crack tip to be placed inside the element [96].

For most of the aforementioned methodologies, the fracture process zone size has to be negligibly small compared to any structural dimension which is apparently not valid for many quasi-brittle materials [37, 137]. In such cases, the fracture process zone and the embedded cohesive tractions have to be modeled explicitly. Cohesive zone models have been developed over the past decades to address this issue [10, 40, 58, 85]. Using cohesive zone models, the non-physical singular stress field at the crack tip is eliminated by introducing a cohesive zone in the process zone. The decohesion mechanism is characterized by a phenomenological traction-separation law reflecting the average micromechanical behavior in the degradation process [24, 35]. Cohesive zone models adequately predict the initiation of a crack and its subsequent growth [30], while they can also be used for multiple interacting crack problems [100].

Consistent with the modeling of strong discontinuities [86], cohesive cracks can be simply modeled within a continuum finite element framework by adding extra degrees of freedom along the discontinuity via interface elements [60, 104]. For an existing interface, cohesive zone elements are typically inserted between continuum elements. Since the potential crack paths should be identified a priori, this approach is well suited for the simulation of interfacial delamination in layered structures with known interfaces [5, 6, 21, 111, 131].

The fracture process zone has to be resolved sufficiently accurately to ensure a smooth redistribution of energy in the bulk when softening occurs in the interface [3, 16, 22, 44, 55, 82, 119, 122, 124]. Spurious oscillations occur for coarse discretizations if the interfacial behavior is rather brittle and the process zone is quite small compared to the structural dimensions. To track these oscillations, expensive path-following techniques are required to enable the Newton-Raphson iterative scheme to follow discretization-induced snap-backs in the global load-displacement response.

Global path-following techniques have been developed where a constraint equation is added to the set of linearized equations to control the load step size [27, 98, 102]. Improved cylindrical arc-length control methods can overcome the non-smoothness even in the case of relatively sharp snap-backs [57]. However, global approaches where all degrees of freedom contribute equally to the constraint equation, are not efficient when deformation is highly localized, i.e. in the process zone of a cohesive crack in a quasi-brittle body. Revising the constraint equation involving only degrees

of freedom related to the localized zone significantly enhances the performance of these methods [34, 45, 46, 110]. Due to its monotonically increasing nature, the crack length has often been used as the control parameter to detect snap-backs [17]. The combination of local path following techniques and line searches can be used at the cost of expensive computations [4]. An efficient path-following constraint based on the energy dissipated in the failure process has been recently presented [53].

The applicability of quasi-brittle cohesive zone models is compromised by the extensive computations required to guarantee a stable numerical solution. To address this problem, there have been some proposals to increase the robustness of these models via a local enrichment of the elements within or in the vicinity of the process zone by higher order interpolation functions [28, 52]. However, the fixed functions used do not adequately address the adaptivity of the process zone within the interface. Recently, a variational X-FEM formulation has been proposed in a two-dimensional domain so that the crack propagation direction and the length of the discontinuity segment created in each step of an incremental procedure were regarded as additional degrees of freedom for which their values could be determined by minimization of the total energy of the global system [80, 81]. However, extension of the proposed strategy to three-dimensional cases would be quite cumbersome, at least from an implementation point of view. Moreover, in the case of known interfaces, an X-FEM based approach is not required.

Cohesive zone models were formulated within a self-adaptive finite element framework where the interface and bulk elements in the fracture process zone have been enriched to give a better approximation of the local delamination process [109]. Application of an adaptive hierarchical extension of the conventional finite element interpolation functions refines the discretization where the physics of the underlying problem needs it. The enrichment degrees of freedom were calculated by solving the global system of equations. The formulation has been extended to simulate mixed-mode delamination [106]. Application of the elaborated enrichment eliminates the need for a further mesh refinement while keeping the standard Newton-Raphson approach applicable in the case of a relatively coarse mesh which saves considerable computational costs.

In this chapter, the self-adaptive finite element formulation presented in [106, 109] is extended to cover delamination problems in a three-dimensional context. Extending 2D concepts to 3D, a practical and efficient enrichment strategy in planar interfaces is proposed, where all edges of an interface element are enriched by adding adaptive nodes. The uniqueness of the solution is guaranteed by adding appropriate penalties to the system [106]. The displacement fields in all bulk elements neighboring enriched interface elements are also enhanced. Straight delamination in a peel-off test with a crack front parallel to element boundaries is addressed first and successfully modeled within this framework. The performance of the developed methodology is assessed qualitatively by showing the global load-displacement responses of the structure undergoing a delamination process. The fluctuations have been scrutinized by identifying their main oscillatory components and their associated amplitudes.

In general, the hierarchical formulation allows for a general application of the methodology to three-dimensional crack growth problems. In the case of delamination with an oblique front (not aligned with element edges), adding hierarchical extensions to conventional finite element interpolation functions does not preserve a constant crack front with a sharp kink in the separation profile of a cohesive crack when propagating through the element. In order to analyze this property, an alternative basis of finite element interpolation functions is used as well and made dependent on the position of the adaptive nodes. The performance of this non-hierarchical scheme is evaluated and compared to the hierarchical framework. A drawback of this non-hierarchical strategy is the replacement of the conventional shape functions and the increase of the number of global degrees of freedom. Analyzing both options, the hierarchical enrichment is found to be most efficient in reducing oscillations in the global force-displacement response, with an acceptable accuracy at the crack front.

The application of self-adaptive finite elements enhances the robustness and efficiency of the cohesive zone modeling by alleviating the need for a fine discretization in the case of brittle interfaces. This chapter makes the methodology applicable to three-dimensional interfacial delamination problems with arbitrary crack growth patterns. In general, the behavior of an enriched model, either brittle or ductile, is significantly more smooth compared to its non-enriched counterpart. Therefore, standard Newton-Raphson iterative schemes remain applicable when the exact solution of the problem does not contain limit points, including a considerable reduction in computational effort. The chapter finishes with a general conclusion and perspective on the proposed 3D methodology.

4.2 Self-adaptive 3D finite elements

Using interface cohesive zone models within a finite element framework, the domain is commonly discretized by bulk and interface elements. While an arbitrary stress-strain (σ - ϵ) relationship is employed to describe the bulk behavior, the decohesion process is typically characterized by a traction-separation (t - δ) law within interface elements [142].

Ignoring body forces acting on the domain Ω , the virtual work principle leads to the global equilibrium equation:

$$\int_{\Omega} d\boldsymbol{\xi}^T \boldsymbol{\sigma} d\Omega + \int_{\Gamma_c} d\boldsymbol{\delta}^T \boldsymbol{t} d\Gamma_c = \int_{\Gamma_t} d\boldsymbol{u}^T \bar{\boldsymbol{t}} d\Gamma_t, \quad (4.1)$$

where $d\boldsymbol{\xi}$ and $d\boldsymbol{\delta}$ represent small strain and small separation perturbations in the bulk and cohesive zone, respectively. The cohesive zone or the internal boundary on which the cohesive forces \boldsymbol{t} are applied is represented by Γ_c . Dirichlet and Neumann

boundary conditions are defined as follows:

$$\underline{u} = \bar{\underline{u}} \quad \text{on} \quad \Gamma_u, \quad (4.2a)$$

$$\underline{\sigma}^T \underline{n}_t = \bar{\underline{t}} \quad \text{on} \quad \Gamma_t. \quad (4.2b)$$

where the external boundary on which the external tractions $\bar{\underline{t}}$ are applied is denoted by Γ_t for which the components of the outward normal vector are stored in the column \underline{n}_t . Displacements $\bar{\underline{u}}$ are prescribed on the external boundary Γ_u . The whole external boundary is $\Gamma = \Gamma_t \cup \Gamma_u$. The stress components are collected in the column $\underline{\sigma}$ in Equation (4.1) and in the symmetric matrix $\underline{\sigma}$ in Equation (4.2b).

A self-adaptive interfacial discretization scheme has been developed in 2D to deal with delamination in brittle interfaces, using a relatively coarse mesh [106]. The developed methodology enriches the discretized domain by enhancing the description of the separation within the cohesive zone as well as the displacement field in the adjacent bulk element in a 3D setting, allowing for a more accurate approximation of deformation in the fracture process zone due to the enrichment adaptivity.

4.2.1 Interface element kinematics

Planar cohesive zone elements with an initially zero thickness and an enriched description of the 3D kinematics are formulated. As shown in Figure 4.1, eight-node interface elements, which are compatible with eight-node continuum brick elements, are utilized here [50]. The upper surface Γ^+ and the bottom surface Γ^- are coinciding in the initial configuration. The element has 2×4 nodes with a fixed position, denoted by $n_i^{+/-}$, $i = 1, \dots, 4$, which results in a total number of 24 standard displacement degrees of freedom for the entire element.

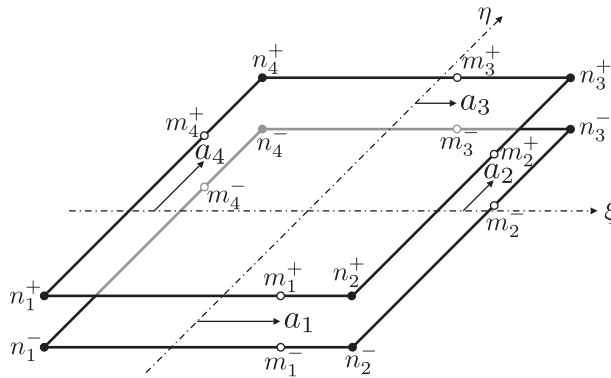


Figure 4.1: An eight-node self-adaptive interface element in isoparametric coordinates (hierarchical enrichment).

In a conventional finite element framework, the displacement of the element surfaces is determined through the standard interpolation functions $N_i(\xi, \eta)$, $i = 1, \dots, 4$,

with $(\xi, \eta) \in [-1, 1]$ the isoparametric coordinates. Planar interface elements are enriched along all edges by bi-linear functions with mobile peak positions. In Figure 4.1, adaptive nodes are denoted by $m_j^{+/-}$, $j = 1, \dots, 4$ and their respective positions are given by the degrees of freedom $a_j \in [-1, 1]$, $j = 1, \dots, 4$. The piece-wise planar enrichment functions, $\phi_j(\xi, \eta, a_k | k = 1, \dots, 4)$, $j = 1, \dots, 4$ are shown in Figure 4.2, with a maximum value of 1 at their associated adaptive nodes $m_j^{+/-}$. Note that each enrichment function depends on the enrichment position at each of the element edges. The interfacial separation is then determined as follows:

$$\underline{u}^+ = \sum_{i=1}^4 N_i \underline{u}_i^+ + \sum_{j=1}^4 \phi_j(a_k | k = 1, \dots, 4) \underline{h}_j^+, \quad (4.3a)$$

$$\underline{u}^- = \sum_{i=1}^4 N_i \underline{u}_i^- + \sum_{j=1}^4 \phi_j(a_k | k = 1, \dots, 4) \underline{h}_j^-, \quad (4.3b)$$

$$\underline{\delta} = \underline{u}^+ - \underline{u}^- = \underline{B}_u \underline{u}_e + \sum_{j=1}^4 \underline{B}_{h_j}(a_k) \underline{h}_j, \quad (4.3c)$$

where \underline{h}_j^+ , \underline{h}_j^- denote columns of enrichment amplitudes at the j^{th} mobile enrichment peak point at the upper and bottom element surfaces, respectively. The columns \underline{u}_e and \underline{h}_j collect all nodal displacements and the enrichment amplitude degrees of freedom at the j^{th} edge, respectively. As can be seen in Equations (4.3), the enrichment peak positions, as well as the enrichment amplitudes at all four edges of the interface element, are introduced as additional degrees of freedom.

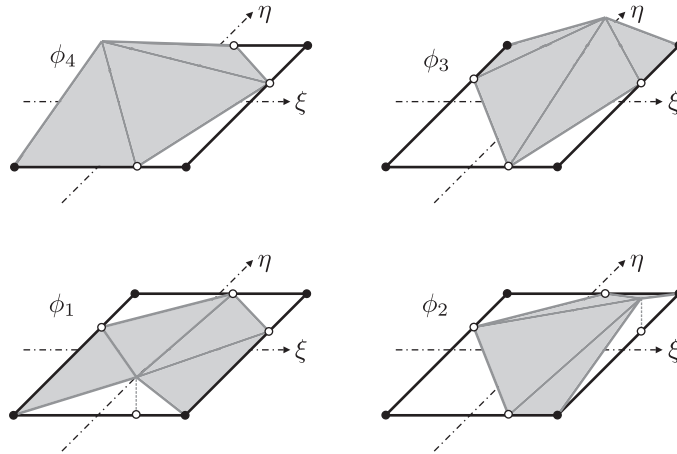


Figure 4.2: Hierarchical interpolation functions used to extend standard finite element interpolation functions.

The internal work done in an enriched interface element on the internal boundary

$\Gamma_{c_e} \in \Gamma_c$ reads:

$$\begin{aligned} \int_{\Gamma_{c_e}} \mathbf{d}\tilde{\delta}^T \underline{t} \, d\Gamma_{c_e} &= \int_{\Gamma_{c_e}} \left(\frac{\partial \delta}{\partial \underline{u}_e} \mathbf{d}\underline{u}_e + \sum_{j=1}^4 \frac{\partial \delta}{\partial \underline{h}_j} \mathbf{d}\underline{h}_j + \sum_{k=1}^4 \frac{\partial \delta}{\partial a_k} \mathbf{d}a_k \right)^T \underline{t} \, d\Gamma_{c_e} \\ &= \int_{\Gamma_{c_e}} \left(\underline{B}_u \mathbf{d}\underline{u}_e + \sum_{j=1}^4 \underline{B}_{h_j} \mathbf{d}\underline{h}_j + \sum_{k=1}^4 \underline{B}_{a_k} \mathbf{d}a_k \right)^T \underline{t} \, d\Gamma_{c_e}, \end{aligned} \quad (4.4)$$

with

$$\underline{B}_{a_k} = \sum_{j=1}^4 \frac{\partial \underline{B}_{h_j}}{\partial a_k} \underline{h}_j. \quad (4.5)$$

The internal forces associated with the displacement degrees of freedom \underline{f}_{int} , the amplitudes at the j^{th} edge $g_{int}^{(j)}$, and the enrichment peak position at the k^{th} edge $b_{int}^{(k)}$ are derived using Equation (4.4):

$$\underline{f}_{int} = \int_{\Gamma_{c_e}} \underline{B}_u^T \underline{t} \, d\Gamma_{c_e}, \quad (4.6a)$$

$$g_{int}^{(j)} = \int_{\Gamma_{c_e}} \underline{B}_{h_j}^T \underline{t} \, d\Gamma_{c_e}, \quad j = 1, \dots, 4, \quad (4.6b)$$

$$b_{int}^{(k)} = \int_{\Gamma_{c_e}} \underline{B}_{a_k}^T \underline{t} \, d\Gamma_{c_e}, \quad k = 1, \dots, 4. \quad (4.6c)$$

In order to establish the set of non-linear equations for the unknowns associated with an enriched interface element, the tangential stiffness matrix can be determined in a straightforward manner analogous to the 2D case [106]. The kinematics of the cohesive zone element are formulated within local coordinates $\{\mathbf{n}, \mathbf{s}_1, \mathbf{s}_2\}$ which requires a transformation of vectorial fields to global coordinates $\{\mathbf{x}, \mathbf{y}, \mathbf{z}\}$ before a global system assembly in a finite element framework.

4.2.2 Bulk element kinematics

Eight-node brick elements are used to discretize the three-dimensional continuum. Each node has three displacement degrees of freedom. In a conventional finite element framework, the displacement field is interpolated through standard shape functions $N_i(\xi, \eta, \zeta)$, $i = 1, \dots, 8$, with $(\xi, \eta, \zeta) \in [-1, 1]$ the corresponding isoparametric coordinates. The kinematic description of the bulk element surface which is connected to a surface of an enriched interface element is enriched as well to ensure continuity of the displacement field at the internal cohesive boundary (see Figure 4.3). The effect of the enrichment vanishes linearly with coordinate ζ through the thickness of the enriched bulk element from the enriched surface to the non-enriched

surface:

$$\underline{u} = \sum_{i=1}^8 N_i \underline{u}_i + \sum_{j=1}^4 \psi_j(a_k | k = 1, \dots, 4) \underline{h}_j, \quad (4.7)$$

with

$$\psi_j = \frac{1}{2} (1 - \zeta) \phi_j(a_k), \quad j = 1, \dots, 4. \quad (4.8)$$

The strain field in the bulk material is then given by:

$$\underline{\epsilon} = \underline{B}_u \underline{u}_e + \sum_{j=1}^4 \underline{B}_{h_j}(a_k) \underline{h}_j, \quad (4.9)$$

where the column $\underline{\epsilon}$ collects the strain components and the columns \underline{u}_e and \underline{h}_j collect all nodal displacements and the enrichment amplitude degrees of freedom at the j^{th} enriched edge, respectively.

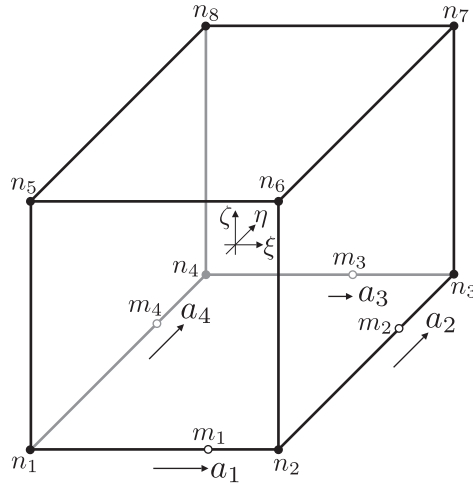


Figure 4.3: An eight-node self-adaptive bulk element in isoparametric coordinates (hierarchical enrichment).

The virtual work done in an enriched bulk element with sub-domain $\Omega_e \in \Omega$ reads:

$$\begin{aligned} \int_{\Omega_e} \underline{d}\underline{\epsilon}^T \underline{\sigma} \, d\Omega_e &= \int_{\Omega_e} \left(\frac{\partial \underline{\epsilon}}{\partial \underline{u}_e} \underline{d}\underline{u}_e + \sum_{j=1}^4 \frac{\partial \underline{\epsilon}}{\partial \underline{h}_j} \underline{d}\underline{h}_j + \sum_{k=1}^4 \frac{\partial \underline{\epsilon}}{\partial a_k} \underline{d}a_k \right)^T \underline{\sigma} \, d\Omega_e \\ &= \int_{\Omega_e} \left(\underline{B}_u \underline{d}\underline{u}_e + \sum_{j=1}^4 \underline{B}_{h_j} \underline{d}\underline{h}_j + \sum_{k=1}^4 \underline{B}_{a_k} \underline{d}a_k \right)^T \underline{\sigma} \, d\Omega_e, \end{aligned} \quad (4.10)$$

with

$$\underline{B}_{a_k} = \sum_{j=1}^4 \frac{\partial \underline{B}_{h_j}}{\partial a_k} h_j. \quad (4.11)$$

The internal forces associated with the displacement degrees of freedom \underline{f}_{int} , enrichment amplitudes at the j^{th} edge $g_{int}^{(j)}$, and the enrichment peak position at the k^{th} edge $b_{int}^{(k)}$ are then given by:

$$\underline{f}_{int} = \int_{\Omega_e} \underline{B}_u^T \underline{\sigma} \, d\Omega_e, \quad (4.12a)$$

$$g_{int}^{(j)} = \int_{\Omega_e} \underline{B}_{h_j}^T \underline{\sigma} \, d\Omega_e, \quad j = 1, \dots, 4, \quad (4.12b)$$

$$b_{int}^{(k)} = \int_{\Omega_e} \underline{B}_{a_k}^T \underline{\sigma} \, d\Omega_e, \quad k = 1, \dots, 4. \quad (4.12c)$$

Analogous to the 2D case for the enriched bulk element [106], the tangential stiffness matrix can be determined to establish the set of non-linear equations. When the bulk element kinematics are formulated within local coordinates $\{\mathbf{n}, \mathbf{s}_1, \mathbf{s}_2\}$, a transformation of vectorial fields to global coordinates $\{\mathbf{x}, \mathbf{y}, \mathbf{z}\}$ is required before a global system assembly.

4.2.3 Numerical implementation

The main purpose of the proposed self-adaptive cohesive zone elements is to provide a more accurate approximation of deformation in the delaminating process zone while maintaining a coarse mesh. This is achieved by enriching the standard FE interpolation with a hierarchical extension that traces the moving crack tip along the element edge. The adaptivity of the enriched edges (swept by the delamination front) ensures an accurate numerical approximation of the physical crack propagation (see Figure 4.4 for different crack growth patterns).

Identification of the location of the fracture process zone and thereby enriching only elements near the process zone increases the efficiency and accuracy of the methodology. Likewise, special care needs to be given to the accurate integration of the enriched elements. Moreover, ensuring uniqueness and convergence of the solution of the resulting non-linear system is crucial for the robustness of the self-adaptive algorithm.

Enrichment strategy

An adaptive enrichment strategy for normal separation modes has been applied to cohesive zone interface elements located in the fracture process zone in two-

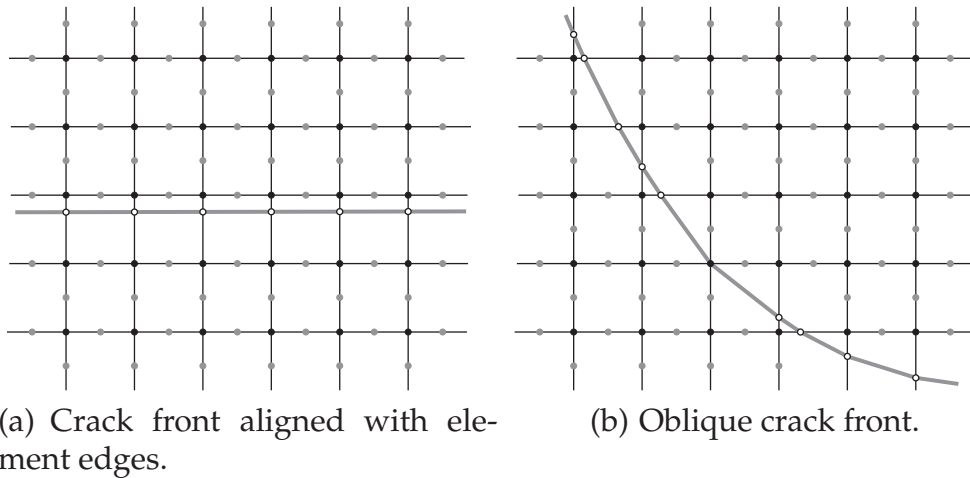


Figure 4.4: Delamination growth patterns with a planar interface (Black and grey filled dots denote interface nodes and enrichment peak positions, respectively. Hollow dots denote repositioned enrichment peak positions to accommodate the moving crack front. The approximated delamination front is shown by the thick grey line).

dimensional problems [109]. This procedure, extended to an effective separation, is next used to enrich a three-dimensional cohesive zone framework.

Numerical integration

The self-adaptive cohesive zone elements enhance the discretization through hierarchical extensions. To obtain a sufficiently accurate integration scheme (i.e. for an adaptive piece-wise planar opening profile), either a high number of fixed integration points can be used or each linear subregion can be integrated separately with a lower order Gaussian integration scheme. Compared to a higher number of fixed integration points, triangularization of the interface element and integrating each part separately reduces the number of integration points, still keeping a sufficiently high accuracy. This procedure is less efficient when history parameters, such as accumulated plastic strain or damage, have to be stored in integration points. The required adaptivity would then necessitate a transport step of the history data at each incremental step. To prevent this, the tangential stiffness and internal forces associated with the enriched element degrees of freedom are calculated using a high-order Gaussian integration scheme. In the current study, 10×10 integration points with fixed positions have been used in the ξ - η plane of the enriched interface plane and its adjacent bulk element, while only 2 layers of integration points are needed to resolve the enriched linear elastic bulk element in the ζ direction.

Solution convergence and uniqueness

The additional degrees of freedom introduced in the self-adaptive cohesive zone elements (i.e. enrichment peak positions and amplitudes), are calculated by means of a potential minimization of the assembled system. Minimizing the potential with respect to the enrichment peak position, a procedure was proposed by the authors in a previous chapter to trace its incremental value in a two-dimensional setting [106]. Depending on the separation profile at each edge of a self-adaptive interface element, an initial estimate for its associated enrichment peak position is made close to the corner where delamination enters. The peak position is then incrementally adapted as delamination grows. More details on incremental adaptation of the enrichment peak position within an edge of a planar interface element based on the effective separations at both ends of that edge (which is treated similar to a linear interface element in a 2D setting), can be found in [106].

A stabilization procedure has to be implemented to restore uniqueness if no enrichment is needed, allowing to determine the positions of the enrichment peaks at all conditions. Therefore, a small (negligible with respect to the physical solution) adaptive penalty is imposed on the enrichment peak positions to ensure a unique solution when the potential variation with respect to these degrees of freedom is negligible. Another penalty is applied close to element corners at all enriched edges to constrain the enrichment peak positions inside the element [106]. Note that when the enrichment peak position within an arbitrary edge is close to a corner, the effect of the enrichment along that edge is negligible and the standard nodal interpolations suffice for the numerical approximation. Since the penalizations in 3D are conceptually not different from those in 2D, the details are not presented here but can be found in [106].

4.3 Numerical examples

The enriched self-adaptive 3D cohesive zone elements are here demonstrated on a crack growth problem with planar interfaces in a three-dimensional continuum.

4.3.1 Problem statement

A propagating delamination crack is modeled in a pre-cracked interface between a plate glued to a rigid substrate. The specimen is pulled at its free end as shown in Figure 4.5. Based on the displacement profile prescribed at the free end of the plate, a moving crack front is obtained that is either aligned or oblique with respect to element edges. The specimen bulk is linear elastic, characterized by its Young's modulus, $E = 100$ (GPa), and Poisson's ratio, $\nu = 0.3$. The sample is discretized by $(10 + 40) \times 6 \times 4$ brick elements. The kinematics of enriched bulk and interface elements are elaborated in Section 4.2. The interface is discretized with a coarse mesh

of 40×6 two-dimensional interface elements in the x - y plane. A mixed-mode bi-linear traction-separation law is considered to characterize the interfacial behavior (see the next subsection).

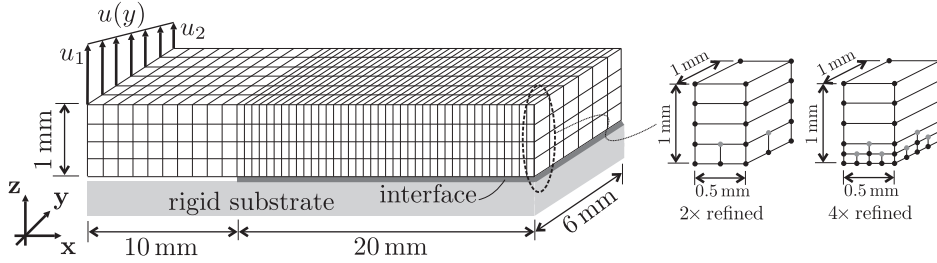


Figure 4.5: Three-dimensional peel-off problem; geometry, boundary conditions, and bulk refinement (double and quadruple bulk refinement is carried out in both x and y directions only in the bulk element layer adjacent to the interface and the rest of the bulk elements are unaltered; the grey nodes are tied).

4.3.2 Constitutive model for mixed-mode delamination

Within a 3D interface cohesive zone model, the degradation of the adhesive bonds relate to normal (mode I) and planar (modes II and III) opening, which triggers a mixed-mode failure of an interfacial point. A bi-linear traction-separation law is adopted here [141, 142]. The interface constitutive law is defined with respect to an effective scalar separation and an effective scalar traction [63, 91]. Delamination initiates when the effective traction reaches the interface strength at an interfacial point, whereas its growth is controlled by the energy required to create the fracture surfaces. The latter, which is the area under the traction-separation curve, is the critical energy release rate and can be experimentally determined [70, 71].

A local or element coordinate system $\{\mathbf{n}, \mathbf{s}_1, \mathbf{s}_2\}$ is used [12, 21]. Using this three-dimensional coordinate system, interfacial separation and traction vectors are defined as $\boldsymbol{\delta}$ and \mathbf{t} , respectively:

$$\boldsymbol{\delta} = \delta_n \mathbf{n} + \delta_{s_1} \mathbf{s}_1 + \delta_{s_2} \mathbf{s}_2, \quad (4.13a)$$

$$\mathbf{t} = t_n \mathbf{n} + t_{s_1} \mathbf{s}_1 + t_{s_2} \mathbf{s}_2, \quad (4.13b)$$

where unit vectors \mathbf{s}_1 and \mathbf{s}_2 denote the two in-plane directions which are mutually perpendicular while \mathbf{n} is the unit vector normal to the interface mid-plane. The effective separation is defined as:

$$\lambda = \sqrt{\langle \delta_n \rangle^2 + \beta^2 (\delta_{s_1}^2 + \delta_{s_2}^2)}. \quad (4.14)$$

Here, it is assumed that the delamination behavior in mode II and III is identical,

i.e. the interfacial strength is identical in all in-plane directions. Parameter β denotes the ratio between planar and normal strengths. As implied by the application of Macaulay brackets in Equation (4.14), the compressive interpenetration of the interface surfaces is not taken into account for the calculation of the effective separation [106].

A bi-linear traction-separation law relates the scalar effective separation to a scalar effective traction, t , under mixed-mode loading conditions (see Figure 4.6):

$$t = \begin{cases} k_0 \lambda & \text{if } \lambda \leq \lambda_0 \\ t_0 \left(\frac{\lambda_f - \lambda}{\lambda_f - \lambda_0} \right) & \text{if } \lambda_0 < \lambda \leq \lambda_f \\ 0 & \text{if } \lambda > \lambda_f. \end{cases} \quad (4.15)$$

The effective traction t increases linearly with a stiffness k_0 as the effective separation increases until it reaches a maximum $t_0 = k_0 \lambda_0$ at the characteristic separation λ_0 . Further separation results in a linear decrease of the traction until the failure separation λ_f is reached. The fracture toughness G_c or the energy required to produce traction-free surfaces equals the area under the traction-separation curve:

$$G_c = \int_0^{\lambda_f} t \, d\lambda = \frac{1}{2} t_0 \lambda_f. \quad (4.16)$$

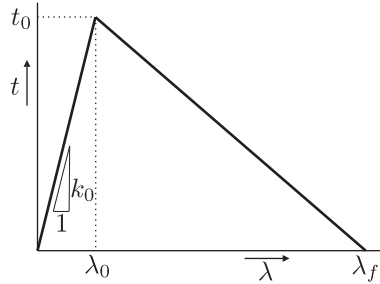


Figure 4.6: Bi-linear traction-separation law.

A cohesive potential energy functional, as considered e.g. in [91], is assumed here:

$$\phi_c(\lambda) = \begin{cases} \frac{1}{2} k_0 \lambda^2 & \text{if } \lambda \leq \lambda_0 \\ \frac{1}{2} k_0 \lambda_0 \left[\lambda_0 + (\lambda - \lambda_0) \left(1 + \frac{\lambda_f - \lambda}{\lambda_f - \lambda_0} \right) \right] & \text{if } \lambda_0 < \lambda \leq \lambda_f \\ \frac{1}{2} k_0 \lambda_0 \lambda_f & \text{if } \lambda > \lambda_f, \end{cases} \quad (4.17)$$

so that the expressions for traction components in normal and planar directions can be derived as follows:

$$t_n = \frac{\partial \phi_c}{\partial \delta_n} = \frac{\partial \phi_c}{\partial \lambda} \frac{\partial \lambda}{\partial \delta_n} = t \frac{\langle \delta_n \rangle}{\lambda} - k_0 \langle -\delta_n \rangle, \quad (4.18a)$$

$$t_{s_1} = \frac{\partial \phi_c}{\partial \delta_{s_1}} = \frac{\partial \phi_c}{\partial \lambda} \frac{\partial \lambda}{\partial \delta_{s_1}} = \beta^2 t \frac{\delta_{s_1}}{\lambda}, \quad (4.18b)$$

$$t_{s_2} = \frac{\partial \phi_c}{\partial \delta_{s_2}} = \frac{\partial \phi_c}{\partial \lambda} \frac{\partial \lambda}{\partial \delta_{s_2}} = \beta^2 t \frac{\delta_{s_2}}{\lambda}, \quad (4.18c)$$

where the interfacial behavior in compression is assumed to be linear elastic with stiffness k_0 in Equation (4.18a). The corresponding effective traction, which was introduced in Equation (4.15), is then given by:

$$t = \sqrt{t_n^2 + \beta^{-2} (t_{s_1}^2 + t_{s_2}^2)}. \quad (4.19)$$

For the numerical examples considered here, a monotonically increasing loading is applied. Therefore, the unloading behavior is not formulated here. However, the self-adaptive cohesive zone model can be applied within a general damage mechanics framework to account for the irreversibility of the interfacial failure [106].

The variation of the traction components ($\underline{t} = [t_n \ t_{s_1} \ t_{s_2}]^T$) with respect to the separation components ($\underline{\delta} = [\delta_n \ \delta_{s_1} \ \delta_{s_2}]^T$) within the interface is written as follows:

$$d\underline{t} = \underline{H}_{cz} d\underline{\delta}, \quad (4.20)$$

and the cohesive zone tangent matrix, \underline{H}_{cz} , is derived as follows:

$$\underline{H}_{cz} = \left. \frac{\partial \underline{t}}{\partial \underline{\delta}} \right|_{\lambda} + \left. \frac{\partial \underline{t}}{\partial \lambda} \right|_{\underline{\delta}} \frac{\partial \lambda}{\partial \underline{\delta}}, \quad (4.21a)$$

where

$$\left. \frac{\partial \underline{t}}{\partial \underline{\delta}} \right|_{\lambda} = \begin{bmatrix} \frac{\partial t_n}{\partial \delta_n} & \frac{\partial t_n}{\partial \delta_{s_1}} & \frac{\partial t_n}{\partial \delta_{s_2}} \\ \frac{\partial t_{s_1}}{\partial \delta_n} & \frac{\partial t_{s_1}}{\partial \delta_{s_1}} & \frac{\partial t_{s_1}}{\partial \delta_{s_2}} \\ \frac{\partial t_{s_2}}{\partial \delta_n} & \frac{\partial t_{s_2}}{\partial \delta_{s_1}} & \frac{\partial t_{s_2}}{\partial \delta_{s_2}} \end{bmatrix} = \begin{bmatrix} \frac{t}{\lambda} \mathcal{H}(\delta_n) + k_0 \mathcal{H}(-\delta_n) & 0 & 0 \\ 0 & \beta^2 \frac{t}{\lambda} & 0 \\ 0 & 0 & \beta^2 \frac{t}{\lambda} \end{bmatrix}, \quad (4.21b)$$

$$\left. \frac{\partial \underline{t}}{\partial \lambda} \right|_{\underline{\delta}} = \frac{1}{\lambda} \left(\frac{\partial t}{\partial \lambda} - \frac{t}{\lambda} \right) \begin{bmatrix} \langle \delta_n \rangle \\ \beta^2 \delta_{s_1} \\ \beta^2 \delta_{s_2} \end{bmatrix}, \quad (4.21c)$$

$$\frac{\partial \lambda}{\partial \underline{\delta}} = \frac{1}{\lambda} [\langle \delta_n \rangle \quad \beta^2 \delta_{s_1} \quad \beta^2 \delta_{s_2}]. \quad (4.21d)$$

For a given fracture toughness, the interfacial behavior becomes more brittle if the interface strength is higher. In these cases, a coarse mesh ceases to be applicable and a refined discretization or an enriched model is needed. The peel-off test is analyzed for an interface strength ranging from 20 (MPa) to 100 (MPa) and a fixed fracture toughness of 0.25 (N/mm). The brittleness thereby varies and allows to investigate

the effectiveness of a discretization refinement versus an enrichment. The same interfacial strength is assumed for normal and tangential modes ($\beta = 1$).

4.3.3 Cracks aligned with element edges

A delaminating crack aligned with element edges can be obtained if the plate is pulled uniformly at its free end ($u_1 = u_2$), as shown in Figure 4.5. Note that a small curvature can exist in the proximity of the lateral edges due to 3D stress effects. Both conventional and enriched cohesive zone models are used for the numerical simulation. To assess the role of mesh refinement (without enrichment), both the interface elements and their adjacent bulk elements are refined two and four times in both x and y directions with conventional cohesive zone elements. The rest of the bulk elements remain unchanged so that the secondary effect of mesh refinement on the plate bending behavior is minimized.

For an interface strength of 50 (MPa), and a coarse mesh of conventional elements, the global force-displacement diagram shows a monotonic increase in the applied load until a maximum is reached, see Figure 4.7. Right after this limit point, the first interface elements at the left start to soften and the resulting total reaction force starts to drop. For the considered coarse discretization, the force-displacement diagram shows an oscillatory behavior which results in a premature termination of the numerical routine. Further mesh refinement reduces the amplitude of the oscillations until a regular Newton-Raphson iterative scheme becomes applicable. However, the number of degrees of freedom increases as the mesh is refined. Figure 4.7 shows that the self-adaptive cohesive zone model applied to the most coarse mesh results in a global response which is even more smooth compared to the conventional approach with a 4×4 -times refined mesh. A standard Newton-Raphson approach is trivially applicable to trace the path in this case.

Conventional mesh refinement or using the hierarchical enrichment in the self-adaptive cohesive zone are both effective in reducing the oscillations in the global response. The effectiveness of both approaches is next assessed by quantifying the oscillating response using a Fourier analysis. A displacement-controlled loading is adopted, for which the oscillatory response is analyzed in the range of $u_1 \in [1.0, 1.8]$ mm. The spectrum of the oscillatory signal is retrieved using a conventional fast Fourier transform (fft) algorithm. The lowest frequencies (smaller than the main oscillation frequency), which represent the physical global response curvature are discarded. A range of $[5, 100]$ mm^{-1} is considered for the frequency of the oscillations.

The computational cost scales with the number of degrees of freedom used to discretize the problem. On the other hand, tracing an oscillatory path requires considerably more iterations and smaller increments which increases the CPU time even if no snap-back occurs (see Figure 4.8(a)). Even though a finer mesh results in a more smooth response, the response remains oscillatory, albeit with a smaller amplitude. In fact, high frequency oscillations with low amplitudes are created due to a refine-

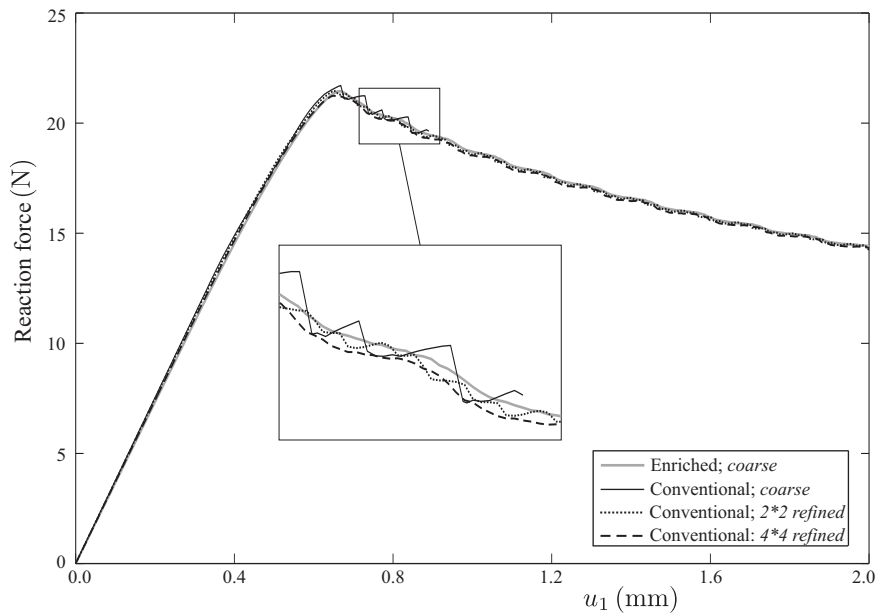


Figure 4.7: Force-displacement diagram of the three-dimensional peel-off problem with a delamination front aligned with element edges ($t_0 = 50$ MPa).

ment at the interface level, which are superimposed on lower frequency oscillations with higher amplitudes (see the multiple peaks in the spectrum of Figure 4.8(b)). As a result, smaller increments are required to trace high frequency oscillations. The self-adaptive cohesive zone model considerably smoothens the response while avoiding extra high frequency oscillations in the system, see Figure 4.8(d). The latter results in lower amplitude oscillations when compared to the 4×4 -times refined model using the conventional framework (see Figure 4.8(c)).

The global response of the peel-off test is next analyzed for different levels of interface brittleness, using both conventional (coarse and refined) and enriched cohesive zones. The area under the single-sided spectrum corresponds to a global measure of discretization-induced oscillations and can be used as an error indicator (see Figure 4.9(a)). The high-amplitude frequencies represent the main oscillation frequency and the corresponding amplitude denotes the main deviation from the physical smooth solution (see Figure 4.9(b)). The mesh-induced oscillations become more severe and the standard Newton-Raphson iterative scheme is not capable of tracing the oscillatory path anymore if the system becomes too brittle. For the most brittle cases ($t_0 > 70$ MPa), even the most refined mesh is not fine enough to avoid a discretization-induced numerical instability and the computations fail to converge at an early stage. Further analysis is only possible if path-following techniques are used in the conventional model. The self-adaptive finite element framework remains applicable until the target applied displacement of $u_1 = 2$ (mm) is reached, without a need for tracing the solution path with arc-length techniques for high brittleness levels.

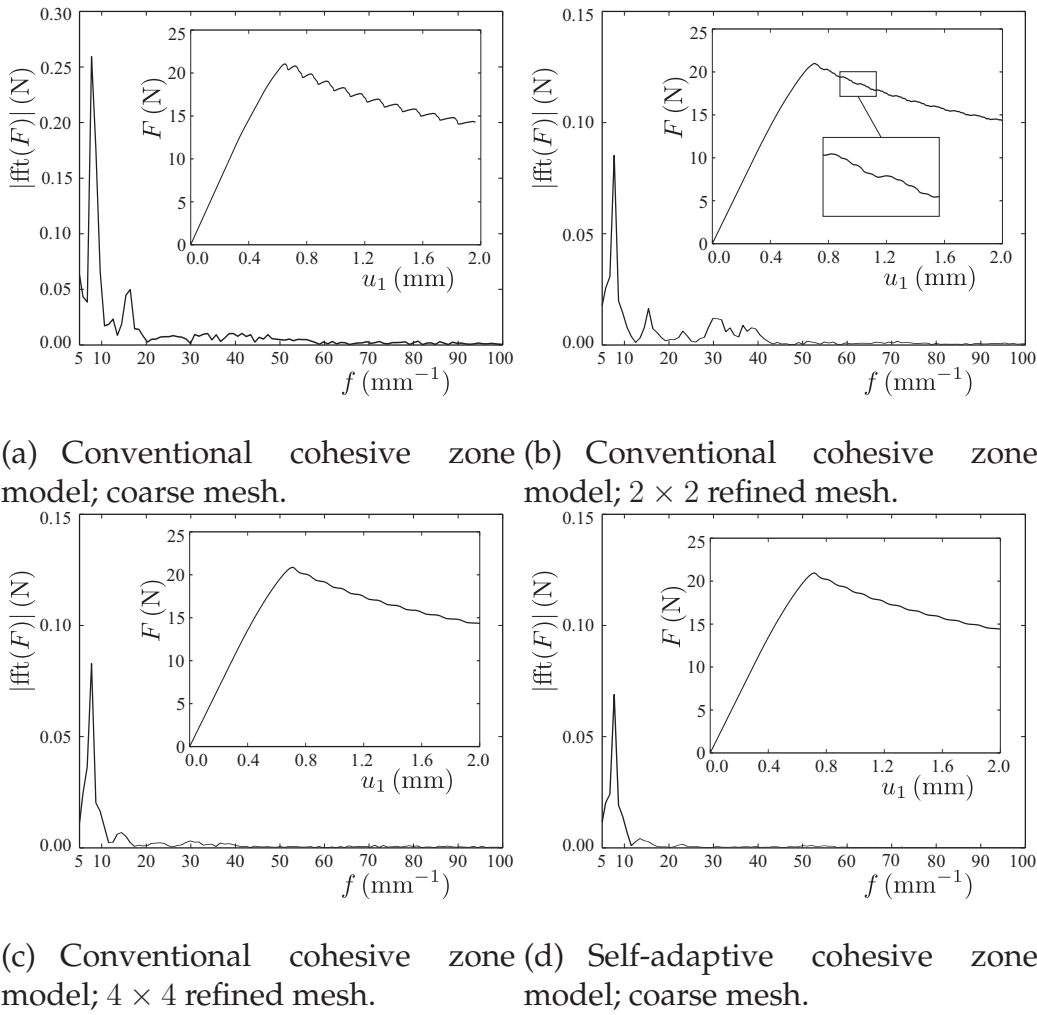
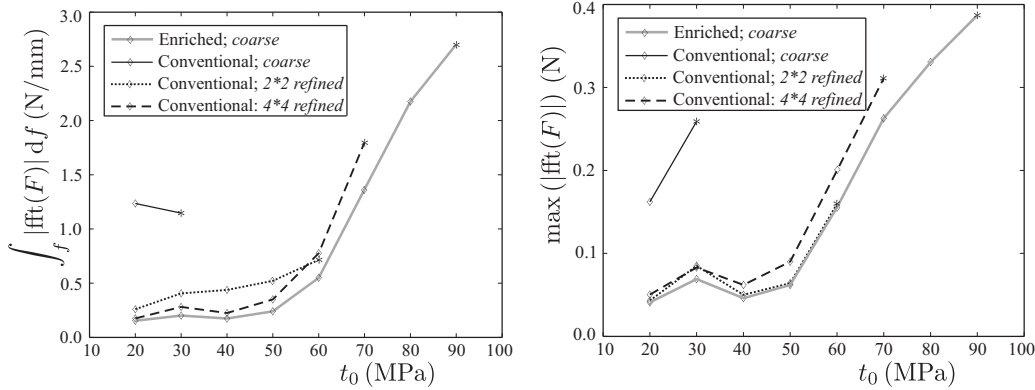


Figure 4.8: Delamination growth aligned with element edges; force-displacement diagrams and single-sided spectrums ($t_0 = 30$ MPa).

4.3.4 Cracks oblique with respect to element edges

An oblique delamination crack is obtained in the interface shown in Figure 4.5 when the plate is pulled non-uniformly at its free end. Here, a displacement along the z -axis is incrementally prescribed, distributed linearly along the free end of the plate so that $u_1 = 4u_2$. Similar to Section 4.3.3, both enriched and conventional (coarse and refined) cohesive zone models are used for the simulation of the problem.

The global force-displacement response of the structure is shown in Figure 4.10. The effect of the hierarchical self-adaptive enrichment on the global response of the most coarse mesh is comparable to a 4×4 -times refinement applied within the conventional cohesive zone model (see Figure 4.10), for which a standard Newton-Raphson iterative scheme is easily applicable.



(a) Area under the single-sided spectrum. (b) Highest oscillation amplitude.

Figure 4.9: Error based on a discrete Fourier transform of the oscillatory response for a crack front aligned with element edges (the data point shown by the asterisk * in each curve represents the most brittle level that can be solved with a standard Newton-Raphson scheme).

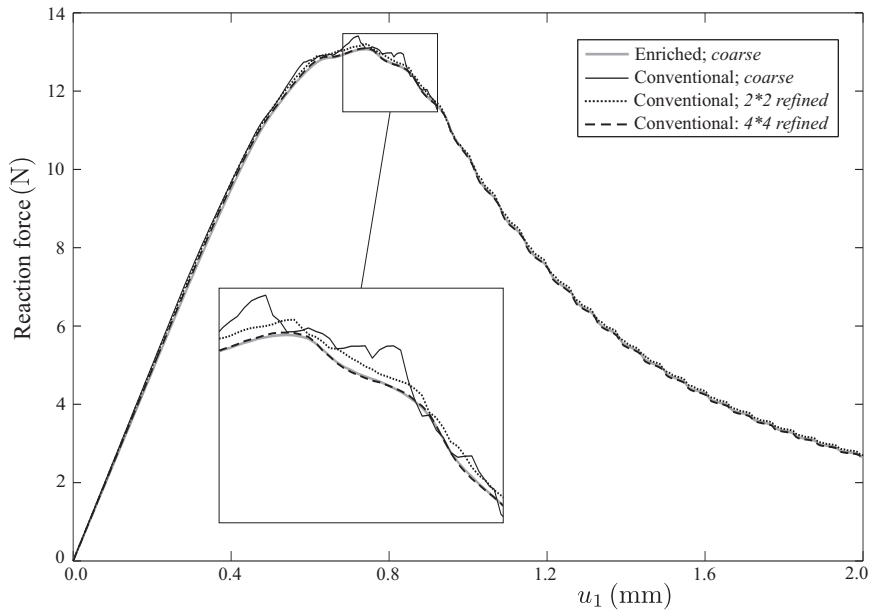


Figure 4.10: Force-displacement diagram of the three-dimensional peel-off problem with oblique delamination growth ($t_0 = 80$ MPa).

4.4 An alternative enrichment strategy

A robust self-adaptive finite element discretization should allow for an accurate approximation of a delamination front that is oblique with respect to the element edges. In other words, the same sharp kink in the separation profile of an oblique crack should be possible at any position in the element. Although the three-dimensional hierarchical self-adaptive finite element framework presented so far works reason-

ably well, it does not have this capability. Figure 4.11 clearly shows that a constant sharp crack front which is oblique with respect to the element edges cannot be obtained.

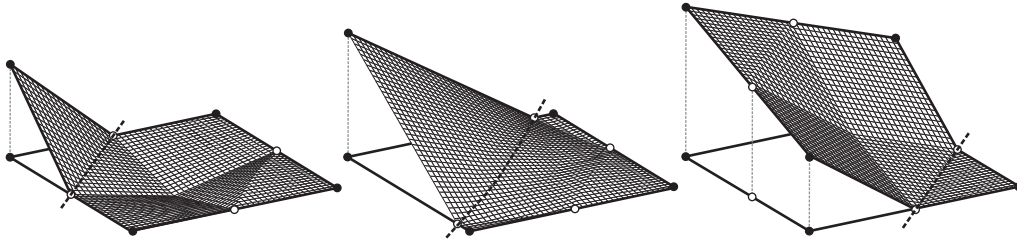


Figure 4.11: An oblique crack growth at different positions in a hierarchical enriched interface element (indicated by the dashed line).

An alternative, non-hierarchical, enrichment strategy which does not suffer from the limitations of the hierarchical framework, is presented. The non-hierarchical self-adaptive finite element framework is examined to evaluate its performance.

4.4.1 Non-hierarchical self-adaptive finite elements

In the non-hierarchical enrichment strategy, an additional adaptive node is added inside the enriched interface element (node m_5 in Figure 4.12). The position of this node is not an additional degree of freedom but is obtained from the intersection of lines m_1-m_3 and m_2-m_4 . The interfacial opening components at this node on the top and bottom surfaces of the interface element constitute extra degrees of freedom.

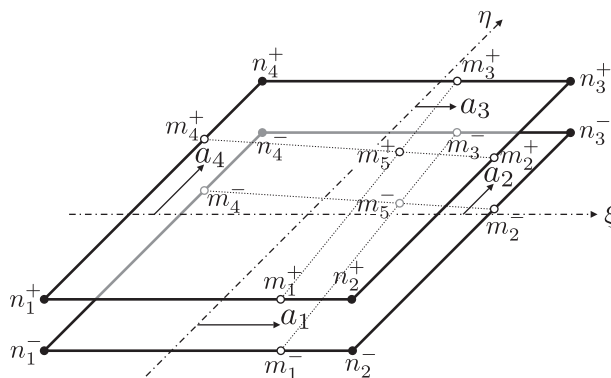


Figure 4.12: An eight-node self-adaptive interface element in isoparametric coordinates (non-hierarchical enrichment).

To address the expected geometry of the crack front inside an element, a new set of interpolation functions is defined as shown in Figure 4.13 for the adaptive nodes. To ensure that the partition of unity property of shape functions within an enriched

interface element is satisfied, the standard finite element interpolation functions associated with nodes n_1, \dots, n_4 are redefined so that their values depend on the position of the adaptive nodes (see Figure 4.14) as well. The interfacial separation is then recovered as follows:

$$\underline{u}^+ = \sum_{i=1}^4 N_i \underline{u}_i^+ + \sum_{j=1}^5 \phi_j(a_k | k = 1, \dots, 4) \underline{v}_j^+, \quad (4.22a)$$

$$\underline{u}^- = \sum_{i=1}^4 N_i \underline{u}_i^- + \sum_{j=1}^5 \phi_j(a_k | k = 1, \dots, 4) \underline{v}_j^-, \quad (4.22b)$$

$$\underline{\delta} = \underline{u}^+ - \underline{u}^- = \underline{B}_u \underline{u}_e, \quad (4.22c)$$

where $\underline{u}_i^{+/-}$ and $\underline{v}_j^{+/-}$ denote displacement components at the top and bottom surfaces of the i^{th} fixed node and the j^{th} adaptive node, respectively. The column \underline{u}_e collects all nodal displacement degrees of freedom of the enriched interface element. Displacement components at the adaptive nodes on the top and bottom surfaces of the interface element as well as the enrichment peak positions constitute additional degrees of freedom. Obviously, the bulk elements adjacent to the enriched interface elements have to be enriched accordingly.

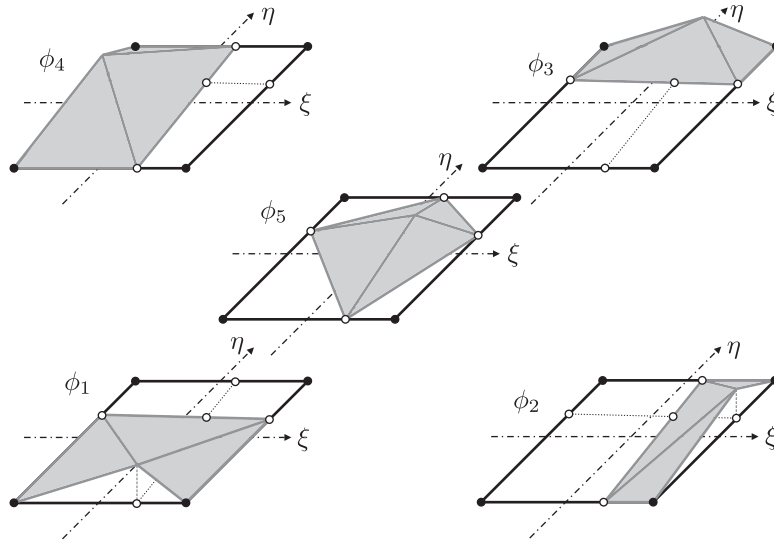


Figure 4.13: Finite element interpolation functions associated to the adaptive nodes in the non-hierarchical enrichment scheme.

Using the set of adaptive interpolation functions depicted in Figures 4.13 and 4.14, an oblique crack growth as schematically shown in Figure 4.15 can be modeled exactly. Moreover, Figure 4.15 shows that two sharp kink points can exist in a single interface element. A crack front aligned with element edges can also be captured by the alternative non-hierarchical enrichment scheme.

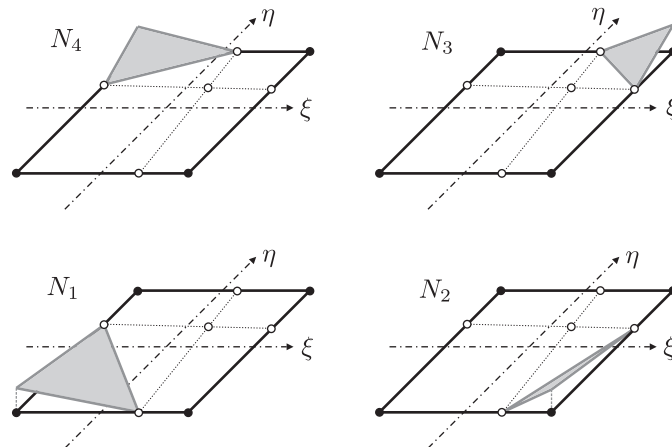


Figure 4.14: Finite element interpolation functions associated to the fixed nodes in the non-hierarchical enrichment scheme.

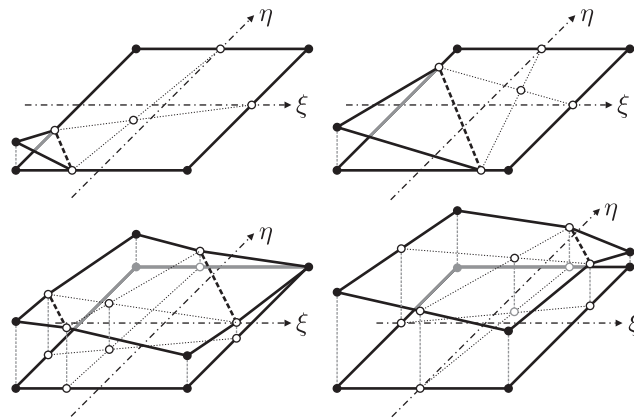


Figure 4.15: An oblique crack growth in a non-hierarchical enriched interface element; the sharp kinks growing from one upper corner of the enriched element are shown in the opening profiles by thick black dashed lines.

4.4.2 Simulation of a propagating oblique crack

The problem of Section 4.3.4 is revisited to evaluate the performance of the non-hierarchical enrichment strategy in the numerical simulation of a propagating delamination with an oblique front. As can be seen in Figure 4.16, both self-adaptive frameworks smoothen the global response of the most coarse mesh so that a standard Newton-Raphson iterative scheme becomes applicable.

The effectiveness of different refinement or adaptive strategies is evaluated using a quantitative measurement of the oscillations, see Section 4.3.3. Figure 4.17(a) confirms that increasing the brittleness leads to a more oscillatory response when the discretization is kept constant. The amplitude of the major oscillations also scale with brittleness as shown in Figure 4.17(b).

Although the non-hierarchical formulation does not suffer from the limitation re-

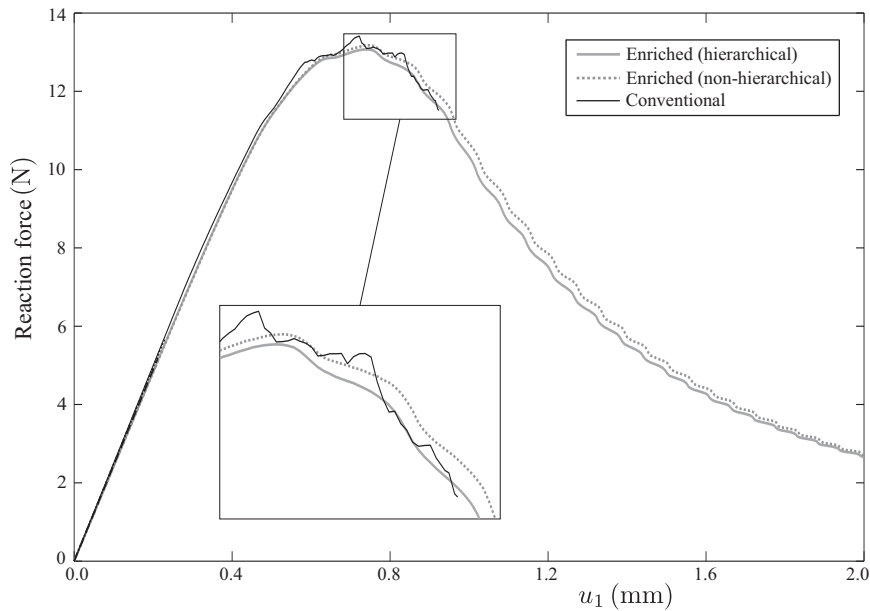


Figure 4.16: Force-displacement diagram for the oblique delamination growth in a three-dimensional peel-off problem using the coarse discretization ($t_0 = 80$ MPa).

ported for the hierarchical formulation, Figure 4.17 shows that it does not lead to a more smooth response. A more accurate approximation of the separation using conventional shape functions (bi-linear in this case) enriched by hierarchical extensions can be a reason for the better performance of the hierarchical framework compared to the non-hierarchical one which requires a modification of the standard finite element interpolation functions to piecewise planar functions. The approximation of the bending behavior of the structure is also deteriorated in the non-hierarchical self-adaptive framework (see load-displacement response in Figure 4.16). The results for an oblique delamination front show the effectiveness of the original hierarchical self-adaptive finite elements, surpassing the alternative enrichment or refinement strategies.

4.5 Conclusion and remarks

In this chapter, the self-adaptive cohesive zone formulation proposed in [106,109] for 2D problems, was extended to three-dimensional delamination problems. In the proposed formulation, the displacement approximation along all four edges of quadrilateral interface elements located in the fracture process zone was enriched by adding bi-linear functions with mobile peaks. The process-driven positions of these peaks were taken as additional degrees of freedom, for which a solution of the global system determines the values in an incremental-iterative routine. The kinematics of the self-adaptive cohesive zone elements and their adjacent bulk elements were elaborated and numerical and implementation issues were addressed.

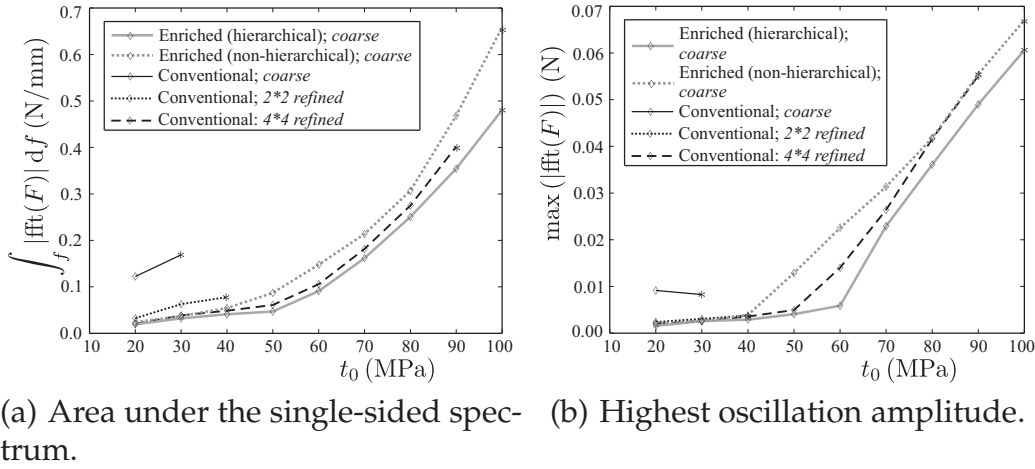


Figure 4.17: Error based on a discrete Fourier transform of the oscillatory response for a crack front oblique with respect to element edges (the data point shown by the asterisk * in each curve represents the most brittle level that can be solved by a standard Newton-Raphson scheme).

The performance of the proposed 3D self-adaptive finite element framework was first evaluated in a peel-off test with boundary conditions that imply a crack growth parallel to element edges. The interface constitutive behavior was described with a bilinear traction-separation law. The results show that the application of this methodology not only smoothens the global response considerably but also stabilizes the Newton-Raphson iterative procedure by reducing the non-physical oscillatory response so that a relatively brittle interfacial behavior can be captured.

The hierarchical enrichment was applied to the numerical simulation of propagating delamination with an oblique front with respect to element edges. Although the results show a considerable improvement of the global response, a constant crack front that grows in an oblique manner with respect to the element edges cannot be reproduced using a hierarchical enrichment. As an alternative, a non-hierarchical enrichment strategy was considered to enhance the approximation in the fracture process zone by adding a bubble function to the enriched element interpolation functions. The non-hierarchical scheme includes bi-linear enrichment of element edges as well. The necessity for the modification of the standard finite element interpolation functions of the fixed nodes and the introduction of extra degrees of freedom associated with an adaptive interior node constitute the main drawbacks of the non-hierarchical enrichment strategy. For the aforementioned reasons and considering the results obtained from both hierarchical and non-hierarchical enrichments in an oblique crack growth problem, the former seems to be more efficient.

The efficient application of cohesive zone models to engineering delamination problems is compromised by the very fine discretization required in the fracture process zone of brittle interfaces. Even though advanced computational strategies have been developed to tackle limit points such as snap-backs, a lot of computational effort is wasted on tracing the non-physical part of the solution path. The self-adaptive finite

elements developed by the authors open a new horizon in using 3D cohesive zone models in an effective, robust, and accurate manner at a reasonable computational cost.

A large deformation self-adaptive cohesive zone model¹

Abstract

Cohesive zone models are common tools for the simulation of delamination since two decades. However, application of these models in a quasi-static finite element framework requires a sufficiently fine discretization to resolve a quasi-brittle process zone. As an alternative to mesh refinement, an adaptive approximation of the growing delamination was obtained in earlier work by enriching the elements in the fracture process zone. Discretization-induced numerical instabilities are thereby avoided and a standard Newton-Raphson iterative scheme remains applicable. This enriched 2D cohesive zone model is here extended to a large deformation self-adaptive finite element framework, which makes it suitable for general engineering applications where geometrical and material non-linearities are expected. Based on recent experimental results from miniaturized mixed-mode bending tests, an irreversible mixed-mode traction-separation law is considered for the simulation of delamination over a wide range of mode mixities. The developed model is used for the simulation of mixed-mode bending tests on bi-material interfaces and the response is compared to the experimental results. Numerical simulations using coarse discretizations in a quasi-static finite element framework show the effectiveness of the self-adaptive cohesive zone model.

¹*Reproduced from:* M. Samimi, M. Kolluri, J.A.W. van Dommelen, and M.G.D Geers. Simulation of interlaminar damage in mixed-mode bending tests using large deformation self-adaptive cohesive zones. *In preparation.*

5.1 Introduction

Interfacial delamination is a common damage mechanism that may lead to failure in laminated structures especially when the interfacial strength is relatively low and a stress concentration occurs at the interface [7, 62]. In an attempt to avoid delamination which compromises the structural integrity, numerical predictive tools are necessary so that the risk for delamination initiation and growth can be assessed and the performance of the laminated structure be evaluated. Predictive simulations are required to avoid different experiments (if not impossible in case of complicated geometries) and to span all thermo-hygro-mechanical loading conditions that arise during the life-time of the structure.

Cohesive zone models were proposed based on the assumption that there exists a small zone around a crack tip where cohesive forces describe the material nonlinearities [10, 40, 58]. These models have also been used for the simulation of interfacial delamination in laminated structures [21, 25, 82, 112, 129]. In an interface cohesive zone model, the interfacial behavior is characterized by a traction-separation law, providing a phenomenological description of local degradation processes and softening occurring at the micro level. The fracture process zone is idealized as a line (or a plane in three dimensions) with initially a zero thickness [24]. Interface cohesive zone models combine stress-based and fracture mechanics-based approaches to simulate delamination growth as well as its initiation without a need for initial flaws [30, 62]. In order to account for the irreversibility of the delamination process, cohesive zone models have also been formulated in a damage mechanics framework [18, 20, 49, 59, 123].

The effect of mode-mixity on the mechanical response of an interface when subjected to arbitrary boundary conditions can be accounted for by a cohesive zone model [59, 127]. Identifying realistic values for the fracture toughness and the interfacial strength for the two main modes of opening as well as a suitable assumption for the coupling between normal and shear modes are crucial for the success of a cohesive zone model in predicting the behavior of a layered structure undergoing mixed-mode delamination. Experimental investigations on mixed-mode bending setups have shown that the interface fracture toughness varies considerably with the applied mode angle [70, 71]. Moreover, since the local mode angle is not known a priori, it is only through dedicated experiments that a prescribed local mode angle can be enforced by adjustment of the applied boundary conditions.

The widespread application of cohesive zone models is sometimes hindered by the need for a sufficiently fine discretization in the process zone of cohesive cracks to capture the steep stress gradient [33, 94]. Otherwise, the global structural response will be accompanied by a sequence of snap-backs for which a standard Newton-Raphson iterative scheme fails to converge. Complicated path-following techniques then have to be used to solve the non-linear system of equations resulting from quasi-static finite element analyses [4, 27, 45, 110]. Application of higher order interpolation functions or hierarchical enrichments of cohesive zone elements improve the perfor-

mance of cohesive zone models by reducing the discretization-induced oscillations due to a more accurate description of the kinematics in the process zone [28, 52, 119].

In the self-adaptive finite element framework that was recently proposed by the authors, the elements in the fracture process zone have been enriched to obtain an adaptive approximation of the growing delamination [106, 109]. A bi-linear enrichment function with an adaptive peak has been added to the linear interpolation along the elements located in the process zone of the interfacial crack. This enrichment naturally smoothens the global response of the structure, whereby the standard Newton-Raphson approach remains applicable for a coarse discretization. This adaptive scheme enforces the efficiency and robustness of brittle cohesive zone models to a great extent.

This paper aims to:

- extend the self-adaptive cohesive zone model to large deformations,
- make the enriched scheme applicable to a wide range of engineering problems where geometrical and material non-linearities are expected,
- account for the full mode mixity, coupling shear and normal interfacial modes,
- account for irreversibility at the interface,
- apply the enriched cohesive zone scheme to experimentally tested bi-material interfaces,
- address the parameter identification for the full range of mode mixities.

Comparison of the numerical results with those obtained from mixed-mode bending tests using a miniaturized setup reveals the suitability of the adopted constitutive law while showing the effectiveness of the self-adaptive framework in the simulation of delamination preserving a coarse discretization.

5.2 Interface model

One of the most common traction-separation laws that has been used for various applications in the last two decades, is the Xu-Needleman exponential law [138]. The model allows for a fracture toughness that is varying with the mode-mixity. It was shown by [127] that unrealistic results might be obtained under some circumstances. An improved model was proposed by modification of the coupling between normal and shear modes [69, 127]. In this paper, the improved exponential model is used in a large deformation damage mechanics framework.

The nominal traction components in the shear direction, which is defined along the interface mid-line denoted by the unit vector s , and in the direction normal to that,

denoted by the unit vector \mathbf{n} , are given by:

$$t_s = k_{0s} \delta_s (1 - d_s) (1 - d_{cn}), \quad (5.1a)$$

$$t_n = k_{0n} \langle \delta_n \rangle (1 - d_n) (1 - d_{cs}) - k_{0n} \langle -\delta_n \rangle. \quad (5.1b)$$

In the above equations, damage variables in shear and normal directions are denoted by d_s and d_n , respectively. The coupling damage terms, d_{cs} and d_{cn} , correspond to damage in normal and shear directions due to the maximum separation attained in shear and normal directions, $\delta_{s,max}$ and $\delta_{n,max}$, respectively. An unloading in shear or normal direction follows the secant stiffness to the origin of the traction-separation diagram in its associated mode (see Figure 5.1). Equation (5.1b) also implies that a linear elastic response with the virgin stiffness k_{0n} is considered in the normal compression regime due to the Macaulay brackets, $\langle \delta_n \rangle = (\delta_n + |\delta_n|)/2$. The virgin undamaged stiffnesses in shear and normal directions are defined as:

$$k_{0s} = G_{cs}/\delta_{0s}^2, \quad (5.2a)$$

$$k_{0n} = G_{cn}/\delta_{0n}^2, \quad (5.2b)$$

with G_{cs} and G_{cn} the fracture toughness in shear and normal directions which are equal to the area under the traction-separation curve in a pure mode II and pure mode I delamination process, respectively. As shown in the traction-separation curves of Figure 5.1, the maximum shear traction t_{0s} and the maximum normal traction t_{0n} are attained at characteristic separations δ_{0s} and δ_{0n} , respectively [69].

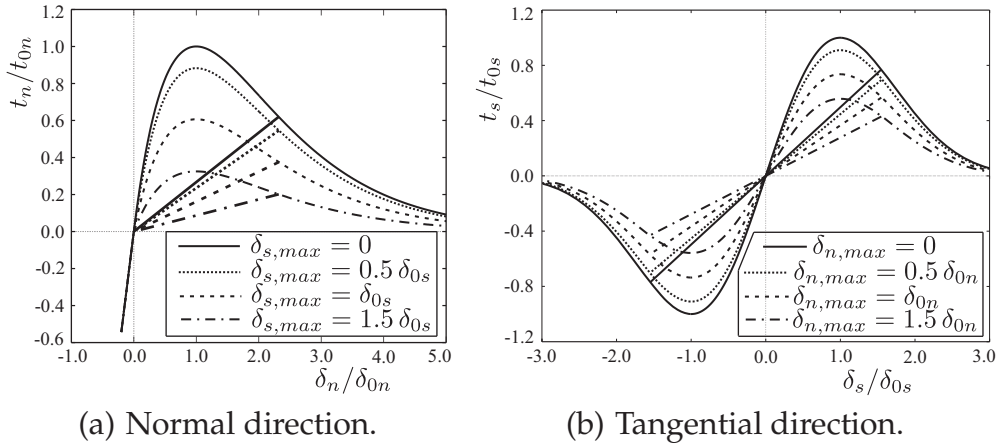


Figure 5.1: Irreversible mixed-mode traction-separation law.

This formulation incorporates the influence of accumulated damage in shear direction on the traction-separation behavior in the normal direction and vice versa due to the coupling damage variables (see Figure 5.1 for the reduction in interface strength in mode I or II due to the non-zero separation history value in the other delamination mode). The evolution of the damage variables introduced in Equation (5.1) is

governed by the following equations:

$$d_s = d_{cs} = 1 - \exp\left(-\frac{\delta_{s,max}^2}{2\delta_{0s}^2}\right), \quad (5.3a)$$

$$d_n = 1 - \exp\left(-\frac{\delta_{n,max}}{\delta_{0n}}\right), \quad (5.3b)$$

$$d_{cn} = 1 - \exp\left(-\frac{\delta_{n,max}}{\delta_{0n}}\right) \left(1 + \frac{\delta_{n,max}}{\delta_{0n}}\right). \quad (5.3c)$$

As implied by Equations (5.3), damage variables increase monotonically from 0 in the undamaged case but can never reach the value 1 which corresponds to the fully damaged case. In practice, this is not realistic. Therefore, it is assumed that the damage variables d_s and d_{cs} evolve linearly to 1 when the separation history parameter $\delta_{s,max}$ increases from $3\delta_{0s}$ to $4\delta_{0s}$. A similar strategy is applied to the evolution of d_n and d_{cn} when the separation history parameter $\delta_{n,max}$ increases from $6\delta_{0n}$ to $7\delta_{0n}$. The derivation of the interface tangent matrix is given in Section 5.6.

The interface model employed here consists of four independent parameters (G_{cs} , δ_{0s} , G_{cn} , δ_{0n}). The model parameters can be identified for different interfaces through experiments performed in a wide range of mode mixities [69]. The self-adaptive cohesive zone model is expected to be capable of predicting the resulting mixed-mode interfacial behavior by taking the identified model parameters in shear and normal modes into account.

5.3 Large deformation self-adaptive finite elements

Using self-adaptive cohesive zone elements, the linear separation approximation through the interface elements located in the fracture process zone is enriched with a bi-linear function with a mobile peak, with the peak position and the enrichment amplitudes as additional global degrees of freedom [106, 109]. The self-adaptive cohesive zone model is a robust and effective tool for the simulation of delamination initiation and growth, especially when the interfacial behavior is rather brittle [109]. In order to apply it successfully to a wide range of engineering applications, the formulation is next extended to a framework suitable for large deformations.

In this study, four-node linear interface elements with zero initial thickness have been used as depicted in Figure 5.2. The geometrical non-linearity is taken into account by casting the self-adaptive interface element into a two-dimensional corotational framework [95].

In the undeformed state, a local coordinate system with the orthonormal basis \mathbf{s}_0 - \mathbf{n}_0 is defined as shown in Figure 5.2(a). As deformation occurs, the local coordinate system with the orthonormal basis \mathbf{s} - \mathbf{n} is established such that the shear direction denoted by the unit vector \mathbf{s} is oriented along the element mid-line (line AB in Figure

5.2(b)) at an angle θ with the x-axis in the global Cartesian coordinate system x-y:

$$\underline{s} = [\cos \theta \quad \sin \theta]^T. \quad (5.4a)$$

$$\underline{n} = [-\sin \theta \quad \cos \theta]^T. \quad (5.4b)$$

Choosing the element mid-line (or mid-plane in a 3D configuration) as a basis for the orientation of the cohesive zone element is suitable for a large deformation framework as far as interface elements do not undergo a severe distortion accompanied by a very large rotation and translation of element faces with respect to each other [128]. The rotation matrix \underline{R} relating local and global coordinate systems is:

$$\underline{R}^T = \begin{bmatrix} \underline{s}^T \\ \underline{n}^T \end{bmatrix}, \quad (5.5)$$

such that

$$\hat{\underline{p}} = \underline{R}^T \underline{p}. \quad (5.6)$$

where the columns $\hat{\underline{p}}$ and \underline{p} collect the components of a vectorial field variable in local and global coordinate systems, respectively.

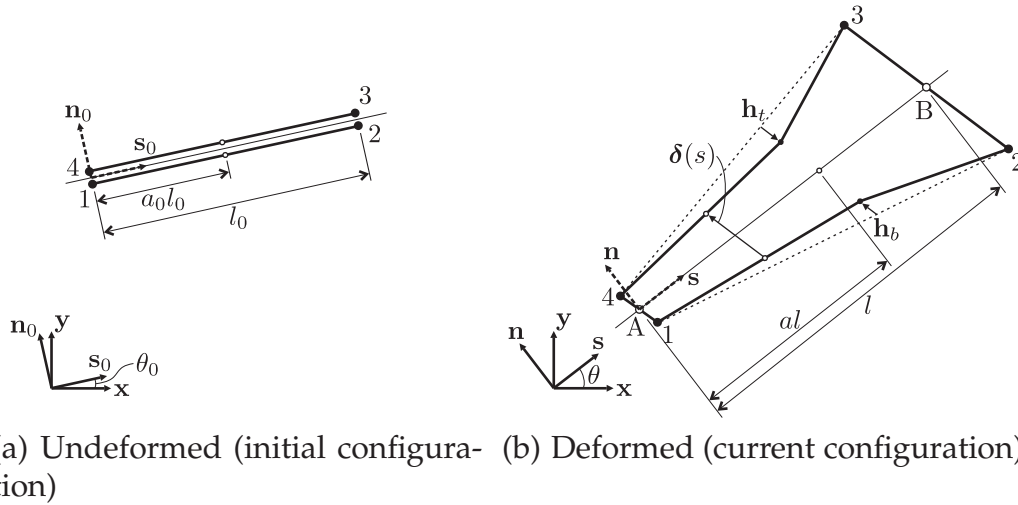


Figure 5.2: A four-node self-adaptive interface element in a two-dimensional geometrically non-linear setting.

A bi-linear function with an adaptive peak position a , defined in element isoparametric coordinates, is added to the standard linear interpolation functions. A self-adaptive interface element with a piece-wise linear separation approximation and an adaptive kink is retrieved (see Figure 5.2(b)). Using Equation (5.6), the values of nodal displacements and enrichment degrees of freedom are calculated in local

coordinates:

$$\hat{u}_i = \underline{R}^T u_i, \quad (5.7a)$$

$$\hat{h}_{t/b} = \underline{R}^T h_{t/b}, \quad (5.7b)$$

$$\hat{a} = a, \quad (5.7c)$$

with $\hat{h}_{t/b}$ the enrichment magnitudes at the top or bottom edges of the interface element. The separation in the current configuration can then be written in local coordinates as:

$$\hat{\underline{\delta}} = \underline{B}_u \hat{u} + \underline{B}_h(\hat{a}) \hat{h}, \quad (5.8)$$

with

$$\hat{u} = [u_{1,s} \quad u_{1,n} \quad u_{2,s} \quad u_{2,n} \quad u_{3,s} \quad u_{3,n} \quad u_{4,s} \quad u_{4,n}]^T, \quad (5.9a)$$

$$\hat{h} = [h_{b,s} \quad h_{b,n} \quad h_{t,s} \quad h_{t,n}]^T, \quad (5.9b)$$

where the details of \underline{B} -matrices and interpolation functions are given in [106].

The principle of virtual work is used to derive the equilibrium equations. It states that within a quasi-static framework, the internal virtual work δW_{int} done in an interface element with a domain Γ equals the external virtual work δW_{ext} applied to it (i.e. by neighboring elements):

$$\delta W_{int} = \int_{\Gamma_0} \delta \hat{\underline{\delta}}^T \hat{\underline{t}} d\Gamma_0 = \delta W_{ext}. \quad (5.10)$$

Using Equation (5.8), the left side of Equation 5.10 is written as:

$$\begin{aligned} \delta W_{int} &= \delta \hat{u}^T \int_{\Gamma_0} \underline{B}_u^T \hat{\underline{t}} d\Gamma_0 + \delta \hat{h}^T \int_{\Gamma_0} \underline{B}_h^T \hat{\underline{t}} d\Gamma_0 + \delta \hat{a} \int_{\Gamma_0} \underline{B}_a^T \hat{\underline{t}} d\Gamma_0 \\ &= \delta \hat{u}^T \hat{\underline{f}}_{int} + \delta \hat{h}^T \hat{\underline{g}}_{int} + \delta \hat{a} \hat{b}_{int}. \end{aligned} \quad (5.11)$$

Using Equation (5.7), the variation of vectorial fields in local and global coordinates are related through transformation matrices:

$$\delta \hat{u} = \underline{T}_{uu} \delta u, \quad (5.12a)$$

$$\delta \hat{h} = \underline{T}_{hu} \delta u + \underline{T}_{hh} \delta h, \quad (5.12b)$$

$$\delta \hat{a} = \delta a. \quad (5.12c)$$

The procedure to calculate the transformation matrices is detailed in Section 5.7. By substituting the variations of displacement and enrichment degrees of freedom from Equation (5.12) into Equation (5.11), the corresponding internal forces are expressed

in global coordinates:

$$\underline{f}_{int} = \underline{T}_{uu}^T \hat{\underline{f}}_{int} + \underline{T}_{hu}^T \hat{\underline{g}}_{int}, \quad (5.13a)$$

$$\underline{g}_{int} = \underline{T}_{hh}^T \hat{\underline{g}}_{int}, \quad (5.13b)$$

$$\underline{b}_{int} = \hat{\underline{b}}_{int}. \quad (5.13c)$$

Differentiating Equation (5.13) results in:

$$\delta \underline{f}_{int} = \underline{T}_{uu}^T \delta \hat{\underline{f}}_{int} + \underline{T}_{hu}^T \delta \hat{\underline{g}}_{int} + \delta \underline{T}_{uu}^T \hat{\underline{f}}_{int} + \delta \underline{T}_{hu}^T \hat{\underline{g}}_{int}, \quad (5.14a)$$

$$\delta \underline{g}_{int} = \underline{T}_{hh}^T \delta \hat{\underline{g}}_{int} + \delta \underline{T}_{hh}^T \hat{\underline{g}}_{int}, \quad (5.14b)$$

$$\delta \underline{b}_{int} = \delta \hat{\underline{b}}_{int}. \quad (5.14c)$$

The tangential stiffness matrix of the interface element required for the global non-linear solution procedure is then derived as follows:

$$\underline{K} = \begin{bmatrix} \underline{K}_{uu} & \underline{K}_{uh} & \underline{K}_{ua} \\ \underline{K}_{uh}^T & \underline{K}_{hh} & \underline{K}_{ha} \\ \underline{K}_{ua}^T & \underline{K}_{ha}^T & K_{aa} \end{bmatrix}, \quad (5.15a)$$

where:

$$\begin{aligned} \underline{K}_{uu} &= \frac{\partial \underline{f}_{int}}{\partial \underline{u}} \\ &= \underline{T}_{uu}^T \left(\hat{\underline{K}}_{uu} \underline{T}_{uu} + \hat{\underline{K}}_{uh} \underline{T}_{hu} \right) + \underline{T}_{hu}^T \left(\hat{\underline{K}}_{hu} \underline{T}_{uu} + \hat{\underline{K}}_{hh} \underline{T}_{hu} \right) \\ &\quad + \underline{K}_{uu}^\sigma + \underline{K}_{hu}^\sigma, \end{aligned} \quad (5.15b)$$

$$\underline{K}_{uh} = \frac{\partial \underline{f}_{int}}{\partial \underline{h}} = \left(\underline{T}_{uu}^T \hat{\underline{K}}_{uh} + \underline{T}_{hu}^T \hat{\underline{K}}_{hh} \right) \underline{T}_{hh} + \underline{K}_{hh}^\sigma, \quad (5.15c)$$

$$\underline{K}_{ua} = \frac{\partial \underline{f}_{int}}{\partial a} = \underline{T}_{uu}^T \hat{\underline{K}}_{ua} + \underline{T}_{hu}^T \hat{\underline{K}}_{ha}, \quad (5.15d)$$

$$\underline{K}_{hh} = \frac{\partial \underline{g}_{int}}{\partial \underline{h}} = \underline{T}_{hh}^T \hat{\underline{K}}_{hh} \underline{T}_{hh}, \quad (5.15e)$$

$$\underline{K}_{ha} = \frac{\partial \underline{g}_{int}}{\partial a} = \underline{T}_{hh}^T \hat{\underline{K}}_{ha}, \quad (5.15f)$$

$$K_{aa} = \frac{\partial \underline{b}_{int}}{\partial a} = \hat{K}_{ha}, \quad (5.15g)$$

with $\underline{K}_{uu}^\sigma$, $\underline{K}_{hu}^\sigma$, and $\underline{K}_{hh}^\sigma$ as the stress stiffness matrices derived from the variation of the transformation matrices, see Section 5.8 for more details [29, 95]. The interface tangential stiffness matrix is symmetric and the derivatives in local coordinates have been elaborated in [106]. A numerical integration scheme is used for calculation of

the stiffness matrix and internal force components with a relatively large number of fixed Gaussian integration points to capture the non-linear nature of the traction-separation law combined with the enriched kinematics [106].

The bulk is discretized using 4-node linear quadrilateral elements. A total Lagrange procedure is adopted to account for geometrical non-linearities. In the current model, an elastic constitutive equation is used that relates the second Piola-Kirchhoff stress to the Green-Lagrange strain measure. However, the developed framework allows for other constitutive models (e.g. elasto-plastic). The bulk elements neighboring an enriched cohesive zone element are enriched as well in a manner as explained in [106].

5.4 Miniaturized mixed-mode bending test

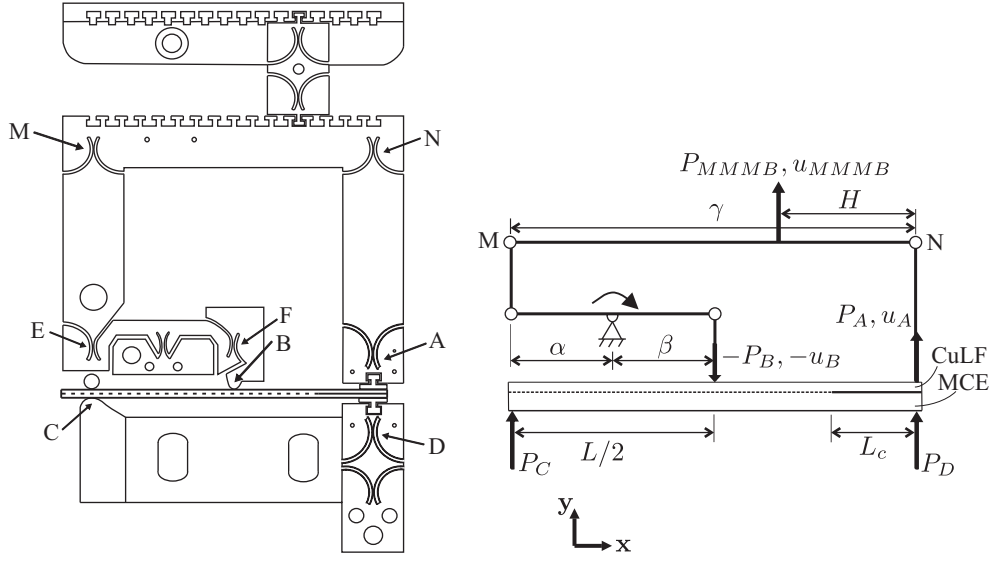
Combining a double cantilever beam concept for mode I loading and an end-notch flexure concept for mode II loading, a mixed-mode bending test has been developed where changing the load position on a loading lever determines the ratio of mode I to mode II loading at the delamination front [99]. The fracture toughness can then be measured for a wide range of mode mixities using identical test specimens and procedures. The mixed-mode bending concept has been widely used after being standardized [1].

Inspired by the need to characterize the interfacial behavior of multi-layer structures present in microsystems, a miniaturized mixed-mode bending (MMMB) apparatus (see Figure 5.3(a)) which can fit in a scanning electron microscope chamber for in-situ delamination testing, has been designed in [70,71]. The setup allows for a pure mode II loading while a compressive mode I component is avoided at the delamination front. This feature increases the accuracy of the fracture toughness measurements when a considerable amount of mode II loading is present at the growing crack tip.

A displacement u_{MMMB} in the y -direction is prescribed to the beam MN at a distance $H = \varsigma\gamma$ from point N. The dimensionless parameter ς determines the mode angle at the delamination front. While $\varsigma = 0$ resembles a double cantilever beam test (pure mode I delamination), increasing the parameter ς results in a larger mode II component so that a pure mode II delamination can eventually be realized. For samples with unequal layers, the relation between the relative loading position and the mode angle can be found in [70]).

For the simulation of delamination in [71], the whole setup and the sample have been discretized with finite elements and the corresponding boundary conditions have been applied on the whole geometry; see Figure 5.4.

To avoid modeling the entire setup, a constraint equation will be used instead here. For this purpose, some verified assumptions can be made; first, the rotation of the links in the setup is small and second, the deformations in the segments BF, EF, EM, AN, and MN are negligible. Both the aforementioned assumptions are realistic [71].



(a) The setup design after [70]. (b) Schematic representation of the setup.

Figure 5.3: Miniaturized mixed-mode bending test.

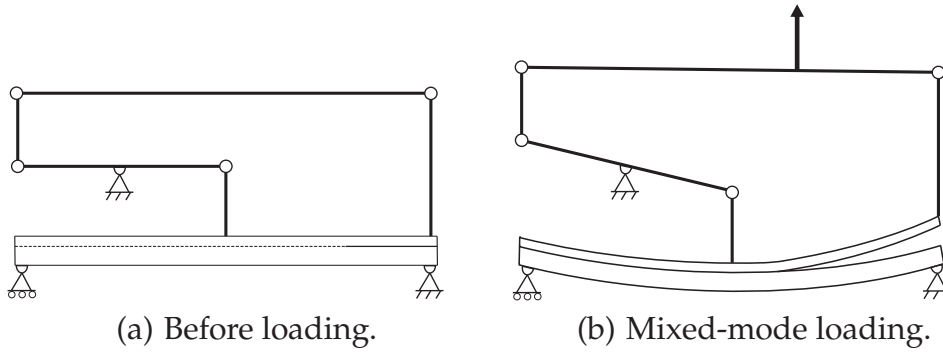


Figure 5.4: Schematic representation of delamination experiments by the miniaturized mixed-mode bending apparatus.

Moreover, the rotational stiffness of the elastic hinges at points E, F, M, and N is ignored due to the negligible contribution of the energy stored in the elastic hinges. Based on these assumptions, the following holds:

$$u_{A,y} = u_{N,y}, \quad (5.16a)$$

$$u_{B,y} = u_{F,y}, \quad (5.16b)$$

$$u_{E,y} = u_{M,y} = -\frac{\alpha}{\beta} u_{F,y}, \quad (5.16c)$$

The constraint equation can then be written as:

$$u_{A,y} = \frac{1}{1-\varsigma} u_{MMMMB,y} + \frac{\varsigma}{1-\varsigma} \frac{\alpha}{\beta} u_{B,y}, \quad (5.17)$$

where u_{MMMMB} is the displacement prescribed on the setup (see Figure 5.3). As a result of the constraint equation, the forces applied to the sample can be written as:

$$P_A = P_{MMMMB} (1 - \varsigma), \quad (5.18a)$$

$$P_B = -P_{MMMMB} \frac{\alpha}{\beta} \varsigma. \quad (5.18b)$$

The boundary conditions are applied to the sample as shown in Figure 5.3(b), together with the constraint Equation (5.17). The delamination simulation is carried out on bi-material specimens consisting of copper lead frame (CuLF) and molding compound epoxy (MCE). The layers of the bi-material samples were 30 mm long and 5 mm wide with a thickness of 0.2 mm for the CuLF layer and 0.5 mm for the MCE layer [70].

The constitutive law of MCE is linear elastic while CuLF is an elasto-plastic material. However, the experimental results did not reveal a plastic deformation either in the bulk or at the interface for samples of this thickness [70]. Therefore, the behavior of the CuLF layer is also assumed to be linear elastic. The elastic bulk material properties are shown in Table 5.1.

Table 5.1: Bulk material properties.

	Young's modulus E (GPa)	Poisson's ratio ν
CuLF	120	0.33
MCE	30	0.25

Delamination experiments were performed on pre-cracked samples (see Figure 5.3(b)) over a wide range of mode mixities characterized by different values of ς [70]. In order to attain a sharp steady state microscopic crack tip, a loading-unloading cycle in pure mode I was applied to the bi-material sample in experiments performed under different loading conditions ($\varsigma = 0.0, 0.4, 0.67, 0.8$) and the crack tip position was measured at the onset of the first unloading [70]. To avoid the influence of the pre-crack, the experimental results shown in Figure 5.6 do not include the initial loading-unloading cycle. The measured crack length is then used as the pre-crack (L_c) for the simulation of delamination in bi-material samples. The fracture toughness in shear and normal directions are directly calculated from the whole set of experimental results in different mode ratios by determining the energy required to create cracks in mode I, and mixed-mode loading conditions [70]. Other required model parameters are chosen such that the second experimental loading-unloading

loop in mode I (see Figure 5.5(a)) and mode II dominant (see Figure 5.5(d)) loading conditions are reproduced with a reasonable accuracy. The resulting cohesive zone model parameters used in the simulations are shown in Table 5.2.

Table 5.2: Cohesive zone model parameters.

	G_c (N/m)	δ_0 (μm)	t_0 (MPa)
mode I	5.0	0.2	9.2
mode II	32.0	5.0	3.9

The bi-material sample layers are discretized by four-node quadrilateral plane strain elements. Each layer is discretized by 240×4 elements in the x - y plane. This level of refinement gives a sufficiently accurate approximation of the bending behavior of the bi-layer sample during delamination experiments. A pre-crack of length L_c is assumed at the right side of the sample between the layers as shown in Figure 5.3(b). Linear interface elements are placed between CuLF and MCE layers where they are bonded. Initially, all elements are non-enriched and enrichment is adaptively activated in elements within the fracture process zone throughout the deformation [109]. Numerical simulations are performed for four different values of ζ indicating conditions of mode I ($\zeta = 0.00$) and mixed-mode loading ($\zeta = 0.40, 0.67, 0.80$). The results are shown in Figure 5.6 along with experimentally obtained results. Oscillations can be seen in the global load-displacement response of the structures simulated within the conventional cohesive zone modeling framework for all loading conditions. In contrary to the self-adaptive cohesive zone model, the conventional model fails to converge prematurely in some cases due to the occurrence of snap-backs that cannot be traced with the standard Newton-Raphson iterative procedure employed here (see Figures 5.5(c) and 5.5(d)). Application of the self-adaptive cohesive zone model results in smooth global responses for all mode mixities.

In general, there is a reasonable agreement between experimental and numerical results, especially in predicting the prescribed displacement at which an interfacial crack starts to grow upon reloading (ignoring the first experimental loading-unloading cycle aimed only at creation of a sharp crack tip). It shows the capability of the cohesive zone model used here in estimating the load bearing capacity of the structure. However, more deviations can be observed for larger delamination lengths. The wavy pattern of the experimental load-displacement responses after the initiation of delamination for the mode II dominant experiments can be attributed to friction in the small cracked zone behind the process zone (the rough bi-material crack surfaces were shown in SEM micrographs in [70]). Various aspects of both experiments and simulations should be investigated to address the source of the observed difference between experimental results and simulations. For example, non-linearity of the setup and friction at the fixtures of the setup affect the experimental results. On the other hand, considering complex failure mechanisms within the interface of an MCE-CuLF assembly of which the effects have to be lumped in a cohesive zone, the considered traction-separation law may be inadequate to de-

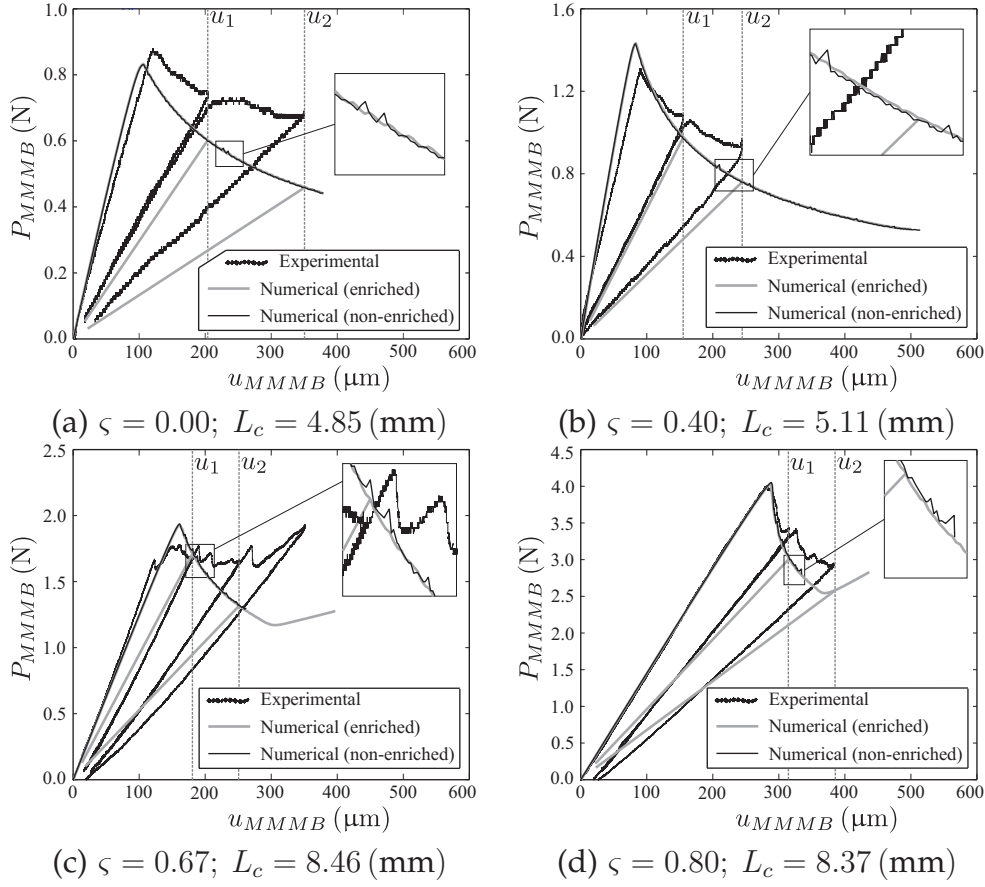


Figure 5.5: Force-displacement diagrams of the delaminating bi-material sample for a wide range of mode mixities; experimental and numerical results are obtained from the miniaturized mixed-mode bending tests and the self-adaptive and conventional cohesive zone models, respectively.

scribe the delamination failure due to its fixed shape. A more thorough analysis of delamination growth is next performed.

In the experimental approach, the crack tip is monitored at two different loading levels; for example at u_1 and u_2 in Figures 5.5(a) to 5.5(d). In any global loading condition denoted by ζ , the energy dissipated through the delamination process is used to calculate the energy release rate corresponding to that loading condition. The same strategy is followed in the simulations where the crack growth is measured within a loading-unloading cycle bounded by u_1 and u_2 . The numerical crack tip is defined as the traction-free point just behind the cohesive zone. Figures 5.6(a) to 5.6(d) show the crack length during delamination growth under various loading conditions using the self-adaptive cohesive zone model. Experimental and numerical crack tip positions, a^{exp} and a^{num} , are pinpointed in Figures 5.6(a) to 5.6(d). The definition of the crack tip position in the experiments differs from the numerical definition. Moreover, there is always an uncertainty associated with identification of the crack tip position in experiments [71]. As a result, the experimental and numerical crack tip position at u_1 and u_2 loading levels do not coincide. However, the numerical approximation

for the crack segment created in the considered loading range, i.e. the increase in crack length between u_1 and u_2 , matches reasonably well with the experimental observations. The energy dissipated within the delamination process between u_1 and u_2 and the corresponding increase in crack length are used to calculate the fracture toughness for both experiments and simulations.

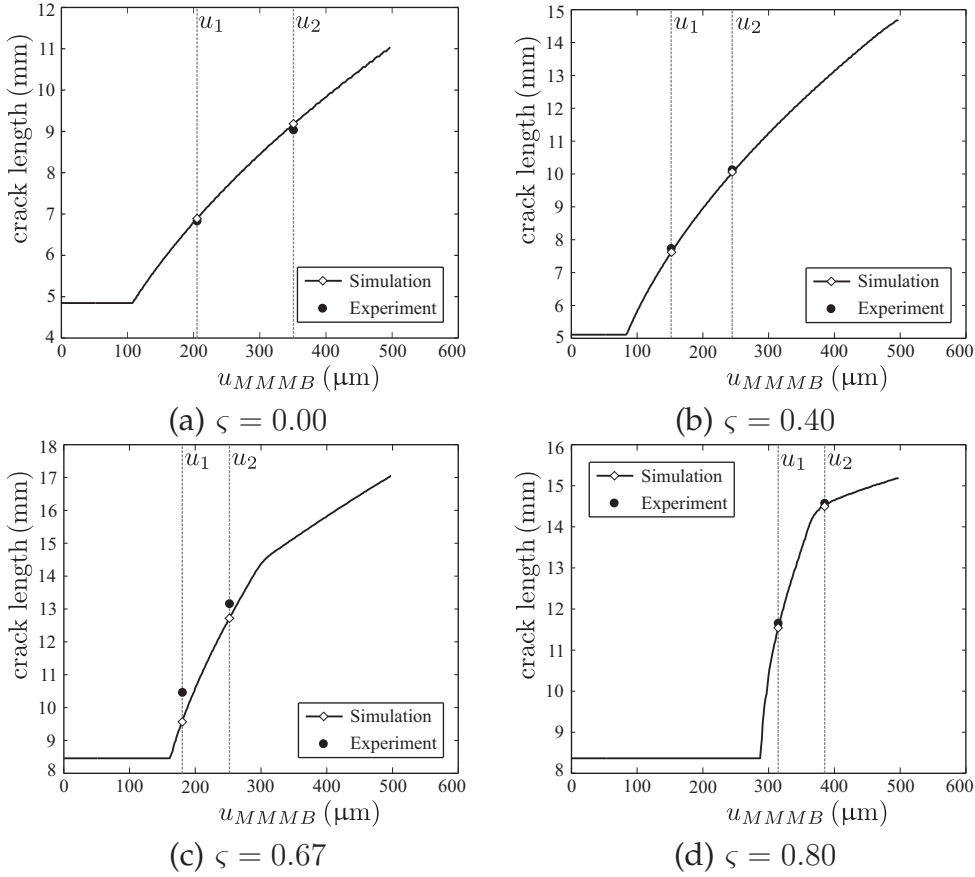


Figure 5.6: Comparison of delamination growth predicted using the self-adaptive cohesive zone model with experiments (symbols \bullet and \diamond represent experimental and numerical points for the specified prescribed displacements, respectively).

The variation of the mode angle at the crack tip upon delamination growth is shown in Figure 5.7 where the following equation is used to calculate the mode angle at the crack tip:

$$\Psi = \arctan\left(\frac{\delta_s}{\delta_n}\right), \quad (5.19)$$

where δ_s and δ_n denote the shear and normal separation components at the numerical crack tip, respectively. Analyses of the mode angle at the crack tip in all numerical simulations show that loading at a fixed value of ζ does not result in a delamination

growth under a constant mode angle. Although the variation of mode angle at the crack tip is limited (from a minimum of 0.2° for $\zeta = 0.0$ to a maximum of 6.0° for $\zeta = 0.67$), the mode angle does not remain constant upon crack propagation in an MMMB delamination experiment, especially in mixed-mode loading conditions.

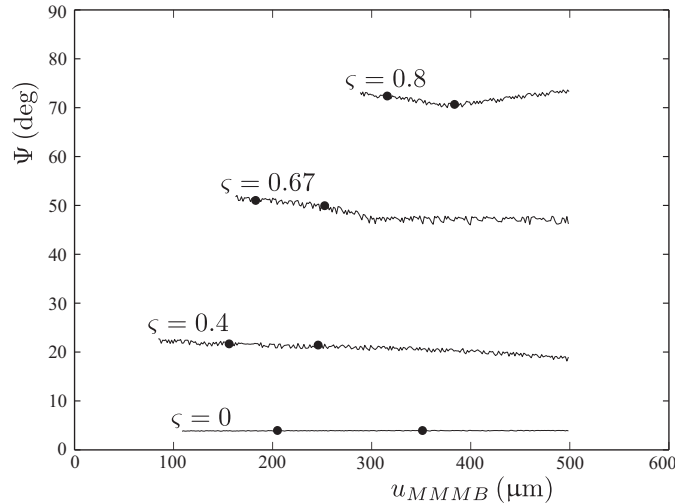


Figure 5.7: Variation of the mode angle at the crack tip obtained from self-adaptive cohesive zone model simulations. The markers • indicate the moments of unloading u_1 and u_2 .

For all loading conditions shown in Figure 5.6, the fracture toughness is calculated based on the numerical simulations and the results are compared with experimental data reported in [70] (see Figure 5.8). For the numerical approach, the fracture toughness is calculated within the interval of $[u_1, u_2]$ as indicated in Figures 5.6(a) to 5.6(d).

In general, numerical and experimental results follow a similar trend in Figure 5.8 which shows that the numerical model is capable of predicting the variation of fracture toughness with respect to various mode mixities implied by the global loading position ζ . The experimental data of Figure 5.8 shows a high sensitivity of the fracture toughness to the loading position in mode II dominant conditions for which only three sets of experiments have been performed (see [70] for more details). It is not sufficient especially since strong variations occur in this range. More experimental data for mode II dominant conditions will provide a more accurate description of the variation of fracture toughness with respect to mode mixity. This variation is a consequence of different mechanisms resisting delamination growth at the micro-scale within the process zone.

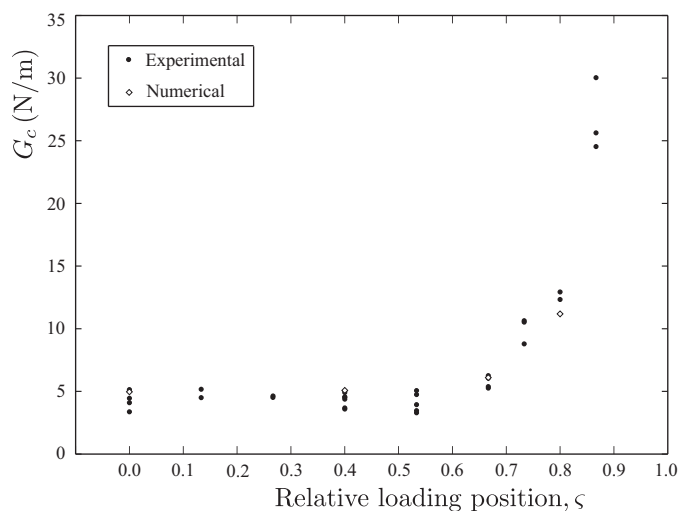


Figure 5.8: Critical energy release rate (fracture toughness) as a function of mode mixity.

5.5 Discussion and conclusion

In this paper, the two-dimensional self-adaptive cohesive zone model developed in [106,109] was extended to a large deformation framework. Based on experimental observations, a mixed-mode irreversible constitutive law was used for the cohesive zone model. The model accounts for the full mode mixity and a coupling between delamination modes. The numerical model developed here can be used for a wide range of engineering applications where material and geometrical non-linearities are expected to occur in delamination problems. Although the current bulk material model is linear elastic, the developed large deformation framework allows for using non-linear material models as well. The cohesive zone model parameters were identified based on the experimental results on mixed-mode delamination in bi-material specimens.

Mixed-mode delamination in bi-material samples (copper lead frame and molding compound epoxy) was simulated using the developed methodology. In order to obtain a fair comparison between numerical and experimental results, a sufficiently fine discretization was applied to capture the bending behavior of the specimens with an adequate accuracy. However, the global response of the structure was found to be oscillatory using the conventional cohesive zone model. A standard Newton-Raphson iterative scheme failed to converge in some cases, especially in mode II dominant simulations, where the conventional cohesive zone model had been applied. The effectiveness of the self-adaptive finite element strategy on smoothing the global response of the system under different loading conditions was demonstrated. A standard Newton-Raphson iterative scheme was used without a need for path-following techniques or further mesh refinements.

The numerical results were compared to experimental results obtained from delamination tests for different loading conditions ranging from mode I to mode II domi-

nant cases using a miniaturized mixed-mode bending setup. The numerical model could predict the trend of the structural response with a reasonable accuracy; however, a deviation was observed in the prediction of delamination growth. In this regime, the non-linearity of the setup as well as the friction at the setup fixtures and their effect on the experimental load-displacement response in various mode mixities need to be investigated. On the numerical side, the traction-separation law used here has a fixed shape which may induce some limitations for simulating complex failure mechanisms happening at the interface between metal (CuLF) and a polymer (MCE). An investigation of mixed-mode simulations was carried out which revealed the capability of the model in approximating the energy dissipation throughout delamination for different mode mixities. A variation of the mode angle at the crack tip was observed for a fixed global loading position. The latter has to be taken into account in characterization of the interface based on mixed-mode experiments.

The current experimental data on delamination of CuLF-MCE specimens in mode II dominant conditions using the miniaturized mixed-mode bending apparatus is not sufficient for a full coverage of the interfacial behavior with respect to mode mixity. More mixed-mode experiments with sharp crack tips introduced along the interface are required, especially for high mode angles. Moreover, a better understanding of the dissipation mechanisms at the micro-scale within the cohesive zone is required. It can be investigated through in-situ experiments to characterize the interface while from a numerical perspective, a multi-scale approach would be important to obtain a better understanding of interfacial delamination and the origin of interfacial properties.

5.6 Appendix A: Interface tangent matrix

The interface tangent matrix shows the variation of traction ($\underline{t} = [t_s \ t_n]^T$) with respect to separation ($\underline{\delta} = [\delta_s \ \delta_n]^T$) within the interface:

$$d\underline{t} = \underline{H}_{cz} d\underline{\delta}. \quad (5.20)$$

The damage variables introduced in Equation (5.3) are collected in:

$$\underline{D} = [d_s \ d_{cs} \ d_n \ d_{cn}]^T. \quad (5.21)$$

The cohesive zone tangent matrix, \underline{H}_{cz} , is then derived as follows:

$$\underline{H}_{cz} = \frac{\partial \underline{t}}{\partial \underline{\delta}} \Big|_{\underline{D}} + \frac{\partial \underline{t}}{\partial \underline{D}} \Big|_{\underline{\delta}} \frac{\partial \underline{D}}{\partial \underline{\delta}}, \quad (5.22a)$$

with

$$\begin{aligned} \frac{\partial \underline{t}}{\partial \underline{\delta}} \Big|_{\underline{D}} &= \begin{bmatrix} \partial t_s / \partial \delta_s & \partial t_s / \partial \delta_n \\ \partial t_n / \partial \delta_s & \partial t_n / \partial \delta_n \end{bmatrix} \\ &= \begin{bmatrix} k_{0s}(1-d_s)(1-d_{cn}) & 0 \\ 0 & k_{0n}(1-d_n)(1-d_{cs})\mathcal{H}(\delta_n) + k_{0n}\mathcal{H}(-\delta_n) \end{bmatrix}, \end{aligned} \quad (5.22b)$$

$$\begin{aligned} \frac{\partial \underline{t}}{\partial \underline{D}} \Big|_{\underline{\delta}} &= \begin{bmatrix} \partial t_s / \partial d_s & \partial t_s / \partial d_{cs} & \partial t_s / \partial d_n & \partial t_s / \partial d_{cn} \\ \partial t_n / \partial d_s & \partial t_n / \partial d_{cs} & \partial t_n / \partial d_n & \partial t_n / \partial d_{cn} \end{bmatrix} \\ &= \begin{bmatrix} -k_{0s}\delta_s(1-d_{cn}) & 0 & 0 & -k_{0s}\delta_s(1-d_s) \\ 0 & -k_{0n}\langle \delta_n \rangle(1-d_n) & -k_{0n}\langle \delta_n \rangle(1-d_{cs}) & 0 \end{bmatrix}, \end{aligned} \quad (5.22c)$$

$$\frac{\partial \underline{D}}{\partial \underline{\delta}} = \begin{bmatrix} \partial d_s / \partial \delta_s & \partial d_s / \partial \delta_n \\ \partial d_{cs} / \partial \delta_s & \partial d_{cs} / \partial \delta_n \\ \partial d_n / \partial \delta_s & \partial d_n / \partial \delta_n \\ \partial d_{cn} / \partial \delta_s & \partial d_{cn} / \partial \delta_n \end{bmatrix} = \begin{bmatrix} \mathcal{F}_s \frac{\delta_s}{\delta_{0s}^2} \exp\left(-\frac{\delta_s^2}{2\delta_{0s}^2}\right) & 0 \\ \mathcal{F}_s \frac{\delta_s}{\delta_{0s}^2} \exp\left(-\frac{\delta_s^2}{2\delta_{0s}^2}\right) & 0 \\ 0 & \mathcal{F}_n \frac{1}{\delta_{0n}} \exp\left(-\frac{\delta_n}{\delta_{0n}}\right) \\ 0 & \mathcal{F}_n \frac{\delta_n}{\delta_{0n}^2} \exp\left(-\frac{\delta_n}{\delta_{0n}}\right) \end{bmatrix}, \quad (5.22d)$$

where \mathcal{H} is the Heaviside function. The Equation (5.22d) shows the variation of the damage parameters with respect to separation components in the exponential damage evolution regime indicated by Equations (5.3a) to (5.3c). The linear tail of the damage evolution law is treated accordingly (see Section 5.2 for the explanation on damage evolution). The load function \mathcal{F}_s gets a value of 1 upon loading in the shear direction and 0 otherwise. The load function \mathcal{F}_n equals 1 upon loading in normal direction and 0 otherwise. The loading in shear and normal directions occurs if the

following conditions are met:

$$\frac{d|\delta_s|}{d\tau} > 0 \text{ and } |\delta_s| = \delta_{s,max} \Rightarrow \mathcal{F}_s = 1, \quad (5.23a)$$

$$\frac{d\delta_n}{d\tau} > 0 \text{ and } \delta_n = \delta_{n,max} \Rightarrow \mathcal{F}_n = 1. \quad (5.23b)$$

5.7 Appendix B: Transformation matrices

The transformation matrices, \underline{T}_{uu} , \underline{T}_{hu} , and \underline{T}_{hh} , are derived using a procedure similar to the one used in [95]. However, the local orthonormal basis s-n is defined with respect to the interface element mid-line in the current study and is more suitable for a large deformation formulation [128], whereas the formulation elaborated in [95] is based on the interface bottom-edge as the reference.

Differentiating Equation (5.7a) results in:

$$\delta \hat{u}_i = \underline{R}^T \delta u_i + \delta \underline{R}^T u_i, \quad (5.24)$$

in which the variation of the rotation matrix - defined in Equation (5.5) - reads:

$$\delta \underline{R} = \begin{bmatrix} -\sin \theta & -\cos \theta \\ \cos \theta & -\sin \theta \end{bmatrix} \delta \theta. \quad (5.25)$$

To determine $\delta \theta$, the displacement of point B with respect to point A in local coordinates is written as (see Figure 5.2):

$$\begin{aligned} \hat{u}_{BA} &= \hat{u}_B - \hat{u}_A = \hat{x}_B - \hat{x}_{0B} - (\hat{x}_A - \hat{x}_{0A}) \\ &= \underline{R}^T (x_B - x_A) - (\hat{x}_{0B} - \hat{x}_{0A}) = \underline{R}^T x_{BA} - \hat{x}_{0BA}, \end{aligned} \quad (5.26)$$

where \hat{x}_{0i} and \hat{x}_i collect initial and current local coordinates of point i , respectively and x_i collects the current global coordinates of point i . Since line AB is the element mid-line and this is taken as a basis for the local coordinate system, the normal component of \hat{u}_{BA} is zero:

$$\hat{u}_{BA,n} = \underline{n}^T x_{BA} - \hat{x}_{0BA,n} = 0, \quad (5.27)$$

Differentiating Equation (5.27) results in:

$$\delta \hat{u}_{BA,n} = -\underline{s}^T x_{BA} \delta \theta + \underline{n}^T \delta x_{BA} = 0. \quad (5.28)$$

Since δx_{BA} is zero, $\delta \theta$ is then calculated:

$$\delta \theta = (\underline{n}^T \delta u_{BA}) / l, \quad (5.29)$$

where l denotes the current length of the interface element and δu_{BA} is elaborated as follows:

$$\delta u_{BA} = \delta u_B - \delta u_A = \frac{1}{2}(-\delta u_1 + \delta u_2 + \delta u_3 - \delta u_4), \quad (5.30)$$

Substitution of Equation (5.30) into Equation (5.29) leads to:

$$\delta \theta = \underline{v}^T \delta \underline{u}, \quad (5.31a)$$

where

$$\underline{v} = \frac{1}{2l} \left[\sin \theta \quad -\cos \theta \quad -\sin \theta \quad \cos \theta \quad -\sin \theta \quad \cos \theta \quad \sin \theta \quad -\cos \theta \right]^T, \quad (5.31b)$$

$$\delta \underline{u} = \left[\delta u_{1,x} \quad \delta u_{1,y} \quad \delta u_{2,x} \quad \delta u_{2,y} \quad \delta u_{3,x} \quad \delta u_{3,y} \quad \delta u_{4,x} \quad \delta u_{4,y} \right]^T, \quad (5.31c)$$

Substitution of Equation (5.31a) into Equation (5.25) results in calculation of $\delta \underline{R}$ which can be used in Equation (5.24) to give the variation of displacements of node i in local coordinates with respect to global coordinates as:

$$\delta \hat{u}_i = \underline{R}^T \delta u_i + \hat{u}_i \underline{v}^T \delta \underline{u}, \quad (5.32)$$

where $\hat{u}_i = [u_{i,n} \quad -u_{i,s}]^T$. Taking all nodal displacements into account, the transformation matrix \underline{T}_{uu} used in Equation (5.12a), is given by:

$$\underline{T}_{uu} = \begin{bmatrix} \underline{R}^T & \underline{0} & \underline{0} & \underline{0} \\ \underline{0} & \underline{R}^T & \underline{0} & \underline{0} \\ \underline{0} & \underline{0} & \underline{R}^T & \underline{0} \\ \underline{0} & \underline{0} & \underline{0} & \underline{R}^T \end{bmatrix} + \hat{u} \underline{v}^T, \quad (5.33a)$$

with

$$\hat{u} = \left[u_{1,n} \quad -u_{1,s} \quad u_{2,n} \quad -u_{2,s} \quad u_{3,n} \quad -u_{3,s} \quad u_{4,n} \quad -u_{4,s} \right]^T, \quad (5.33b)$$

The next step is to determine the transformation matrices \underline{T}_{hu} and \underline{T}_{hh} . Similar to the approach that was used for the derivation of \underline{T}_{uu} , a differentiation of Equation (5.7b) is carried out:

$$\delta \hat{h}_{t/b} = \underline{R}^T \delta h_{t/b} + \delta \underline{R}^T h_{t/b}. \quad (5.34)$$

Using Equations (5.31a) and (5.25), the above relation can be written as:

$$\delta \hat{h}_{t/b} = \underline{R}^T \delta h_{t/b} + \hat{h}_{t/b} \underline{v}^T \delta \underline{u}, \quad (5.35)$$

where $\hat{h}_{t/b} = [\hat{h}_{t/b,n} \quad -\hat{h}_{t/b,s}]^T$. The transformation matrices \underline{T}_{hu} and \underline{T}_{hh} used in Equa-

tion (5.12b), are then given by:

$$\underline{T}_{hu} = \hat{h} v^T, \quad (5.36a)$$

$$\underline{T}_{hh} = \begin{bmatrix} \underline{R}^T & \underline{0} \\ \underline{0} & \underline{R}^T \end{bmatrix}, \quad (5.36b)$$

with

$$\hat{h} = [h_{b,n} \quad -h_{b,s} \quad h_{t,n} \quad -h_{t,s}]^T. \quad (5.36c)$$

5.8 Appendix C: Stress stiffness matrices

Considering Equations (5.14a) and (5.15b), the stress stiffness matrix $\underline{K}_{uu}^\sigma$ is defined so that:

$$\delta \underline{T}_{uu}^T \hat{f}_{int} = \sum_{i=1}^8 \left(\delta \underline{T}_{uu}^{(i)} \right)^T \hat{f}_{int}^{(i)} = \sum_{i=1}^8 \hat{f}_{int}^{(i)} \underline{G}_{uu}^{(i)} \delta u = \underline{K}_{uu}^\sigma \delta u, \quad (5.37)$$

where $\delta \underline{T}_{uu}^{(i)}$ denotes the i th row of $\delta \underline{T}_{uu}$ and $\hat{f}_{int}^{(i)}$ denotes the i th component of \hat{f}_{int} . The matrix $\underline{G}_{uu}^{(i)}$ should be derived for each displacement degree of freedom separately. As an example, it is derived for $i = 1$ by first calculating $\underline{T}_{uu}^{T(1)}$ from Equation (5.33):

$$\left(\underline{T}_{uu}^{(1)} \right)^T = [\underline{s}^T \quad \underline{0}^T \quad \underline{0}^T \quad \underline{0}^T]^T + u_{1,n} v. \quad (5.38)$$

Differentiating Equation (5.38) reads:

$$\left(\delta \underline{T}_{uu}^{(1)} \right)^T = [\underline{n}^T \quad \underline{0}^T \quad \underline{0}^T \quad \underline{0}^T]^T v^T \delta u + \delta u_{1,n} v + u_{1,n} \delta v = \underline{G}_{uu}^{(1)} \delta u. \quad (5.39)$$

Ignoring the variation of the column v because of its negligible effect (see [29, 95]) and calculating $\delta u_{1,n}$ from Equation (5.32), the matrix $\underline{G}_{uu}^{(1)}$ is derived as:

$$\underline{G}_{uu}^{(1)} = [\underline{n}^T \quad \underline{0}^T \quad \underline{0}^T \quad \underline{0}^T]^T v^T + v [\underline{n}^T \quad \underline{0}^T \quad \underline{0}^T \quad \underline{0}^T] - u_{1,s} v v^T. \quad (5.40)$$

Repeating this for the matrices $\underline{G}_{uu}^{(i)}$ for $i = 1, \dots, 8$, the stress stiffness matrix $\underline{K}_{uu}^\sigma$ is obtained using Equation (5.37).

In order to derive the stress stiffness matrices $\underline{K}_{hu}^\sigma$ and $\underline{K}_{hh}^\sigma$, the following relation is defined:

$$\begin{aligned} \delta \underline{T}_{hu}^T \hat{g}_{int} &= \sum_{i=1}^4 \left(\delta \underline{T}_{hu}^{(i)} \right)^T \hat{g}_{int}^{(i)} = \sum_{i=1}^4 \hat{g}_{int}^{(i)} \underline{G}_{hu}^{(i)} \delta u + \sum_{i=1}^4 \hat{g}_{int}^{(i)} \underline{G}_{hh}^{(i)} \delta h \\ &= \underline{K}_{hu}^\sigma \delta u + \underline{K}_{hh}^\sigma \delta h, \end{aligned} \quad (5.41)$$

where $\delta \underline{T}_{hu}^{(i)}$ denotes the i th row of $\delta \underline{T}_{hu}$ and $\hat{g}_{int}^{(i)}$ denotes the i th component of $\hat{\underline{g}}_{int}$. The matrices $\underline{G}_{hu}^{(i)}$ and $\underline{G}_{hh}^{(i)}$ are derived for each enrichment scaling factor degree of freedom separately. As an example, assuming $i = 1$, $\underline{T}_{hu}^{T(1)}$ is derived using Equations (5.35) and (5.36):

$$\left(\underline{T}_{hu}^{(1)}\right)^T = h_{b,n} \underline{v}. \quad (5.42)$$

Differentiating Equation (5.42) and calculating $\delta \hat{h}_{b,n}$ from Equation (5.35) results in:

$$\left(\delta \underline{T}_{hu}^{(1)}\right)^T = -h_{b,s} \underline{v} \underline{v}^T \delta \underline{u} + \underline{v} [n^T \ 0^T] \delta \underline{h} = \underline{G}_{hu}^{(1)} \delta \underline{u} + \underline{G}_{hh}^{(1)} \delta \underline{h}, \quad (5.43)$$

where $\delta \underline{v}$ has been ignored (see [29,95]). The above strategy can be used to determine $\underline{G}_{hu}^{(i)}$ and $\underline{G}_{hh}^{(i)}$ for $i = 1, \dots, 4$, which, after being substituted in Equation (5.41), gives the stress stiffness matrices $\underline{K}_{hu}^\sigma$ and $\underline{K}_{hh}^\sigma$.

General conclusion and outlook

6.1 Conclusion

Laminated structures are built by integration of dissimilar materials with various manufacturing technologies in order to obtain a high thermo-electro-mechanical performance at a low weight, size, and cost. However, considering the wide range of applications of such structures from micro-electronics to aerospace structural components, they are prone to complex thermo-hygro-mechanical loading conditions during their service life which may influence their structural integrity. Complex intra-laminar as well as inter-laminar damage mechanisms endanger the structural integrity of such systems which is directly in relation with their reliability and functionality. The presence of high stresses between dissimilar adherent layers in multi-layered structures causes accumulation of interfacial damage which can eventually result in interfacial delamination. It is a common failure mode leading to a loss of structural integrity. Therefore, together with dedicated experiments for interface characterization, predictive numerical tools are necessary to analyze the reliability or mechanical response of such structures during their design and optimization process to minimize such a catastrophic failure. The research presented in this thesis focused on the development of a robust and effective numerical framework for the simulation of interfacial delamination.

Due to the capability of cohesive zone models to predict both delamination initiation and growth as a result of degradation of adhesion between laminae and the simplicity of their application in a finite element framework, these models are widely used. However, these models suffer from an intrinsic mesh sensitivity. A sufficiently accurate kinematic description of the process zone of the cohesive crack is required; otherwise, numerical instabilities in the form of snap-backs occur in the global load-displacement response of the system. In a rather brittle interface where the size of the process zone is much smaller than the structural dimensions, the implications

are that either a very fine discretization must be used to eliminate the numerical instabilities or complex path-following techniques should be employed to trace the non-physical (discretization-induced) oscillatory path in very small increments.

Both aforementioned remedies result in a considerable increase in computational costs which limits the applicability of cohesive zone models to the simulation of brittle interfacial delamination, especially in a three-dimensional framework where an adaptive mesh refinement is not straightforward. The goal of this research was to develop a self-adaptive cohesive zone model to simulate interfacial delamination in an effective and robust manner by preserving a coarse discretization while avoiding path-following techniques.

The separation approximation within the interface elements located in the process zone was enriched by adding a piece-wise linear function with an adaptive peak position in a two-dimensional setting (or piece-wise planar functions in a three-dimensional setting) to the conventional interpolation functions. Adaptivity of the peak of the enrichment functions in individual interface elements mimics the physical delamination growth problem. The peak positions of the enrichment functions and the enrichment magnitudes form additional global degrees of freedom for which the values are determined by solving the global system. The bulk elements neighboring the enriched cohesive zone elements are enriched in a similar fashion to account for the continuity of displacements along the faces of the interfacial crack.

While adding only a simple extension to the set of conventional finite element interpolation functions in the process zone of the cohesive crack imposes a minor extra computational effort, the adaptivity of the enrichment makes it an effective substitute for the mesh refinement strategy where the added nodes are not adaptive. It results in a considerable reduction of the non-physical oscillations in the global response of the delaminating structure such that a standard Newton-Raphson iterative scheme could be applied without a need for complicated path-following techniques. The self-adaptive finite element framework developed in this thesis offers new possibilities for a general application of cohesive zone models to the simulation of interfacial delamination in an effective, robust, and accurate manner at a reasonable computational cost.

The activities and findings associated with the introduction and further extension and development of the self-adaptive finite elements are summarized as follows:

- The self-adaptive finite element framework was developed and applied to a simple one-dimensional example for which an analytical solution existed. The numerical results obtained from the enriched model showed a major improvement compared to the conventional cohesive zone model in terms of reducing the discretization-induced oscillations in the global response of the structure. The additional computational cost was minimized by using an adaptive enrichment strategy where only the elements located in the process zone were enriched.
- Adaptivity (mobility) of the enrichment function plays a key role in enabling

the self-adaptive finite elements to accurately capture the kinematics of the growing interface crack at all instances, which constitutes one of the major advantages of the proposed methodology. A consistent energy-based self-adaptive cohesive zone model, where the possible equilibrium states correspond to the local minima of the total potential of the system, was considered. The variation of the total potential with respect to the enrichment peak position was investigated and revealed a non-convex potential profile under some circumstances. The latter needed special treatment to improve the convergence. This investigation led to the development of a penalty formulation which ensures uniqueness of the solution as well as the stability of the solution procedure with a minimum constraint on the enrichment adaptivity.

- Based on the previous findings on numerical aspects of the enrichment, a two-dimensional mixed-mode self-adaptive cohesive zone model was formulated within a damage mechanics framework which accounted for the irreversibility of the delamination process.
- The self-adaptive cohesive zone model was extended to three-dimensional delamination problems by enriching all edges of the planar interface elements with hierarchical process-driven enrichment functions. The performance of the hierarchical 3D formulation was evaluated for crack growth problems where the crack front was parallel to the element edges or oblique with respect to the edges. Compared to conventional cohesive zone modelling, the self-adaptive framework had a considerable effect on reducing the oscillations to a level that the solution could be traced with a standard Newton-Raphson iterative scheme, even for the most brittle interface behaviour considered. In an attempt to improve the approximation in the process zone such that a constant crack front that grows in an oblique manner with respect to the element edges could be reproduced, a non-hierarchical formulation was proposed. Considering the requirement for the modification of standard finite element interpolation functions in the alternative approach and comparing its performance with the hierarchical enrichment, the superiority of the original hierarchical approach was demonstrated.
- The oscillations observed in the global load-displacement response of delaminating structures were quantified through Fourier analyses and the relationship between the amount of oscillations and the brittleness of the system was demonstrated for a given discretization. The effect of a persistent refinement on reducing the oscillations was quantified and was compared with different enrichment strategies.
- Choosing an irreversible mixed-mode traction-separation law which accounts for a coupling between delamination modes, the self-adaptive cohesive zone model was formulated within a large deformation framework. This enables the methodology to be applied to general engineering problems where material or geometrical non-linearities might occur. The numerical results were compared

with experimental results obtained from miniaturized mixed-mode bending tests which showed a satisfactory performance of the enhanced methodology.

6.2 Outlook

A more robust and effective cohesive zone model was obtained by formulating it within a self-adaptive finite element framework. The process-driven hierarchical enrichment was found to be a more effective and efficient substitute for a mesh refinement especially when the interface was rather brittle. In light of the research objective of this thesis and considering the scope and limitations of the proposed methodology, the following recommendations and suggestions are given for future research:

- In case of a very coarse discretization of the process zone, very high traction gradients might occur within a single interface element in the fracture process zone for which a bi-linear enrichment function is inadequate. Convergence problems arise due to a non-convex potential in such a case. However, the proposed methodology is well-suited to be extended to other enrichments as well, allowing for more complex separation profiles within a single cohesive zone element.
- Studying delamination problems, non-linearities may arise at both the interface and the bulk material. Higher order adaptive enrichment functions might show a better performance in such cases. Moreover, the bending behavior of the bulk material can be captured with a higher accuracy using higher order finite elements together with hierarchical enrichments.
- The oscillations observed in the global structural load-displacement response are discretization-induced ones which are not affected by the integration scheme. However, a numerical integration should capture the highly non-linear nature of the traction-separation law combined with the enriched kinematics with a reasonable accuracy. Integration of the self-adaptive finite elements can be done by either using fixed integration points (in which case a sufficiently high number is needed) or by a lower number of adaptive integration points. The former was chosen in this research for the convenience of the storage of history parameters in case of the enriched cohesive zone elements. In general, the bulk material can also be history-dependent which results in a considerable computational burden. Therefore, a more thorough study of the integration of self-adaptive finite elements is recommended to further improve the efficiency of self-adaptive finite elements.
- A penalty formulation was developed to ensure the uniqueness of the solution while imposing a minimum constraint on the enrichment adaptivity. Since the penalization affects the mobility of the enrichment peak position, a quantitative study of the penalty formulation is recommended. The penalty coefficient has

to be chosen such that it does not make major changes in the total potential of the system. The strategy to determine the value of the penalty coefficient could be further investigated.

- The self-adaptive finite elements improve the kinematic description within the fracture process zone. Application of this framework to modeling arbitrary cohesive crack growth in a continuum such as by X-FEM is conceptually possible. However, implementation aspects and its effectiveness have to be investigated.
- A proper damage evolution law that governs the loss of cohesive strength as a function of thermo-hygro-mechanical history could be developed by proper experiments in a wide range of mode mixities. Obtaining a realistic cohesive law, the self-adaptive cohesive zone model can then be used to evaluate the reliability of complex multi-layered structures for which the conventional cohesive zone models are not efficient.

Bibliography

- [1] ASTM D6671-01, standard test method for mixed mode i- mode ii interlaminar fracture toughness of unidirectional fiber reinforced polymer matrix composites. In *Annual book of ASTM standards*, volume 15.03. 2001.
- [2] G. Alfano. On the influence of the shape of the interface law on the application of cohesive-zone models. *Comp. Sci. Tech.*, 66:723–730, 2006.
- [3] G. Alfano and M.A. Crisfield. Finite element interface models for the delamination analysis of laminated composites: mechanical and computational issues. *Int. J. Numer. Meth. Engng.*, 50:1701–1736, 2001.
- [4] G. Alfano and M.A. Crisfield. Solution strategies for the delamination analysis based on a combination of local-control arc-length and line searches. *Int. J. Numer. Meth. Engng.*, 50:999–1048, 2003.
- [5] O. Allix and A. Corigliano. Geometrical and interfacial non-linearities in the analysis of delamination in composites. *Int. J. Solids Struct.*, 36:2189–2216, 1999.
- [6] O. Allix and P. Ladeveze. Interlaminar interface modelling for the prediction of delamination. *Compos. Struct.*, 22:235–242, 1992.
- [7] O. Allix, P. Ladeveze, and A. Corigliano. Damage analysis of interlaminar fracture specimens. *Compos. Struct.*, 31:61–74, 1995.
- [8] I. Babuska and J.M. Melenk. The partition of unity method. *Int. J. Numer. Meth. Engng.*, 40:727–758, 1997.
- [9] G. Bao and L. Wang. Multiple cracking in functionally graded ceramic/metal coatings. *Int. J. Solids Struct.*, 32:2853–2871, 1995.
- [10] G.I. Barenblatt. The formation of equilibrium cracks during brittle fracture. general ideas and hypotheses. axially-symmetric cracks. *J. Appl. Math. Mech.*, 23:622–636, 1959.
- [11] Z.P. Bazant and J. Planas. *Fracture and size effects in concrete and other quasi-brittle materials*. CRC Press, Boca Raton, 1998.

- [12] G. Beer. An isoparametric joint/interface element for finite element analysis. *Int. J. Numer. Meth. Engng.*, 21:585–600, 1985.
- [13] T. Belytschko and T. Black. Elastic crack growth in finite elements with minimal remeshing. *Int. J. Numer. Meth. Engng.*, 45:601–620, 1999.
- [14] T. Belytschko, J. Fish, and B.E. Engelmann. A finite element with embedded localization zones. *Comput. Methods Appl. Mech. Engrg.*, 70:59–89, 1988.
- [15] S.E. Benzley. Representation of singularities with isoparametric finite elements. *Int. J. Numer. Meth. Engng.*, 8:537–545, 1974.
- [16] B.R.K. Blackman, H. Hadavinia, A.J. Kinloch, and J.G. Williams. The use of a cohesive zone model to study the fracture of fibre composites and adhesively-bonded joints. *Int. J. Fract.*, 119:25–46, 2003.
- [17] P. Bocca, A. Carpinteri, and S. Valente. Mixed mode fracture of concrete. *Int. J. Solids Struct.*, 27:1139–1153, 1991.
- [18] R. Borg, L. Nilsson, and K. Simonsson. Modeling of delamination using a discretized cohesive zone and damage formulation. *Compos. Sci. Tech.*, 62:1299–1314, 2002.
- [19] P.O. Bouchard, F. Bay, and Y. Chastel. Numerical modelling of crack propagation: automatic remeshing and comparison of different criteria. *Comput. Methods Appl. Mech. Engrg.*, 192:3887–3908, 2003.
- [20] G.T. Camacho and M. Ortiz. Computational modeling of impact damage in brittle materials. *Int. J. Solids Struct.*, 33:2899–2938, 1996.
- [21] P.P. Camanho, C.G. Davila, and M.F. de Moura. Numerical simulation of mixed-mode progressive delamination in composite materials. *J. Comp. Mater.*, 37:1415–1438, 2003.
- [22] J.L. Chaboche, F. Feyel, and Y. Monerie. Interface debonding models: a viscous regularization with a limited rate dependency. *Int. J. Solids Struct.*, 38:3127–3160, 2001.
- [23] S.K. Chan, I.S. Tuba, and W.K. Wilson. On the finite element method in linear fracture mechanics. *Engng. Fracture Mech.*, 2:1–17, 1970.
- [24] N. Chandra, H. Li, C. Shet, and H. Ghonem. Some issues in the application of cohesive zone models for metal-ceramic interfaces. *Int. J. Solids Struct.*, 39:2827–2855, 2002.
- [25] A. Corigliano and O. Allix. Some aspects of interlaminar degradation in composites. *Comput. Methods Appl. Mech. Engrg.*, 185:203–224, 2000.
- [26] J.V. Cox. An extended finite element method with analytical enrichment for cohesive crack modeling. *Int. J. Numer. Meth. Engng.*, 78:48–83, 2009.

- [27] M.A. Crisfield. A fast incremental/iterative solution procedure that handles snap-through. *Comput. Struct.*, 13:55–62, 1981.
- [28] M.A. Crisfield and G. Alfano. Adaptive hierarchical enrichment for delamination fracture using a decohesive zone model. *Int. J. Numer. Meth. Engng.*, 54:1369–1390, 2002.
- [29] M.A. Crisfield and G.F. Moita. A co-rotational formulation for 2-d continua including incompatible modes. *Int. J. Numer. Meth. Engng.*, 39:2619–2633, 1996.
- [30] W.C. Cui and M.R. Wisnom. A combined stress-based and fracture-mechanics-based model for predicting delamination in composites. *Composites*, 24:467–474, 1993.
- [31] W.C. Cui, M.R. Wisnom, and M. Jones. A comparison of failure criteria to predict delamination of unidirectional glass/epoxy specimens waisted through the thickness. *Composites*, 23:158–166, 1992.
- [32] C. Daux, N. Moes, J. Dolbow, N. Sukumar, and T. Belytschko. *Int. J. Numer. Meth. Engng.*, 48:1741–1760, 2000.
- [33] R.A. Day and D.M. Potts. Zero thickness interface elements - numerical stability and application. *Int. J. Numer. Anal. Meth. Geomech.*, 18:689–708, 1994.
- [34] R. de Borst. Computation of post-bifurcation and post-failure behavior of strain-softening solids. *Comput. Struct.*, 25:211–224, 1987.
- [35] R. de Borst. Fracture in quasi-brittle materials: a review of continuum damage-based approaches. *Engng. Fracture Mech.*, 69:95–112, 2002.
- [36] R. de Borst. Numerical aspects of cohesive-zone models. *Engng. Fract. Mech.*, 70:1743–1757, 2003.
- [37] R. de Borst, M.A. Gutierrez, G.N. Wells, J.J.C. Remmers, and H. Askes. Cohesive-zone models, higher-order continuum theories and reliability methods for computational failure analysis. *Int. J. Numer. Meth. Engng.*, 60:289–315, 2004.
- [38] C.A. Duarte, I. Babuska, and J.T. Oden. Generalized finite element methods for three-dimensional structural mechanics problems. *Comput. Struct.*, 77:215–232, 2000.
- [39] C.A. Duarte, O.N. Hamzeh, T.J. Liszka, and W.W. Tworzydlo. A generalized finite element method for the simulation of three-dimensional dynamic crack propagation. *Comput. Methods Appl. Mech. Engrg.*, 190:2227–2262, 2001.
- [40] D.S. Dugdale. Yielding of steel sheets containing slits. *J. Mech. Phys. Solids*, 8:100–104, 1960.

- [41] E.N. Dvorkin, A.M. Cuitino, and G. Gioia. Finite elements with displacement interpolated embedded localization lines insensitive to mesh size and distortions. *Int. J. Numer. Meth. Engng.*, 30:541–564, 1990.
- [42] M. Elices, G.V. Guinea, J. Gomez, and J. Planas. The cohesive zone model: advantages, limitations and challenges. *Engng. Fract. Mech.*, 69:137–163, 2002.
- [43] V. Fiori and S. Orain. A multi scale finite element methodology to evaluate wire bond pad architectures. In L.J. Ernst, G.Q. Zhang, P. Rodgers, S. Marco, M. Meuwissen, and O. de SaintLeger, editors, *Proceedings of the 6th International Conference on Thermal, Mechanical and Multi-Physics Simulation and Experiments in Micro-Electronics and Micro-Systems. EuroSimE 2005*, pages 648–655, Berlin, Germany, 2005.
- [44] J.W. Foulk III. An examination of stability in cohesive zone modeling. *Comput. Methods Appl. Mech. Engng.*, 199:465–470, 2010.
- [45] M.G.D. Geers. Enhanced solution control for physically and geometrically non-linear problems. part i—the subplane control approach. *Int. J. Numer. Meth. Engng.*, 46:177–204, 1999.
- [46] M.G.D. Geers. Enhanced solution control for physically and geometrically non-linear problems. part ii—comparative performance analysis. *Int. J. Numer. Meth. Engng.*, 46:205–230, 1999.
- [47] W.H. Gerstle and J.E. Abdalla. Finite element meshing criteria for crack problems. *ASTM Special Technical Publication*, 1074:509–521, 1990.
- [48] L.N. Gifford and P.D. Hilton P.D. Stress intensity factors by enriched finite elements. *Engng. Fracture Mech.*, 10:485–496, 1978.
- [49] J.P.M. Goncalves, M.F.S.F. de Moura, P.M.S.T. de Castro, and A.T. Marques. Interface element including point-to-surface constraints for three-dimensional problems with damage propagation. *Engrg. Comput.*, 17:28–47, 2000.
- [50] V.K. Goyal, E.R. Johnson, and C.G. Davila. Irreversible constitutive law for modeling the delamination process using interfacial surface discontinuities. *Compos. Struct.*, 65:289–305, 2004.
- [51] A. Griffith. The phenomena of rupture and flow in solids. *Phil. Trans. R. Soc.*, A 221:163–198, 1921.
- [52] I. Guiamatsia, J.K. Ankersen, G.A.O. Davies, and L. Iannucci. Decohesion finite element with enriched basis functions for delamination. *Compos. Sci. Tech.*, 69:2616–2624, 2009.
- [53] M.A. Gutierrez. Energy release control for numerical simulations of failure in quasi-brittle solids. *Commun. Numer. Meth. Engng*, 20:19–29, 2008.

- [54] A. Hansbo and P. Hansbo. A finite element method for the simulation of strong and weak discontinuities in solid mechanics. *Comput. Methods Appl. Mech. Engrg.*, 193:3523–3540, 2004.
- [55] P.W. Harper and S.R. Hallett. Cohesive zone length in numerical simulations of composite delamination. *Engng. Fract. Mech.*, 75:4774–4792, 2008.
- [56] T.K. Hellen. On the method of virtual crack extensions. *Int. J. Numer. Meth. Engrg.*, 9:187–207, 1975.
- [57] H.B. Hellweg and M.A. Crisfield. A new arc-length method for handling sharp snap-backs. *Comput. Struct.*, 66:705–709, 1998.
- [58] A. Hillerborg, M. Modeer, and P.E. Petersson. Analysis of crack formation and crack growth in concrete by means of fracture mechanics and finite elements. *Cement Conc. Res.*, 6:773–782, 1976.
- [59] J.L. Hogberg. Mixed mode cohesive law. *Int. J. Fract.*, 141:549–559, 2006.
- [60] A.R. Ingraffea, W.H. Gerstle, P. Gergely, and V. Saouma. Fracture mechanics of bond in reinforced concrete. *ASCE J. Struct. Engrg.*, 110:871–890, 1984.
- [61] G.R. Irwin. Analysis of stresses and strains near the end of a crack traversing a plate. *Trans. ASME: J. Appl. Mech.*, 24:361–364, 1957.
- [62] N.E. Jansson and R. Larsson. A damage model for simulation of mixed-mode delamination growth. *Compos. Struct.*, 53:409–417, 2001.
- [63] Z.-H. Jin, G.H. Paulino, and R.H. Dodds Jr. Finite element investigation of quasi-static crack growth in functionally graded materials using a novel cohesive zone fracture model. *Trans. ASME: J. Appl. Mech.*, 69:370–379, 2002.
- [64] M. Jirasek. Comparative study on finite elements with embedded discontinuities. *Comput. Methods Appl. Mech. Engrg.*, 188:307–330, 2000.
- [65] M. Jirasek and T. Belytschko. Computational resolution of strong discontinuities. In H.A. Mang, F.G. Rammerstorfer, and J. Eberhardsteiner, editors, *Proceedings of the Fifth World Congress on Computational Mechanics*, Vienna, Austria, 2002.
- [66] M. Jirasek and T. Zimmerman. Embedded crack model: I. basic formulation. *Int. J. Numer. Meth. Engrg.*, 50:1269–1290, 2001.
- [67] M.F. Kanninen and C.H. Popelar. *Advanced fracture mechanics*. Oxford University Press, New York, 1985.
- [68] M. Klisinski, K. Runesson, and S. Sture. Finite element with inner softening band. *ASCE J. Engrg. Mech.*, 117:575–587, 1991.

- [69] M. Kolluri, J.P.M. Hoefnagels, J.A.W. van Dommelen, and M.G.D. Geers. Modeling and characterization of irreversible mixed mode interface delamination using a cohesive zone with combined damage and plasticity. *In preparation*.
- [70] M. Kolluri, J.P.M. Hoefnagels, J.A.W. van Dommelen, and M.G.D. Geers. An improved miniature mixed mode delamination setup for in-situ microscopic interface failure analyses. *J. Phys. D: Appl. Phys.*, 44:034005, 2011.
- [71] M. Kolluri, M.H.L. Thissen, J.P.M. Hoefnagels, J.A.W. van Dommelen, and M.G.D. Geers. In-situ characterization of interface delamination by a new miniature mixed mode bending setup. *Int. J. Fract.*, 158:183–195, 2009.
- [72] R. Krueger. The virtual crack closure technique: history, approach and applications. Technical Report CR-2002-211628, NASA, 2002.
- [73] S. Li, M.D. Thouless, A.M. Waas, J.A. Schroeder, and P.D. Zavattieri. Mixed-mode cohesive-zone models for fracture of an adhesively bonded polymer-matrix composite. *Engng. Fract. Mech.*, 73:64–78, 2006.
- [74] S. Li, J. Wang, and M.D. Thouless. The effects of shear on delamination in layered materials. *J. Mech. Phys. Solids*, 52:193–214, 2004.
- [75] H.R. Lotfi and P.B. Shing. Embedded representation of fracture in concrete with mixed finite elements. *Int. J. Numer. Meth. Engng.*, 38:1307–1325, 1995.
- [76] S. Mariani and U. Perego. Extended finite element method for quasi-brittle fracture. *Int. J. Numer. Meth. Engng.*, 58:103–126, 2003.
- [77] J.M. Melenk and I. Babuska. The partition of unity finite element method: Basic theory and applications. *Comput. Methods Appl. Mech. Engrg.*, 139:289–314, 1996.
- [78] J. Mergheim, E. Kuhl, and P. Steinmann. A finite element method for the computational modelling of cohesive cracks. *Int. J. Numer. Meth. Engng.*, 63:276–289, 2005.
- [79] J. Mergheim, E. Kuhl, and P. Steinmann. Towards the algorithmic treatment of 3d strong discontinuities. *Commun. Numer. Meth. Engng.*, 23:97–108, 2007.
- [80] G. Meschke and P. Dumstorff. Energy-based modeling of cohesive and cohesionless cracks via x-fem. *Comput. Methods Appl. Mech. Engrg.*, 196:2338–2357, 2007.
- [81] G. Meschke, P. Dumstorff, and W. Fleming. Variational extended finite element model for cohesive cracks: influence of integration and interface law. In A. Combescure, R. de Borst, and T. Belytschko, editors, *Proceedings of IUTAM Symposium on Discretization Methods for Evolving Discontinuities*, pages 283–301, Lyon, France, 2006.

- [82] Y. Mi, M.A. Crisfield, G.A.O. Davies, and H.B. Hellweg. Progressive delamination using interface elements. *J. Comp. Mater.*, 32:1246–1272, 1998.
- [83] N. Moes and T. Belytschko. Extended finite element method for cohesive crack growth. *Engng. Fract. Mech.*, 69:813–833, 2002.
- [84] N. Moes, J. Dolbow, and T. Belytschko. A finite element method for crack growth without remeshing. *Int. J. Numer. Meth. Engng.*, 46:131–150, 1999.
- [85] A. Needleman. A continuum model for void nucleation by inclusion debonding. *J. Appl. Mech.*, 54:525–531, 1987.
- [86] D. Ngo and A.C. Scordelis. Finite element analysis of reinforced concrete beams. *ACI J.*, 64:152–163, 1967.
- [87] J. Oliver. Modelling strong discontinuities in solid mechanics via strain softening constitutive equation. part 1: Fundamentals. *Int. J. Numer. Meth. Engng.*, 39:3575–3600, 1996.
- [88] J. Oliver. Modelling strong discontinuities in solid mechanics via strain softening constitutive equation. part 2: Numerical simulation. *Int. J. Numer. Meth. Engng.*, 39:3601–3623, 1996.
- [89] J. Oliver, A.E. Huespe, and P.J. Sanchez. A comparative study on finite elements for capturing strong discontinuities: E-fem vs x-fem. *Comput. Methods Appl. Mech. Engrg.*, 195:4732–4752, 2006.
- [90] M. Ortiz, Y. Leroy, and A. Needleman. A finite element method for localized failure analysis. *Comput. Methods Appl. Mech. Engrg.*, 61:189–214, 1987.
- [91] M. Ortiz and A. Pandolfi. Finite-deformation irreversible cohesive elements for three-dimensional crack-propagation analysis. *Int. J. Numer. Meth. Engng.*, 44:1267–1282, 1999.
- [92] Y.E. Pak. Linear electro-elastic fracture mechanics of piezoelectric materials. *Int. J. Fract.*, 54:79–100, 1992.
- [93] D.M. Parks. A stiffness derivative finite element technique for determination of crack tip stress intensity factors. *Int. J. Fract.*, 10:487–502, 1974.
- [94] N. Point and E. Sacco. A delamination model for laminated composites. *Int. J. Solids Struct.*, 33:483–509, 1996.
- [95] Y. Qiu, M.A. Crisfield, and G. Alfano. An interface element formulation for the simulation of delamination with buckling. *Engng. Fract. Mech.*, 68:1755–1776, 2001.
- [96] T. Rabczuk, G. Zi, A. Gerstenberger, and W.A. Wall. A new crack tip element for the phantom-node method with arbitrary cohesive cracks. *Int. J. Numer. Meth. Engng.*, 75:577–599, 2008.

- [97] I.S. Raju. Calculation of strain-energy release rates with higher order and singular finite elements. *Engng. Fracture Mech.*, 28:251–274, 1987.
- [98] E. Ramm. Strategies for tracing the nonlinear response near limit points. In W. Wunderlich, E. Stein, and K.J. Bathe, editors, *Nonlinear Finite Element Analyses in Structural Mechanics: Proceedings of the Europe-U.S. Workshop, Ruhr University Bochum, Germany, July 28-31, 1980*. Springer, Berlin, 1981.
- [99] J.R. Reeder and J.R. Crews Jr. Mixed-mode bending method for delamination testing. *AIAA J.*, 28:1270–1276, 1990.
- [100] J.J.C. Remmers, R. de Borst, and A. Needleman. A cohesive segments method for the simulation of crack growth. *Comput. Mech.*, 31:69–77, 2003.
- [101] J.R. Rice. A path independent integral and the approximate analysis of strain concentration by notches and cracks. *J. Appl. Mech.*, 35:379–386, 1968.
- [102] E. Riks. The application of newton’s method to the problem of elastic stability. *J. Appl. Mech.*, 39:1060–1066, 1972.
- [103] P. Robinson, T. Besant, and D. Hitchings. Delamination growth prediction using a finite element approach. In J.G. Williams and A. Pavan, editors, *Fracture of Polymers, Composites and Adhesives: 2nd ESIS TC4 Conference on Polymers and Composites, Les Diablerets, Switzerland, 1999.*, pages 135–147, Amsterdam, 2000. Elsevier Science B.V.
- [104] J.G. Rots. *Computational modeling of concrete fracture*. PhD thesis, Delft University of Technology, Delft, The Netherlands, 1988.
- [105] E.F. Rybicki and M.F. Kanninen. A finite element calculation of stress intensity factors by a modified crack closure integral. *Engng. Fracture Mech.*, 9:931–938, 1977.
- [106] M. Samimi, J.A.W. van Dommelen, and M.G.D. Geers. A self-adaptive finite element approach for simulation of mixed-mode delamination using cohesive zone models. *Engng. Fract. Mech.*, Accepted.
- [107] M. Samimi, J.A.W. van Dommelen, and M.G.D. Geers. Simulation of interlaminar damage in mixed-mode bending tests using large deformation self-adaptive cohesive zones. *In preparation*.
- [108] M. Samimi, J.A.W. van Dommelen, and M.G.D. Geers. A three-dimensional self-adaptive cohesive zone model for interfacial delamination. *To be submitted*.
- [109] M. Samimi, J.A.W. van Dommelen, and M.G.D. Geers. An enriched cohesive zone model for delamination in brittle interfaces. *Int. J. Numer. Meth. Engng.*, 80:609–630, 2009.

- [110] M. Samimi, B.A.E. van Hal, R.H.J. Peerlings, J.A.W. van Dommelen, and M.G.D. Geers. An enriched cohesive zone model for numerical simulation of interfacial delamination in microsystems. In L.J. Ernst, G.Q. Zhang, P. Rodgers, M. Meuwissen, S. Marco, W.D. van Driel, and O. de Saint Leger, editors, *Proceedings of the 8th International Conference on Thermal, Mechanical and Multi-Physics Simulation and Experiments in Micro-Electronics and Micro-Systems. EuroSimE 2007*, pages 1–7, London, United Kingdom, 2007.
- [111] J.C.J. Schellekens. *Computational strategies for composite structures*. PhD thesis, Delft University of Technology, Delft, The Netherlands, 1992.
- [112] J.C.J. Schellekens and R. de Borst. A non-linear finite element approach for the analysis of mode-i free edge delamination in composites. *Int. J. Solids Struct.*, 30:1239–1253, 1993.
- [113] J.C.J. Schellekens and R. de Borst. On the numerical integration of interface elements. *Int. J. Numer. Meth. Engng.*, 36:43–66, 1993.
- [114] C.F. Shih and R.J. Asaro. Elastic-plastic analysis of cracks on bimaterial interfaces: Part i- small scale yielding. *J. Appl. Mech.*, 55:299–316, 1988.
- [115] J.H. Song, P.M.A. Areias, and T. Belytschko. A method for dynamic crack and shear band propagation with phantom nodes. *Int. J. Numer. Meth. Engng.*, 67:868–893, 2006.
- [116] N. Sukumar, Z.Y. Huang, J.H. Prevost, and Z. Suo. Partition of unity enrichment for bimaterial interface cracks. *Int. J. Numer. Meth. Engng.*, 59:1075–1102, 2004.
- [117] N. Sukumar, N. Moes, B. Moran, and T. Belytschko. Extended finite element method for three-dimensional crack modelling. *Int. J. Numer. Meth. Engng.*, 48:1549–1570, 2000.
- [118] N. Sukumar, B. Moran, T. Black, and T. Belytschko. An element-free galerkin method for three-dimensional fracture mechanics. *Comp. Mech.*, 20:170–175, 1997.
- [119] R.T. Tenchev and B.G. Falzon. A pseudo-transient solution strategy for the analysis of delamination by means of interface elements. *Finite Elem. Anal. Des.*, 42:698–708, 2006.
- [120] M.D. Thouless. Fracture of a model interface under mixed-mode loading. *Acta Metall. Mater.*, 38:1135–1140, 1990.
- [121] M.D. Thouless, J.W. Hutchinson, and E.G. Liniger. Plane-strain, buckling-driven delamination of thin films: model experiments and mode-ii fracture. *Acta Metall. Mater.*, 40:2639–2649, 1992.

- [122] T. Tomar, J. Zhai, and M. Zhou. Bounds for element size in a variable stiffness cohesive finite element. *Int. J. Numer. Meth. Engng.*, 61:1894–1920, 2004.
- [123] A. Turon, P.P. Camanho, J. Costa, and C.G. Davila. A damage model for the simulation of delamination in advanced composites under variable-mode loading. *Mech. Mater.*, 38:1072–1089, 2006.
- [124] A. Turon, C.G. Davila, P.P. Camanho, and J. Costa. An engineering solution for mesh size effects in the simulation of delamination using cohesive zone models. *Engng. Fract. Mech.*, 74:1665–1682, 2007.
- [125] V. Tvergaard. Effect of fiber debonding in a whisker-reinforced metal. *Mater. Sci. Engng.*, A 125:203–213, 1990.
- [126] V. Tvergaard. Crack growth predictions by cohesive zone model for ductile fracture. *J. Mech. Phys. Solids*, 49:2191–2207, 2001.
- [127] M.J. van den Bosch, P.J.G. Schreurs, and M.G.D Geers. An improved description of the exponential xu and needleman cohesive zone law for mixed-mode decohesion. *Engng. Fract. Mech.*, 73:1220–1234, 2006.
- [128] M.J. van den Bosch, P.J.G. Schreurs, and M.G.D Geers. A cohesive zone model with a large displacement formulation accounting for interfacial fibrillation. *Eur. J. Mech. A/Solids*, 26:1–19, 2007.
- [129] M.J. van den Bosch, P.J.G. Schreurs, and M.G.D Geers. On the development of a 3d cohesive zone element in the presence of large deformations. *Comput. Mech.*, 42:171–180, 2008.
- [130] B.A.E. van Hal, R.H.J. Peerlings, M.G.D. Geers, and O. van der Sluis. Cohesive zone modeling for structural integrity analysis of ic interconnects. *Micro. Rel.*, 47:1251–1261, 2007.
- [131] J. Wang. Cohesive zone model of frp-concrete interface debonding under mixed-mode loading. *Int. J. Solids Struct.*, 44:6551–6568, 2007.
- [132] P.A. Wawrzynek and A.R. Ingraffea. An interactive approach to local remeshing around a propagating crack. *Finite Elem. Anal. Des.*, 5:87–96, 1989.
- [133] Y.J. Wei and L. Anand. Grain-boundary sliding and separation in polycrystalline metals: application to nanocrystalline fcc metals. *J. Mech. Phys. Solids*, 52:2587–2616, 2004.
- [134] G.N. Wells and L.J. Sluys. A new method for modelling cohesive cracks using finite elements. *Int. J. Numer. Meth. Engng.*, 50:2667–2682, 2001.
- [135] M.R. Wisnom. Modelling discrete failures in composites with interface elements. *Composites: Part A*, 41:795–805, 2010.

-
- [136] Q.Z. Xiao and B.L. Karihaloo. Asymptotic fields at frictionless and frictional cohesive crack tips in quasi-brittle materials. *J. Mech. Mater. Struct.*, 1:881–910, 2006.
- [137] D. Xie and A.M. Waas. Discrete cohesive zone model for mixed-mode fracture using finite element analysis. *Engng. Fract. Mech.*, 73:1783–1796, 2006.
- [138] X.-P. Xu and A. Needleman. Void nucleation by inclusion debonding in a crystal matrix. *Model. Simul. Mater. Sci. Eng.*, 1:111–132, 1993.
- [139] X.-P. Xu and A. Needleman. Numerical simulations of fast crack growth in brittle solids. *J. Mech. Phys. Solids*, 42:1397–1434, 1994.
- [140] Q. Yang and B. Cox. Cohesive models for damage evolution in laminated composites. *Int. J. Fract.*, 133:107–137, 2005.
- [141] P.D. Zavattieri and H.D. Espinosa. Grain level analysis of crack initiation and propagation in brittle materials. *Acta mater.*, 49:4291–4311, 2001.
- [142] Z. Zhang and G.H. Paulino. Cohesive zone modeling of dynamic failure in homogeneous and functionally graded materials. *Int. J. Plast.*, 21:1195–1254, 2005.
- [143] O.C. Zienkiewicz and R.L. Taylor. *The Finite Element Method. Vol I: The Basis*. Butterworth-Heinemann, Oxford, 2000.

Samenvatting

Falen van interfaces in de vorm van delaminatie resulteert vaak in het slecht functioneren of bezwijken van gelamineerde structuren. Verschillende numerieke technieken zijn voorgesteld voor het simuleren van dit proces. Vanwege de mogelijkheid om zowel de initiatie als groei van delaminatie te voorspellen worden vaak cohesive zone modellen gebruikt om delaminatie te simuleren waarbij de adhesie tussen twee materialen geleidelijk degradeert wanneer de interface ertussen geopend wordt.

Toepassing van cohesive zone modellen voor het modelleren van delaminatie in brosse interfaces in een quasistatische eindige elementen formulering is onderhevig aan een intrinsieke gevoeligheid voor de discretisatie. Een groot aantal interface elementen is nodig voor de discretisatie van de proces zone van een scheur. Wanneer dit niet het geval is, zal het plotseling vrijkomen van energie in grote cohesive zone elementen resulteren in een serie van snap-through en snap-back punten in de globale kracht-verplaatsing respons van het systeem, waardoor de numerieke efficiëntie nadelig beïnvloed wordt.

Hoewel rekentechnisch dure technieken gebruikt kunnen worden om het oscillerende belastingspad te volgen, kan de efficiëntie en robuustheid van brosse cohesive zone modellen aanzienlijk verbeterd worden door het reduceren van de oscillaties in de kracht-verplaatsing response zonder een verdere mesh verfijning. Met dit doel voor ogen wordt de benadering van de scheuropening in de proces zone verrijkt met een adaptieve hiërarchische uitbreiding. De lineaire benadering van de opening van het cohesive zone element is verrijkt met een bi-lineaire functie, waarbij de positie van de piek van de verrijking en de grootte van de verrijking beschouwd worden als extra vrijheidsgraden die bepaald worden door het minimaliseren van de totale potentiaal van het globale systeem. Door de mobiliteit van de piek van de verrijkingfunctie binnen het cohesive zone element wordt de discretisatie aangepast aan de fysica van het probleem.

Belangrijke numerieke aspecten van de voorgestelde verrijkingstrategie, zoals de mobiliteit and uniekheid van de oplossing zijn uitgebreid onderzocht. De efficiëntie en robuustheid van de verrijking zijn getoond aan de hand van numerieke voorbeelden die de algemene toepasbaarheid van de methode laten zien. Door toepassing van de verrijking hoeft de mesh niet verder verfijnd te worden terwijl de standaard

Newton–Raphson methode toepasbaar blijft in het geval van een relatief grove mesh, waardoor grote rekenkosten bespaard blijven. Het voorgestelde verrijkingsschema is uitgebreid naar delaminatie in een driedimensionale eindige elementen formulering. Vlakke interface elementen zijn langs alle zijden verrijkt met bi-lineaire functies met mobiele pieken. Het effect van de voorgestelde methode op de reductie van oscillaties gerelateerd aan de discretisatie is kwantitatief geëvalueerd. Voor situaties van scheurgroei waarbij het front van de scheur niet uitgelijnd is met de randen van het element is een niet-hiërarchische verrijkingstrategie ontwikkeld en de prestaties ervan zijn vergeleken met de hiërarchische methode.

De zelfadaptieve eindige elementen formulering is uitgebreid naar een formulering die geschikt is voor grote deformaties en is toegepast op interfaces in micro-elektronica onder realistische mixed-mode belastingcondities. In het bijzonder zijn materiaal/interface systemen gemodelleerd in geminiaturiseerde mixed-mode buig-experimenten, waarbij de mode hoek varieert over een groot bereik en de resultaten zijn vergeleken met experimentele resultaten. In de constitutieve relatie die gebruikt is voor de interface is de scheurtaaiheid afhankelijk van de mode hoek. Hiermee kan het verrijkte cohesive zone model gebruikt worden voor de nauwkeurige, effectieve en efficiënte simulatie van het gedrag van brosse interfaces.

Acknowledgements

The work presented in this thesis was hardly possible without direct and indirect contribution of many people. First of all, I would like to thank my promoter Marc Geers for his professional support and guidance with which I could keep on being on the right track with an optimistic hard working attitude. I found numerous discussions with my co-promoter Hans van Dommelen quite constructive and essential to this work. Accuracy, critical thinking, and respecting all small details while having the big picture in mind are among the values I got well aware of in light of his supervision within the past several years.

In addition to my promoters, I would like to thank other staff members of the Materials Technology Institute (MaTe) and especially the mechanics of materials group for their support and feedback. I would like to thank Marcel Brekelmans, Johan Hoefnagels, Varvara Kouznetsova, Ron Peerlings, and Piet Schreurs for their comments on my work during project and group meetings or through discussions. I would like to thank Alice van Litsenburg for her help in many occasions. The computer and software problems could be a real bottleneck without the help of Leo Wouters and Patrick van Brakel. I would like to thank both for their help in that regard. I am grateful of Marleen and Yvon for all their friendly efforts in MaTe with which I could feel at home. I would like to thank staff members in personnel and education offices for their efforts during these years in arranging administrative issues. I would also like to thank Ruud Voncken and Olaf van der Sluis from Philips for their feedback and support.

I am grateful to the committee members, Dr. Giulio Alfano, Prof. Harald van Brummelen, Prof. Nicolas Moes, Prof. Bert Sluys, and Prof. Viggo Tvergaard, for their effort in reading my thesis, giving comments to improve the quality of the work, and attending my defense.

I would like to thank my friends in MaTe, Tuncay, Cem, Britta, Izzet, Frederico, Gabriel, Viny, Rudy, Muge, Ana, Francesco, Pina, Erica, and Graham; thanks for your company. I owe all of you for the very pleasant memories of my stay in Eindhoven. I am thankful of my colleagues and friends in the Netherlands, Alexei, Ali, Amin &

Parisa, Anish, Bas, Bhairav, Can, Carole, Hamed & Negar, Hamid, Hristina, Iman, Isa, Jan, Javad, John, Juan Carlos, Kambiz & Sima, Kamyar & Pegah, Lambert, Lars, Leong Hien, Lucia, Lynda, Marc, Marina, Matej, Michael, Michiel, Murthy, Parsa, Paul, Peter, Pieter, Pouya & Solmaz, Reza, Salman, Samaneh & Saeed, Sebastian, Tom and all others. Special thanks to my former officemates, Arjen, Bart, Birgit, Chantal, Chen-Ket, Famke, Jasper, Kristel, Marloes, and Moniek for providing me with a nice work atmosphere.

I would also like to thank my friends and family in Iran for their kind support under any circumstances. Being far away or spending my holidays back in Iran with them, I could always feel the energy I was receiving through their love and friendship.

Finally, my dear Samaneh, I don't know how to thank you for your presence at difficult times, your love and caring. With your energy, full support, and encouragement, nothing seems unreachable.

Mohammad Samimi
Delft, April 2011.

Curriculum Vitae

Mohammad Samimi was born on 19 January 1980 in Isfahan (Esfahan), Iran. After finishing his high school education, with specialization in maths/physics in 1998 at the National Organization for Development of Exceptional Talents in Isfahan, he entered Isfahan University of Technology where he got his B.Sc. degree in civil engineering in 2002. He continued his education in Sharif University of Technology, Tehran, Iran, where he got his M.Sc. degree in structural engineering in 2004. His M.Sc. research, titled "Application of RKPM in numerical simulation of pressure-sensitive materials using a cap plasticity model", was carried out under supervision of Prof. A.R. Khoei at the Department of Civil Engineering, Sharif University of Technology, Tehran, Iran. He worked as a structural engineer in a consultant engineering company and as a lecturer in several private universities in Tehran and Isfahan in the period 2004-2006. In July 2006, he moved to the Netherlands to pursue his education and research through a MicroNed Ph.D. program in the group of Prof. Marc Geers in the Department of Mechanical Engineering, Eindhoven University of Technology. The focus of his Ph.D. research was on developing a robust and efficient self-adaptive cohesive zone model for interfacial delamination. The results of his Ph.D. research are presented in this dissertation. He is currently a post-doctoral researcher at the Department of Precision and Microsystems Engineering, Faculty of Mechanical, Maritime and Materials Engineering at Delft University of Technology.